UNIVERSITEIT VAN PRETORIA
UNIVERSITY OF PRETORIA
YUNIBESITHI YA PRETORIA

OPTIMIZING LDPC CODES FOR A MOBILE WIMAX SYSTEM WITH A SATURATED TRANSMISSION AMPLIFIER

By

Brian P Salmon

Studyleader: Professor J.C. Olivier (University of Pretoria, South Africa)

Co-Studyleader: Dr B.T.J. Maharaj (University of Pretoria, South Africa)

Submitted in partial fulfillment of the requirements for the degree

Master of Engineering (Electronic)

in the

Department of Electrical, Electronic and Computer Engineering

in the

School of Engineering

in the

Faculty of Engineering, Built Environment and Information Technology

UNIVERSITY OF PRETORIA

July 2008

UNIVERSITEIT VAN PRETORIA
UNIVERSITY OF PRETORIA
YUNIBESITHI YA PRETORIA

SUMMARY

OPTIMIZING LDPC CODES FOR A MOBILE WIMAX SYSTEM WITH A SATURATED TRANSMISSION AMPLIFIER

by

Brian P Salmon

Studyleader: Professor J.C. Olivier (University of Pretoria, South Africa)

Co-Studyleader: Dr B.T.J. Maharaj (University of Pretoria, South Africa)

Department of Electrical, Electronic and Computer Engineering

Master of Engineering (Electronic)

In mobile communication, the user's information is transmitted through a wireless communication link that is subjected to a range of deteriorating effects. The quality of the transmission can be presented by the rate of transfer and the reliability of the received stream. The capacity of the communication link can be reached through the use of channel coding. Channel coding is the method of adding redundant information to the user's information to mitigate the deteriorating effects of the communication link. Mobile WiMAX is a technology that makes use of orthogonal frequency division multiplexing (OFDM) modulation to transmit information over a wireless communication channel. The OFDM physical layer has a high peak average to power ratio (PAPR) characteristic that saturates the transmitter's amplifier quite easily when proper backoff is not made in the transmission power. In this dissertation an optimized graph code was used as an alternative solution to improve the system's performance in the presence of a saturated transmission's amplifier. The graph code was derived from a degree distribution given by the density evolution algorithm and provided no extra network overhead to implement. The performance analysis resulted in a factor of 10 improvement in the error floor and a coding gain of 1.5 dB. This was all accomplished with impairments provided by the mobile WiMAX standard in the construction of the graph code.

Keywords:

Low-density parity-check codes, Density Evolution, Peak-average power-ratio, WiMAX.

UNIVERSITEIT VAN PRETORIA
UNIVERSITY OF PRETORIA
YUNIBESITHI YA PRETORIA

OPSOMMING

VERBETERING VAN 'N LDPC KODE VIR 'N MOBIELE WIMAX STELSEL MET 'N VERSADIGDE TRANSMISSIE VERSTERKER

deur

Brian P Salmon

Studieleier: Professor J.C. Olivier (Universiteit van Pretoria, Suid Afrika)

Mede-Studieleier: Dr B.T.J. Maharaj (Universiteit van Pretoria, Suid Afrika)

Departement Elektriese-,Elektroniese- en Rekenaar Ingenieurswese

Meester in Ingenieurswese (Elektronies)

Mobiele kommunikasie behels die stuur van gebruiker informasie deur 'n draadlose kommunikasie medium wat 'n reeks verswakking effekte het wanneer dit ontvang word. Die kwaliteit van die kommunikasie kan vergelyk word teen die data tempo en die betroubaarheid van die informasie. Deur vorige studies is daar gevind dat kanaal kapasiteit kan bereik word deur gebruik te maak van kanaal kodering. Kanaal kodering is 'n metode wat addisionele informasie byvoeg om die gebruiker se informasie te beskerm teen die effekte van die kommunikasie medium. Mobiele WiMAX is 'n tegnologie wat gebruik maak van ortogonale frekwensie divisie multipleksering (OFDM) modulasie om informasie deur 'n draadlose kommunikasie medium te stuur. OFDM het 'n hoë piek-tot-gemiddelde drywing verhouding (PGDV) eienskap wat die afsender versterker met gemak versadig wanneer gepaste krag vermindering metodes nie in die afsender gebruik word nie. In hieride dissertasie was 'n grafiese kode ontwerp wat as 'n alternatiewe oplossing is tot die versadiging van die transmissie versterker. Die grafiese kode is afgelei van 'n grade distribusie wat afgelei was deur die digtheid evolusie algoritme en die voordeel van hierdie grafiese kode is dat geen ekstra netwerk behandeling nodig is om dit te implementeer nie. 'n Faktor van 10 in verbetering was gesien in die fout vloer van die stelsel effektiteit analise en 'n kodering wins van 1.5 dB was ook verkry. Al die bogenoemde is bereik deur die grafiese kode ontwerp selfs met die beperkte stelsel parameters in die mobiele WiMAX standaard.

Sleutelwoorde:

Lae digtheid pariteit kodes, Digtheid evolusie, Piek-tot-gemiddelde drywing verhouding, WiMAX.

This dissertation is dedicated to:

God Almighty, for blessing me with all my talents and providing me with all the opportunities in my life.

My loving mother, for never losing faith and always standing by my side.

UNIVERSITEIT VAN PRETORIA
UNIVERSITY OF PRETORIA
YUNIBESITHI YA PRETORIA

ACKNOWLEDGEMENT

The author would like to thank the following people and institutions without whose help this dissertation would not have been possible.

- My study leader Prof J.C Olivier, for all the advice and guidance he has given me throughout the course of my studies.
- Dr. B.T.J. Maharaj and my fellow students at the Sentech Chair in Broadband Wireless Multimedia Communications (BWMC) at the University of Pretoria.
- The Center for Teletraffic Engineering in an Information Society (CeTEIS) for their financial support.
- My fellow student Waldo Kleynhans for his useful suggestions and good advice.
- The Advance Computing Cluster maintained by Hans Grobler at the University of Pretoria.

CONTENTS

LIST OF FIGURES

LIST OF TABLES

ABBREVIATIONS

AAS	Adaptive Antenna System
ACI	Adjacent Channel Interference
AWGN	Additive White Gaussian Noise
BER	Bit Error Rate
BEC	Binary Erasure Channel
BP	Belief Propagation
BS	Base Station
BSC	Binary Symmetrical Channel
CC	Convolutional Code
CID	Cell Identification
CIR	Channel Impulse Response
CG	Coding Gain
CP	Cyclic Prefix
CSI	Channel State Information
CW	Continuous Wave
DC	Direct Current
DE	Density Evolution

DSL	Digital Subscriber Loop
ECC	Error Correction Code
EXIT	Extrinsic Information Transfer
FEC	Forward Error Correction
FFT	Fast Fourier Transform
FIR	Finite Impulse Response
FUSC	Full Usage of Subchannels
HDD	Hard Decision Decoding
HPA	High Power Amplifier
IEEE	Institute of Electrical and Electronics Engineers
IFFT	Infinite Fast Fourier Transform
ISI	Intersymbol Interference
LDPC	Low Density Parity Check
LLR	Log-Likelihood Ratio
LOS	Line of Sight
LSB	Least Significant Bit
MAP	Maximum Aposteriori Probability
MIMO	Multiple Input Multiple Output
ML	Maximum Likelihood
NASA	National Aeronautics and Space Administration
NLOS	No line of sight
OFDM	Orthogonal Frequency Division Multiplexing
OFDMA	Orthogonal Frequency Division Multiple Access
PAM	Pulse Amplitude Modulation
PAPR	Peak-to-Average Power Ratio

PCL	Peak Clipping Level
PDF	Probability Density Function
PDP	Power Delay Profile
PEG	Progressive Edge Growth
PHY	Physical
PRBS	Pseudorandom Binary Source
PSAM	Pilot Symbol Assistant Modulation
PSD	Power Spectral Density
PSK	Phase Shift Keying
PUSC	Partial Usage of Subchannels
QAM	Quadrature Amplitude Modulation
QPSK	Quadrature Phase Shift Keying
RF	Radio Frequency
RMS	Root Mean Square
SC	Subcarrier
SDD	Soft Decision Decoding
SHF	Super High Frequency
SNR	Signal to Noise Ratio
SS	Subscriber station
TCM	Trellis Code Modulation
TDD	Time Division Duplex
UHF	Ultra High Frequency
VA	Viterbi Algorithm
WiMAX	Worldwide Interoperability for Microwave Access
WirelessMAN	Wireless Metropolitan Area Network

CHAPTER ONE
INTRODUCTION

1.1 BRIEF HISTORY OF CODING THEORY

Even though the need for reliable communication is as old as our civilization itself, it is only in recent times that communication has utilized radio frequency (RF) signals. In 1897, Guglielmo Marconi demonstrated that continuous communication could be provided using RF signals [1]. The possibility to correct errors in RF communication was shown to be possible by Shannon in 1948 [2]. Shannon showed that given a desired rate of communication measured in $bits/s/Hz$, a minimum threshold in the required signal to noise ratio (SNR) is required if all the errors are to be corrected.

The theory of error correction coding (ECC) evolved soon after Shannon's work by the introduction of Hamming codes [3], followed by the development of Golay codes [4]. Both codes were considered to be perfect codes [5], but more importantly this work led to new research on finding optimal error correction codes.

The class of convolutional codes [6] was developed in 1955 and outperforms both perfect codes in an additive white Gaussian noise (AWGN) channel [5] in terms of the achievable bit error rate (BER). The efficient decoding of the convolutional codes was shown to be possible by Viterbi [7] in 1967. The Viterbi algorithm found many practical applications over the next 40 years as convolutional codes were standardized as a mandatory coding scheme in most wireless technologies [8–10].

In 1960, a linear block code known as Reed Solomon codes [11–14] was developed and found many practical applications ranging from compact disc players to deep-space applications [15].

Reed Solomon codes are most suitable when the correction of burst errors in a communication medium is desired and are decodable using the Berlekamp-Massey algorithm [5].

In 1963, Gallager invented the sparse linear block code [16], and these have become known as Low-Density Parity-Check (LDPC) codes. The encoding and decoding of these codes was considered unfeasible, and hence was soon forgotten [17–19].

Over the following decade other error correcting codes were developed but it was not until 1982 that the Trellis Coded Modulation (TCM) error correction codes [20] proved to yield more performance gain by joining a coding and a modulation scheme with each other.

The next key point in the field of coding theory was the discovery of the Turbo codes [21] in 1993. Turbo Codes were able to approach the Shannon limit within a fraction of a decibel (dB) in an AWGN channel. Turbo codes was standardized in mobile WiMAX [8] as an optional coding scheme.

LDPC codes were rediscovered [19] in 1999 and this started renewed research at finding sparse graph codes that could approach capacity. Belief propagation [22–24] was shown in 1963 as an algorithm for decoding LDPC codes [16]. It is possible to decode large LDPC codes using Belief propagation, which led to relatively simple decoding strategies. This was a key contributing factor in the success of LDPC codes. It was demonstrated that LDPC codes were also able to reach the Shannon limit [25, 26] just as Turbo codes could but with a lower complexity.

A method for optimizing a LDPC code, known as *density evolution* (DE), was first presented in [16] for a binary erasure channel (BEC). This method later evolved to use continuous functions with special emphasis on a binary symmetrical channel (BSC) [27]. Further optimization of LDPC codes was achieved through the analysis of irregular code design to reach the Shannon capacity for both a frequency non-selective fading channel and the AWGN channel [28, 29].

1.2 BRIEF OVERVIEW OF WIMAX

Mobile WiMAX (Worldwide Interoperability for Microwave Access) which is also known as the IEEE802.16e-2005 standard, operates with the following physical (PHY) air interfaces: single carrier modulation, orthogonal frequency division multiplexing (OFDM) and orthogonal frequency division multiple access (OFDMA) respectively. Mobile WiMAX was created by

the WiMAX forum[1] in December 2005 and is an amendment to the fixed WiMAX standard (IEEE802.16d-2004). The aim is to deliver *last mile* broadband wireless access as an alternative to digital subscriber loop (DSL) solutions.

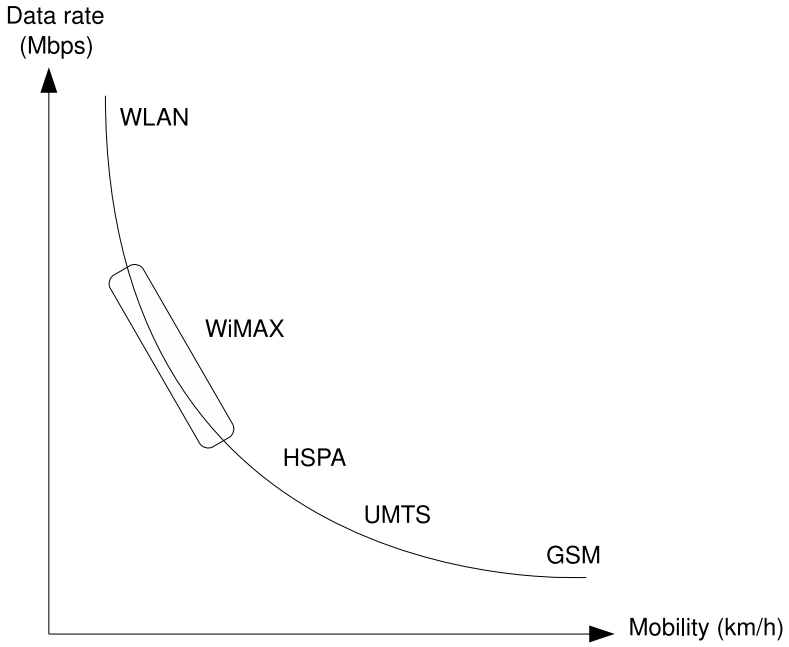

FIGURE 1.1: Competing technologies

The mobile WiMAX standard defines the operational region be in the ultra high frequency (UHF) and super high frequency (SHF) band which is below the 10 GHz band. The radio wavelength in this band is long enough to support a non line of sight (NLOS) communication link [8, 9]. The main factors limiting the performance in this band are the thermal noise generated at the receiver and the multipath propagation of signals [30].

The mobile WiMAX is scalable within a range of available channel bandwidths ranging between 1.25-20 MHz and provides downlink and uplink speeds of 10-70 Mbps. Capacity may be improved by using an intelligent Adaptive Antenna System (AAS) and Multiple Input Multiple Output (MIMO) technology [31].

1.3 OBJECTIVE OF THIS DISSERTATION

LDPC codes have matured [18] since its rediscovery and were included as an optional coding scheme in the mobile WiMAX standard [8]. For this reason, the first objective in this

[1] WiMAX Forum was formed in June 2001 to promote conformance and interoperability of the WiMAX standard (IEEE802.16-2001).

dissertation was to study the performance achievable when using the LDPC code defined in the mobile WiMAX standard. In order to verify results presented in this dissertation, a realistic WiMAX simulation platform needed to be designed and developed. Hence, a realistic mobile WiMAX simulator was developed that conforms to the mobile WiMAX standard [8]. The scalable OFDMA PHY air interface was implemented with the full-usage of subchannels (FUSC) as mode of operation. Implementation was based on its inherent frequency diversity over subchannels and its low network overhead.

The second objective in this dissertation was to compare the LDPC codes to the National Aeronautics and Space Administration's (NASA) convolutional code[2] in order to establish a common performance platform.

The last objective was to analyze and develop a novel sparse graph code to reduce the effect of the high peak-to-average power ratio (PAPR) which is a characteristic of OFDM modulation. This method has the distinct advantage of limiting the backoff at the power amplifier and therefore reduces the loss of sensitivity in practical WiMAX systems.

1.4 OUTLINE OF THE DISSERTATION

The outline of this dissertation is as follows. The dissertation starts by describing a realistic mobile WiMAX simulation platform in Chapter 2 with all its characteristics of interest. Chapter 3 explains how an error correction coding scheme operates within a mobile WiMAX communication system and is followed by the design parameters and implementation of the standardized convolutional code in the mobile WiMAX platform. The standardized convolutional code will serve as a benchmark to compare performance of all sparse graph codes as used in this dissertation.

The notation and design parameters used in the analysis and design of a LDPC code is given in chapter 4. LDPC codes are optimized by using the analysis for peak clipping conditions at the transmitter. In the same chapter the manner in which LDPC codes were constructed in order to combat the effect of peak clipping, is addressed.

Chapter 5 begins with illustrating the range of channel conditions that will be used for testing different coding schemes. Both the convolutional code and standardized LDPC code are tested on the mobile WiMAX platform for a range of channel conditions. This is followed by

[2] The NASA convolutional code is a mandatory coding scheme in mobile WiMAX

the illustration of performance improvement of the optimized LDPC codes in peak clipping conditions. The dissertation is concluded in chapter 6 with concluding remarks and future research.

1.5 CONTRIBUTIONS FROM THIS AND RELATED STUDIES

The following journal paper based on the mobile WiMAX simulation platform was submitted to the Institute of Electrical and Electronics Engineers (IEEE) Transactions on Education:

1. B.P. Salmon, W. Kleynhans, J.C. Olivier and B.T. Maharaj, *"Teaching the theory of channel estimation and coding via a mobile WiMAX simulation platform"*, submitted for publication

The following conference paper was submitted to the PIMRC Conference 2008 and the work is based on the results directly obtained from this dissertation:

1. B.P. Salmon, W. Kleynhans, J.C. Olivier and B.T. Maharaj, *"Performance analysis of channel coding techniques in a mobile WiMAX system with reduced transmission power"*, submitted for publication

The author co-authored the following conference papers that were submitted to the PIMRC 2008 conference and is based on a related dissertation on the analysis of channel estimation and equalization methods:

1. W. Kleynhans, B.P. Salmon, J.C. Olivier and B.T. Maharaj, *"On adaptive frequency domain interpolation for mobile WiMAX"*, submitted for publication

2. W. Kleynhans, B.P. Salmon, J.C. Olivier and B.T. Maharaj, *"An evaluation of channel estimation methods on a mobile WiMAX platform"*, submitted for publication

The following IEEE WCNC 2007 conference paper has been accepted with the work being directly based on the results from this dissertation:

1. B.P. Salmon and J.C. Olivier, *"Performance analysis of low-density parity-check codes on a WiMAX platform"*, in Proc. IEEE WCNC'2007, vol. 1, Hong Kong, March 2007, pp. 569-571.

CHAPTER TWO
MOBILE WiMAX

2.1 CHAPTER OVERVIEW

The chapter begins with discussing the mobile fading channel of interest that was used within the mobile WiMAX simulator. The mobile fading channel with all desired characteristics was emulated with a complex base band communication model. The mobile fading channel characteristics of interest were discussed in this chapter and are AWGN, multipath propagation and flat fading respectively. Several different multipath propagation profiles are appended in appendix A that were obtained from [32, 33] which are included within the performance evaluation platform. The effects of large-scale fading which is thoroughly described in [1] will not be covered in this dissertation. Popular models used in the industry to emulate large-scale fading are the modified Okumura model, Lee model, Longley-Rice model and the COST231 model [1, 34–37].

The second part of this chapter discusses the mobile WiMAX standard [8, 9] and how the developed simulator conforms to the standard. The inherent scalability of the OFDMA modulation scheme [8, 32], makes it widely considered to be the physical layer of choice in the use of mobile WiMAX [1, 38] and will be the air interface used in this dissertation. The chapter continues by explaining the limiting characteristics of using OFDM as a modulation scheme and illustrates its shortcomings. The chapter is concluded with an explanation of the construction of a mobile WiMAX simulation platform that will exert realistic system parameters and can be used as a baseline for all simulation conclusions.

2.2 ADDITIVE WHITE GAUSSIAN NOISE CHANNEL

In the design of a system that transfers information through a communication medium, it is always convenient to construct a mathematical model to analyze the communication medium. This mathematical model should reflect all the characteristics of the transmission medium [39]. Bearing this in mind, the fundamental AWGN physical channel will be addressed first. This channel is an additive statistical model and only the first and second moment of the process is required. The AWGN channel model is applied as

$$r(t) = x(t) + \eta(t), \tag{2.1}$$

where $x(t)$ denotes the transmitted symbol and $r(t)$ the received symbol. The received symbol is corrupted by the communication channel and the AWGN process $\eta(t)$ has a probability density function (PDF) that is Gaussian distributed as

$$p(\eta(t)) = \frac{1}{\sqrt{2\pi}\sigma_{\eta(t)}} \exp\left(-\frac{(\eta(t)-m_{\eta(t)})^2}{2\sigma^2_{\eta(t)}}\right), \tag{2.2}$$

with mean $m_{\eta(t)}$ and variance of $\sigma^2_{\eta(t)}$. The power spectral density (PSD) of the process $\eta(t)$ is a constant double-sided flat spectrum for the entire frequency spectrum and is a memoryless process. The induced entropy for the corresponding AWGN process that is given by [30] as

$$H(\eta(t)) = \frac{1}{2}\log_2(2\pi e\sigma^2_{\eta(t)}), \tag{2.3}$$

with the natural number e=2.7183. All of the above mentioned properties of the AWGN process is important in this analysis and will become more apparent later in this dissertation.

2.3 MOBILE FADING CHANNELS

A more sophisticated mathematical model was required when analyzing a more complex communication system. The first characteristic behind electromagnetic wave propagation is the reflection, diffraction and scattering of these waves [1, 40, 41]. Two classifications, large-scale and small-scale propagation, can be identified from these three characteristics and both are always present in any mobile wireless channel.

Large-scale propagation models are traditionally focused on predicting the average received signal strength within a given environment with the displacement between the two stations as

reference. This is accomplished through the construction of a statistical propagation model by matching a semi-empirical model to a large sample set of field measurements. To each fitted model a degree of confidence can be assigned to verify the accuracy of the model [1, 34]. This attenuation factor is the path loss experienced in the system and should be taken into consideration when calculating the link budget of the communication link [34]. The focus of this dissertation is not to calculate the link budget and for this reason only small-scale propagation was evaluated.

Small-scale fading is used to classify the rapid fluctuation in the received RF signal over a short period of time. This rapid fluctuation is caused by numerous contributors, namely the motion of the receiving device, the current environmental scatterers and the dynamic change in the environment that influence the propagation of these electromagnetic waves. These contributing factors present multiple versions of the same transmitted signal to the receiver with a varying delay profile. This small-scale fading, or simply fading, in the communication medium is mathematically expressed as

$$r(t) = \sum_{k=1}^{L} a_k \, \alpha(t) x(t - \tau_k) + \eta(t), \tag{2.4}$$

where $Eq.$ (2.4) is an extension to $Eq.$ (2.1). The physical factors given in $Eq.$ (2.4) that influence the properties of the small-scale propagation of electromagnetic radio waves are explained in the following sections.

2.3.1 Small-scale Fading Channel Parameters

2.3.1.1 Rayleigh Fading Distribution

Modern communication standards are designed to cater for the user's needs and operational environment. The packet structure and carrier frequency of mobile WiMAX is ideal for mobile NLOS communication, which the typical subscriber station (SS) experiences. Fading distribution for small-scale propagation in a line of sight (LOS) transmission are closely correlated to a Ricean distribution and as the LOS component strengthens, the distribution converges to a Gaussian distribution [42]. But for the typical mobile WiMAX user the Rayleigh distribution is of interest, because it possesses the statistical time varying nature of the non light of sight (NLOS) communication link [1, 30, 39, 40, 42]. This fading component denoted as $\alpha(t)$ in $Eq.$ (2.4) on page 8 has an amplitude PDF as

$$p(\alpha(t)) = \begin{cases} \frac{\alpha(t)}{\sigma^2_{r(t)}} \exp\left(-\frac{\alpha^2(t)}{2\sigma^2_{r(t)}}\right) & 0 \leq \alpha(t) \leq \infty, \\ 0 & \alpha(t) < 0. \end{cases} \tag{2.5}$$

Where $\sigma_{r(t)}$ is the root mean square (RMS) [1] value of the received signal $r(t)$ before envelope detection and $\sigma^2_{r(t)}$ is the average power of $r(t)$ before envelope detection. The statistical mean $m_{\alpha(t)}$ is given as

$$m_{\alpha(t)} = \mathrm{E}[\alpha(t)] = \sqrt{\frac{\pi}{2}}\sigma_{r(t)} = 1.253314\,\sigma_{r(t)}, \tag{2.6}$$

and the variance is equal to

$$\sigma^2_{\alpha(t)} = \mathrm{E}[\alpha^2(t)] - \mathrm{E}^2[\alpha(t)] = \left(2 - \sqrt{\frac{\pi}{2}}\right)\sigma^2_{r(t)} = 0.429204\,\sigma^2_{r(t)}. \tag{2.7}$$

The phase $\theta_{\alpha(t)}(t)$ of the frequency non-selective fading signal $\alpha(t)$ is uniformly distributed over $[0, 2\pi)$ and is given in [1, 30, 39, 40] as

$$p(\theta_{\alpha(t)}(t)) = \frac{1}{2\pi} \quad -\pi \leq \theta_{\alpha(t)}(t) \leq \pi. \tag{2.8}$$

2.3.1.2 Coherence Bandwidth

The coherence bandwidth B_c is a measure of the bandwidth over which the channel's frequencies have a high correlation in amplitude variation and phase shifts. This implies that all the used carrier frequencies within the coherence bandwidth [1, 30, 39, 43] will fade simultaneously and can be calculated as

$$B_c = \frac{1}{\beta_{cb}\sigma_\tau}. \tag{2.9}$$

Where the RMS delay spread is denoted by σ_τ [1] and the degree of correlation between frequencies within a given bandwidth is denoted by $\beta_{cb} \in \mathbb{R}^+$.

2.3.1.3 Doppler Spread

The motion of the subscriber station generates a Doppler frequency shift f_{cD} on the carrier frequency f_c [1]. The amount of frequency shift exerted on the carrier frequency can be calculated as

$$f_{cD} = \frac{v_{ss}\, f_c}{c} \cos(\theta_{ss}), \tag{2.10}$$

with v_{ss} as the velocity of the SS while assuming the basestation (BS) is stationary. The angle of displacement between the SS and the BS is presented by θ_{ss} and the carrier frequency by f_c of the communication system. A design parameter is to determine the maximum operable speed for a mobile WiMAX subscriber station and from this derive the maximum expected Doppler frequency shift and is expressed as $f_D = \max(f_{cD})$. Doppler spread B_D is the measure of spectral broadening of a single spectrum in a band of frequencies. The Doppler power spectrum for a continuous wave (CW) carrier can be well approximated by the following PSD [1, 34]

$$S_{x(t)}(f) = \begin{cases} \frac{\sigma^2_{x(t)}}{\pi\sqrt{f_D^2-(f-f_c)^2}} & \text{if } |f-f_c| \leq f_D, \\ 0 & \text{if } |f-f_c| > f_D. \end{cases} \tag{2.11}$$

Coherence time T_c is a statistical measure of a time period in a transmission sequence over which the channel impulse response (CIR) remains invariant. The coherence time is inversely proportional to the Doppler spread [1] of the channel and is expressed as

$$T_c = \frac{\beta_{ct}}{B_D}. \tag{2.12}$$

With $\beta_{ct} \in \mathbb{R}^+$ for a degree of correlation between amplitudes within a given time period.

2.3.1.4 Rate of Fading Fluctuation

Depending on the rate of fluctuation in the received sequence compared to the frequent changes in the communication channel, the channel can be classified into either a fast or slow fading channel. A channel is classified as fast fading when the time duration of the transmitted sequence $T_{x(t)}$ is longer than the coherence time T_c of the channel and the transmission bandwidth $B_{x(t)}$ is smaller than the Doppler spread B_D [1]. On the other hand a channel is classified as slow fading when the time duration of the transmitted sequence $T_{x(t)}$ is much shorter than the coherence time T_c of the channel and the transmission bandwidth $B_{x(t)}$ is larger than the Doppler spread B_D [1]. The properties of both classifications is given in summary as

$$\begin{aligned} \text{Fast fading} \rightarrow \quad & T_{x(t)} > T_c, \quad B_{x(t)} < B_D, \\ \text{Slow fading} \rightarrow \quad & T_{x(t)} \ll T_c, \quad B_{x(t)} \gg B_D. \end{aligned} \tag{2.13}$$

2.3.1.5 Multipath Propagation

The environment presents many points for reflection, diffraction and scattering for all propagating signals. These scatterers support multiple paths for signal propagation to the receiving antenna of the subscriber station. These multiple versions of the same transmitted sequence arrives at the receiving antenna on different propagating paths. Each propagating path has a different distance, arrival time, arrival angle and phase orientation [44] to the other paths. This multipath propagation is expressed as

$$r(t) = \sum_{k=1}^{L} a_k x(t - \tau_k) + \eta(t). \tag{2.14}$$

Hence the received signal consist of L multipath versions of the signal $x(t)$, where each version is attenuated from an index value in vector $\{a\}$ and delay by the same index value in vector $\{\tau\}$. These two vectors are obtained from the dynamic environment that induces different combinations of how the signal propagates and is known as the power delay profile (PDP). Either constructive or destructive combinations can be observed during the process of combining the multiple versions of the transmitted sequence and results in the fluctuations within the received sequence. The combination of delayed sequences are known as intersymbol interference (ISI) and will either extend or shorten the duration of the symbol.

2.3.2 Multipath Fading

Depending on the bandwidth of the signal and the delay spread [1], a system will experience different delays in the propagating paths at the receiving antenna. These different delays in the propagating paths divides the communication channel into two classifications.

$$\begin{aligned} \text{Frequency Non Selective Fading} \rightarrow \quad & B_{x(t)} \ll B_c, \quad T_{x(t)} \gg \sigma_\tau, \\ \text{Frequency Selective Fading} \quad \rightarrow \quad & B_{x(t)} > B_c, \quad T_{x(t)} < \sigma_\tau, \end{aligned} \tag{2.15}$$

where $T_{x(t)}$ is the symbol time period, $B_{x(t)}$ is the bandwidth of the signal, σ_τ is the RMS delay spread and B_c is the coherence bandwidth of the communication channel. Frequency non-selective fading preserves the spectral characteristics of the transmitted signal over the channel, but due to the multipath propagation within the environment the signal strength will fluctuate in gain at the receiver. The most common amplitude distribution for a frequency non-selective channel is the Rayleigh distribution. In a frequency selective fading channel the

spectral characteristics are altered and the outcome is that various frequency gains are expected over the entire channel bandwidth.

2.4 WiMAX PLATFORM

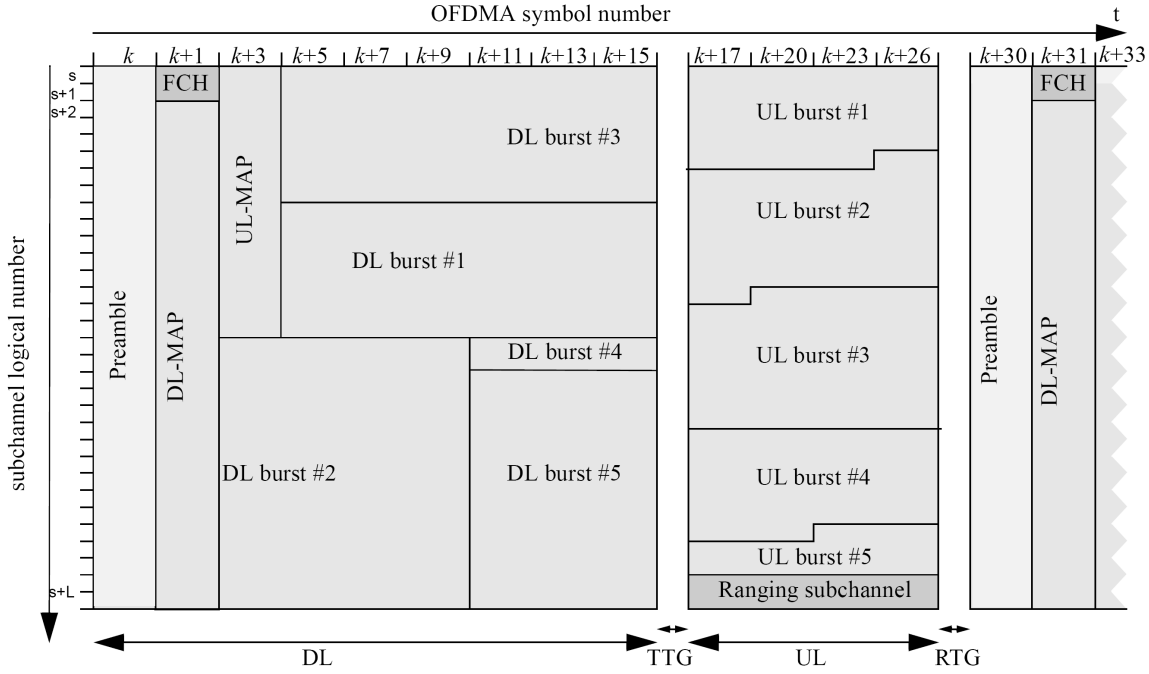

FIGURE 2.1: One OFDMA TDD time frame.

WiMAX (IEEE 802.16) is a technology for broadband wireless communication that incorporates OFDM modulation to transfer data at high rates over a communication channel. The WiMAX standard provides both licence and licence exempted bands for the industry. The Wireless MAN OFDMA air-interface for IEEE 802.16e-2005 will be the focus in this chapter and this air-interface offered by the WiMAX standard operates in the 2.5 GHz spectrum. This frequency band operates below the 11 GHz sprectrum and is subjected to the physical environment where the wavelength is long enough to support a NLOS transmission, with multipath propagation becoming a significant impairment. The simulation platform designed in this dissertation incorporates a Wireless MAN OFDMA air interface which includes all the following features:

- Scalable OFDMA [45] to support multiple channel bandwidths from 1.25 to 20 MHz.
- Support TDD transmission and frame support.

- Conforms to the mobile packet format.
- FUSC operation mode is supported.
- Support waterfilling over all subcarriers.
- Support adaptive modulation schemes.

The WiMAX simulator with default settings is available at http://opensource.ee.up.ac.za/.

2.4.1 Modulator

A OFDM system with channel equalization is illustrated in figure 2.2 [8, 9]. The first step in transmission is to obtain N modulated symbols in the frequency domain. The modulation scheme of the data carriers is determined by the channel conditions and quality of the RF signal. In the downlink bursts the BS support 4-QAM (QPSK), 16-QAM and 64-QAM modulation schemes. With good channel conditions the more complex 64-QAM modulation scheme is used, and as lower RF signal quality is experienced the less complex modulation schemes are used. In an initial study [46] it was shown that WiMAX operates 86.01% of the time in the 4-QAM mode, 10.48% of the time in the 16-QAM mode and 0.8% of the time in 64-QAM mode. There is also 2.7% probability that WiMAX is in an unoperable region.

The simplest method to construct a QAM signal is to impress separate information bits on each of the quadrature carriers and assign them using a gray coding scheme [8, 9]. The two quadrature carriers are the inphase and quadrature carriers [39] and are multiplexed to obtain the transmitted signal waveform in the frequency domain [39, 47] as

$$s_n(f) = A_{mc} g_F(f) cos(2\pi f_c f) + A_{ms} g_F(f) sin(2\pi f_c f) \quad n = 1, \ldots, N. \tag{2.16}$$

Where $\{A_{mc}\}$ and $\{A_{ms}\}$ are the sets of amplitude levels that are obtained by mapping k-bit sequences into signal amplitudes and $g_F(f)$ is the frequency pulse shaping filter. The length of the k-bit sequence for a M-QAM constellation is given by

$$k = \log_2(M). \tag{2.17}$$

Rectangular QAM constellations [8] have a distinct advantage of being generated as two PAM signals that are impressed onto the two quadrature carriers and leads to ease of modulation and

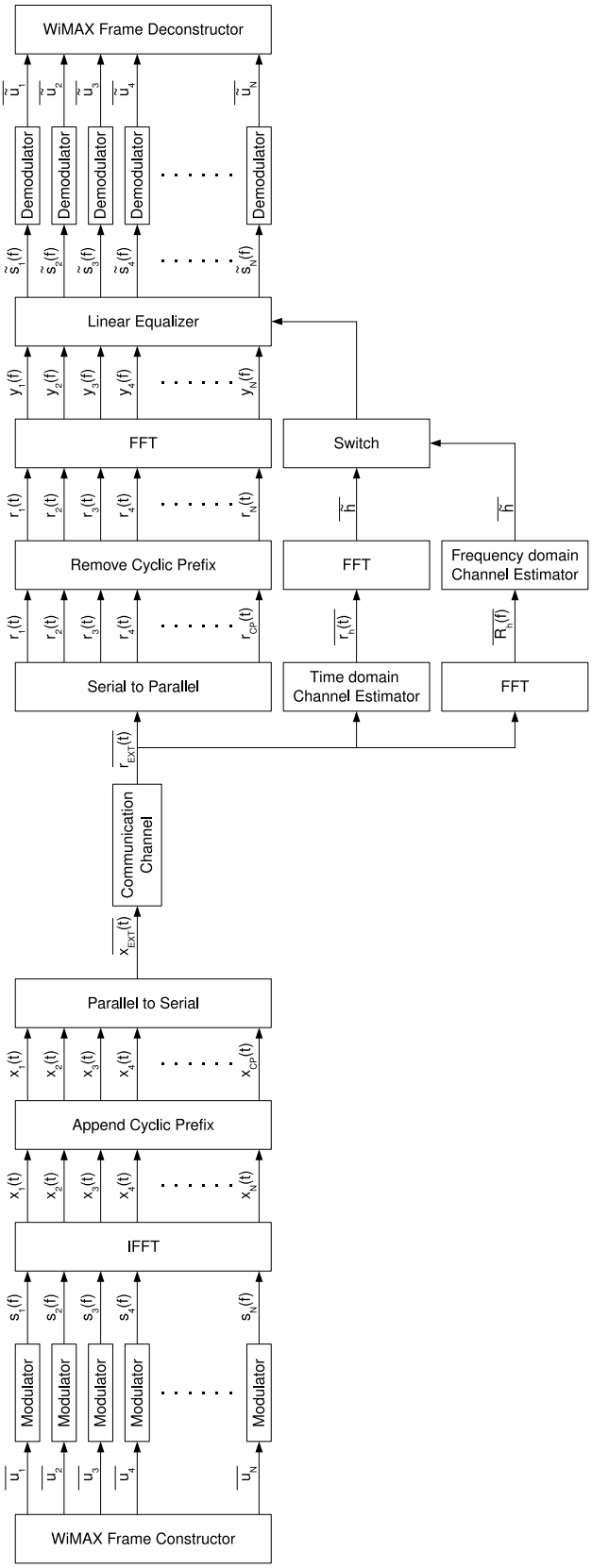

FIGURE 2.2: OFDMA system with channel estimation and equalization.

demodulation in the system. There exist two methods of demodulating a signal constellation, namely hard decision and soft decision demodulation.

Both decision methods induce the same probability of symbol error for a M-QAM constellation when no coding is applied and is given in [30] as

$$P_M = 1 - \left(1 - 2\left(1 - \frac{1}{\sqrt{M}}\right)Q\left(\sqrt{\frac{3E_{av}}{(M-1)N_0}}\right)\right)^2 \quad \text{for } k \text{ even.} \tag{2.18}$$

With E_{av}/N_0 denoting the average signal-to-noise ratio (SNR) per symbol. Both decision methods will be discussed in the following sections.

2.4.1.1 Hard Decision Detection

The function of the demodulator in Figure 2.2 on page 14, is to make a decision on each of the received symbols based on the observation of $\tilde{s}_n(f)$, $n \in [1, N]$ for all the subcarriers. The decision criterion is based on maximum aposteriori probability (MAP) and selects the signal corresponding to the highest posterior probability in the set of posterior probabilities $\{P(s_{n,m}(f)|\tilde{s}_n(f))\}$ [39]. Using Baye's rule the MAP detection can be expressed as

$$P(s_{n,m}(f)|\tilde{s}_n(f)) = \frac{p(\tilde{s}_n(f)|s_{n,m}(f))P(s_{n,m}(f))}{p(\tilde{s}_n(f))}, \quad m \in [1, M]. \tag{2.19}$$

where $p(\tilde{s}_n(f)|s_{n,m}(f))$ is the conditional PDF that $\tilde{s}_n(f)$ is observed on subcarrier n, given that symbol $s_{n,m}(f)$ was transmitted. The symbol $s_{n,m}(f)$ presents the m^{th}-QAM symbol, $m \in [1, M]$, that was transmitted over the n^{th} subcarrier. By expanding on $Eq.$ (2.19) we obtain the following

$$P(s_{n,m}(f)|\tilde{s}_n(f)) = \frac{p(\tilde{s}_n(f)|s_{n,m}(f))P(s_{n,m}(f))}{\sum_{m=1}^{M} p(\tilde{s}_n(f)|s_{n,m}(f))P(s_{n,m}(f))}, \quad m \in [1, M]. \tag{2.20}$$

With perfect source encoding the a priori probability $P(s_{n,m}(f))$ for the m^{th}-QAM symbol being transmitted is assumed to be equal probable; i.e., $P(s_{n,m}(f)) = 1/M$, $\forall\ m$. By substituting equal probable symbols into $Eq.$ (2.20) we acquire the expression as

$$P(s_{n,m}(f)|\tilde{s}_n(f)) = \frac{\frac{1}{M}\, p(\tilde{s}_n(f)|s_{n,m}(f))}{\frac{1}{M}\ \sum_{m=1}^{M} p(\tilde{s}_n(f)|s_{n,m}(f))}, \quad m \in [1, M], \tag{2.21}$$

that simplifies to

$$P(s_{n,m}(f)|\tilde{s}_n(f)) = \frac{p(\tilde{s}_n(f)|s_{n,m}(f))}{\sum_{m=1}^{M} p(\tilde{s}_n(f)|s_{n,m}(f))}, \quad m \in [1, M]. \tag{2.22}$$

When evaluating an AWGN channel, $Eq.$ (2.22) can be written as

$$P(s_{n,m}(f)|\tilde{s}_n(f)) = \beta_{qam} \cdot \left(\frac{1}{\sqrt{2\pi}\sigma_{\eta(t)}} \exp\left(- \frac{D(\tilde{s}_n(f), s_{n,m}(f))}{2\sigma^2_{\eta(t)}} \right) \right), \tag{2.23}$$

with β_{qam} given as

$$\beta_{qam} = \left(\sum_{m=1}^{M} \frac{1}{\sqrt{2\pi}\sigma_{\eta(t)}} \exp\left(- \frac{D(\tilde{s}_n(f), s_{n,m}(f))}{2\sigma^2_{\eta(t)}} \right) \right)^{-1}. \tag{2.24}$$

$D(\tilde{s}_n(f), s_{n,m}(f))$ denotes the euclidean distance between the symbols $\tilde{s}_n(f)$ and $s_{n,m}(f)$. To maximize $P(s_{n,m}(f)|\tilde{s}_n(f))$, the distance vector $D(\tilde{s}_n(f), s_{n,m}(f))$ must be minimized. In summary, only a set $\{m\}$, $m \in [1, M]$ euclidean distances must be computed and then select the symbol corresponding to the shortest distance to obtain the most likely symbol transmitted and decode the corresponding binary sequence for the receiver. This hard decision detection for each subcarrier n is given by

$$\widetilde{\overline{u_n}} = HD(\overline{u_n}|\tilde{s}_n(f)) = \min_{m=1}^{M} \left(D(\tilde{s}_n(f), s_{n,m}(f)) \right), \quad n \in [1, N]. \tag{2.25}$$

2.4.1.2 Soft Decision Detection

By substituting a hard decision detector with a soft decision detector, system complexity is increased. Soft decision detection starts with the same MAP algorithm for symbol detection as shown in $Eq.$ (2.20). By assuming all the same parameter as in section 2.4.1.1, the symbol probability is

$$P(s_{n,m}(f)|\tilde{s}_n(f)) = \frac{p(\tilde{s}_n(f)|s_{n,m}(f))P(s_{n,m}(f))}{\sum_{m=1}^{M} p(\tilde{s}_n(f)|s_{n,m}(f))P(s_{n,m}(f))}, \quad m \in [1, M]. \tag{2.26}$$

Assuming again equal probable symbol transmission we express $Eq.$ (2.26) as

$$P(s_{n,m}(f)|\tilde{s}_n(f)) = \frac{\frac{1}{M} p(\tilde{s}_n(f)|s_{n,m}(f))}{\frac{1}{M} \sum_{m=1}^{M} p(\tilde{s}_n(f)|s_{n,m}(f))}, \quad m \in [1, M], \tag{2.27}$$

that simplifies to

$$P(s_{n,m}(f)|\tilde{s}_n(f)) = \frac{p(\tilde{s}_n(f)|s_{n,m}(f))}{\sum_{m=1}^{M} p(\tilde{s}_n(f)|s_{n,m}(f))}, \quad m \in [1, M]. \tag{2.28}$$

When evaluating an AWGN channel, $Eq.$ (2.28) can be written as

$$P(s_{n,m}(f)|\tilde{s}_n(f)) = \beta_{qam} \cdot \left(\frac{1}{\sqrt{2\pi}\sigma_{\eta(t)}} \exp\left(- \frac{D(\tilde{s}_n(f), s_{n,m}(f))}{2\sigma^2_{\eta(t)}} \right) \right), \tag{2.29}$$

with β_{qam} given as

$$\beta_{qam} = \left(\sum_{m=1}^{M} \frac{1}{\sqrt{2\pi}\sigma_{\eta(t)}} \exp\left(- \frac{D(\tilde{s}_n(f), s_{n,m}(f))}{2\sigma^2_{\eta(t)}} \right) \right)^{-1}. \tag{2.30}$$

The hard decision detection chooses the most probable symbol and demodulates the symbol to the correct binary sequence given a symbol constellation map. The main difference for a soft decision detection is that instead of demodulating to a binary information stream, the soft decision detector calculates the corresponding bit probability for each bit in the binary sequence. The soft decision detection for the probability of the j^{th} bit being a 1 in vector $\overline{\tilde{u}_n}$ for each subcarrier n is

$$\overline{\tilde{u}_n}(j) = SD(\overline{u_n}(j)|\tilde{s}_n(f)) = \sum_{m=1}^{M} P(s_{n,m}(f)|\tilde{s}_n(f)) \cdot P(\overline{u_n}(j) = 1|s_{n,m}(f)), \tag{2.31}$$

where $P(\overline{u_n}(j) = 1|s_{n,m}(f))$ is the probability that the binary sequence mapped to symbol $s_{n,m}(f)$ has a binary value of 1 in position j. $Eq.$ (2.31) must be computed $K = \log_2(M)$ times to obtain the complete $\overline{\tilde{u}_n}(j)$ vector and is expressed as

$$\{\overline{\tilde{u}_n}(j)\} = \left\{ SD(\overline{u_n}(1)|\tilde{s}_n(f)) \, ; SD(\overline{u_n}(2)|\tilde{s}_n(f)) \, ; \ldots ; SD(\overline{u_n}(K)|\tilde{s}_n(f)) \right\}. \tag{2.32}$$

$Eq.$ (2.32) is used to calculate each bit probability of being a 1. The bit probability of 0 for each bit is calculated as

$$P(\overline{u_n}(j) = 0) = 1 - P(\overline{u_n}(j) = 1), \quad j = 1, 2, \ldots, \log_2(M). \tag{2.33}$$

2.4.2 OFDM Modulation

The approach of OFDM is to subdivide the available channel bandwidth into a number of equal size orthogonal bands of subcarriers. This subdivision provides N bands where different information symbols can be transmitted simultaneously on the N subcarriers. WiMAX is designed that each subcarrier band f_{SC} must have a bandwidth size of 10.49KHz. This size of bandwidth satisfies the following inequality [8] of

$$f_D \ll f_{SC} \ll \frac{1}{\sigma_\tau}. \tag{2.34}$$

With the maximum Doppler frequency shift denoted by f_D and the RMS delay spread denoted by σ_τ. Synchronizing subcarriers for orthogonality [8, 9, 39] and mitigating the effect of ISI is optimized if $Eq.$ (2.34) holds as a design parameter.

The OFDM modulator and demodulator can be impletemented by use of a parallel bank of filters or when the number of subcarriers are large, typically $N > 25$, it would be more efficient to implement the modulator and demodulator using a fast Fourier transform (FFT) algorithm [39]. The OFDM modulation of the N subcarriers, which is the inverse fast Fourier transform (IFFT) function [47, 48] is given as

$$x_j(t) = \frac{1}{N}\sum_{k=1}^{N} s_k(f)\,\exp\left(\frac{2\,i\,\pi(j-1)(k-1)}{N}\right), \qquad j \in [1, 2, \ldots, N], \tag{2.35}$$

and the OFDM demodulation, which is the FFT function [47, 48] is given as

$$y_k(f) = \sum_{j=1}^{N} r_j(t)\,\exp\left(\frac{-2\,i\,\pi(k-1)(j-1)}{N}\right), \qquad k \in [1, 2, \ldots, N]. \tag{2.36}$$

The next major design parameter to discuss is the transmission of OFDM symbols with the restrictive high PAPR characteristic [39, 49–51]. A characteristic of OFDM is that the modulation seldomly exerts excessive high amplitude peaks. These high amplitudes are caused by the symbols in the N subcarriers that add constructively in phase with each other in the frequency domain. Proper rollback in the transmission power of the communication system must be adhered to in order to ensure that the high power amplifier (HPA) does not saturate in the operation region. This operational region for the HPA is defined as

$$x_j(t) = \begin{cases} x_j(t) & \text{if } x_j(t) \leq x_{saturated}(t), \\ x_{saturated}(t) & \text{if } x_j(t) > x_{saturated}(t). \end{cases} \tag{2.37}$$

Where $x_{saturated}(t)$ denotes the saturation point of the HPA in the linear operating region. For illustration purposes the operation region of an amplifier is shown in Figure 2.3 on page 19. The first notable difference is the operational regions of the ideal amplifier and the HPA. The saturation point is the maximum amplification where the amplification predictability of the HPA still corresponds to the ideal amplifier. To ensure no corruption of the OFDM symbols occur at the transmitter end, the highest peak amplitude value for a given OFDM modulation is set to the saturation point of the amplifier. This is accomplished by backing off in the power of the operation point (average OFDM power) until the highest peak amplitude value is less than or equal to the amplifier's saturation point. This back off region is also shown in Figure 2.3 and illustrates the massive loss in amplification gain in the usage of OFDM as a modulation scheme.

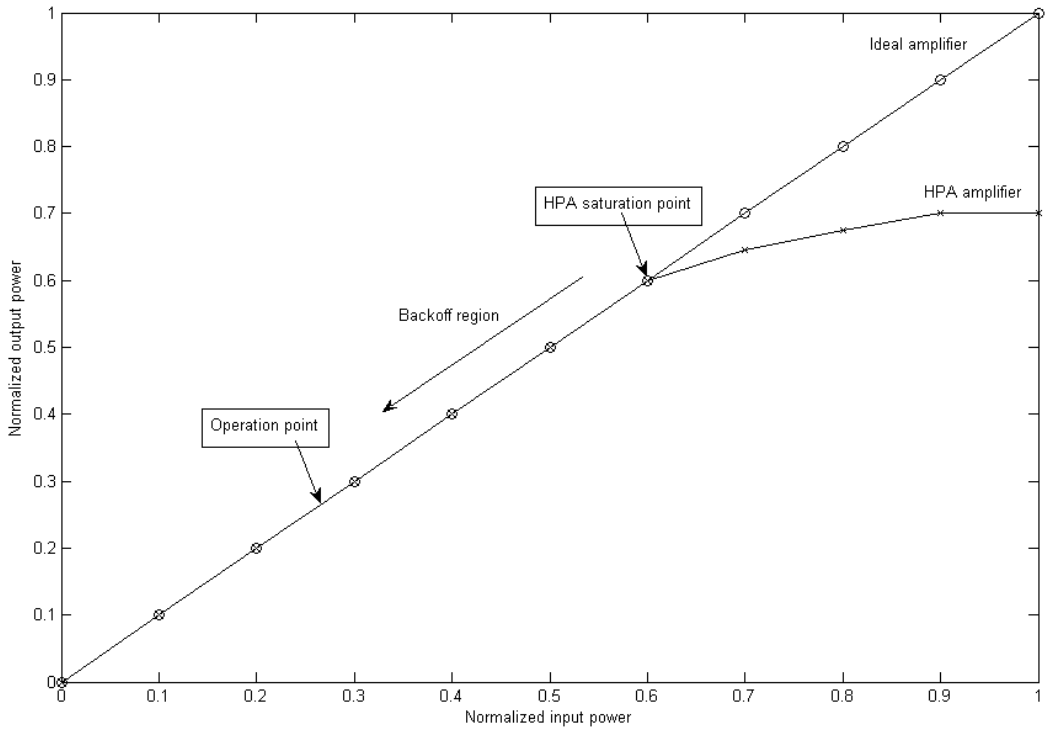

FIGURE 2.3: Operational region of HPA.

Definition 2.4.1 *OFDM modulating N-subcarriers in the frequency domain, will create an OFDM symbol that is compiled of N discrete complex time symbols.*

The transmitter's HPA saturates when the transmission symbols are amplified and the high amplitude values are amplified beyond the HPA's saturation point. By peak clipping a set of

time symbols in an OFDM symbol will result in a complete distortion of the symbols $y_k(f)$, $k \in [1, N]$ in the frequency domain. This is commonly referred to as inband distortion and outband smearing of the transmission band in the frequency spectrum [1, 8–10, 39] and this distortion at the receiver is expressed as

$$y_k(f) = \sum_{j=1\setminus j'}^{N} r_j(t) \exp\left(\frac{-2\,i\,\pi(k-1)(j-1)}{N}\right) + \sum_{j'=1\setminus j}^{N} r_{j'}(t) \exp\left(\frac{-2\,i\,\pi(k-1)(j'-1)}{N}\right). \tag{2.38}$$

Where the k^{th} subcarriers at the receiver is presented by $y_k(f)$. The first summation in $Eq.$ (2.38) on the right is the set of symbols of received values $r_j(t)$ that are not saturated and the second summation is the set of saturated symbols in the the received OFDM symbol denoted by $r_{j'}(t)$. The communication channel was omitted in Figure 2.4 to illustrates the effect that a saturated HPA has on the transmitted signal. The horizontal lines in the figure are the preset saturation level of the HPA.

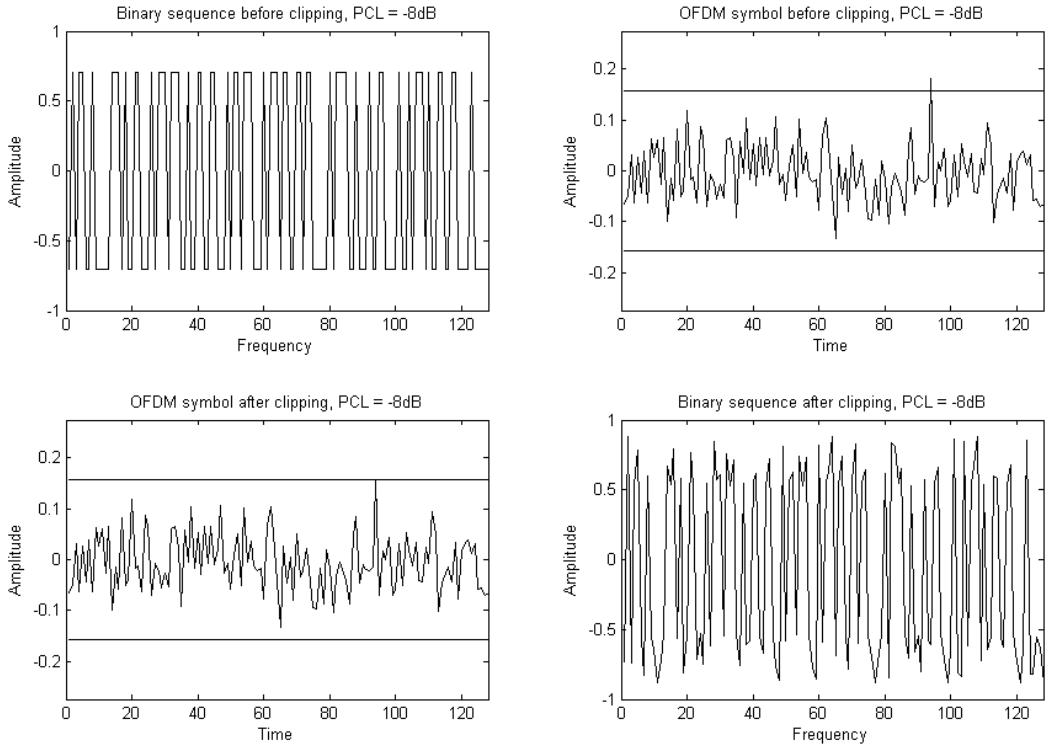

FIGURE 2.4: OFDM system with -8dB clip in the HPA.

It is observed in Figure 2.4 that by clipping a single time instance effects the entire OFDM symbol and these effects have been well researched in [49, 50]. An emphirical graph running 1

Tera samples, is plotted in Figure 2.5 on page 21 for an OFDM system using a 128-point FFT and a E_b/N_0 of 0 dB with various peak clipping levels.

It is concluded from the empirical graph presented in Figure 2.5, that there is no serious performance degradation for peak clipping levels above -7.5 dB in the saturation point for a 128-point FFT OFDM system. The foundation for this is the increase in number of clipping occurrences in all the OFDM symbols. Filters can be placed to limit the out band smearing but other techniques need to be used to bring the inband distortion down and will be discussed later in this dissertation (see section 4.10).

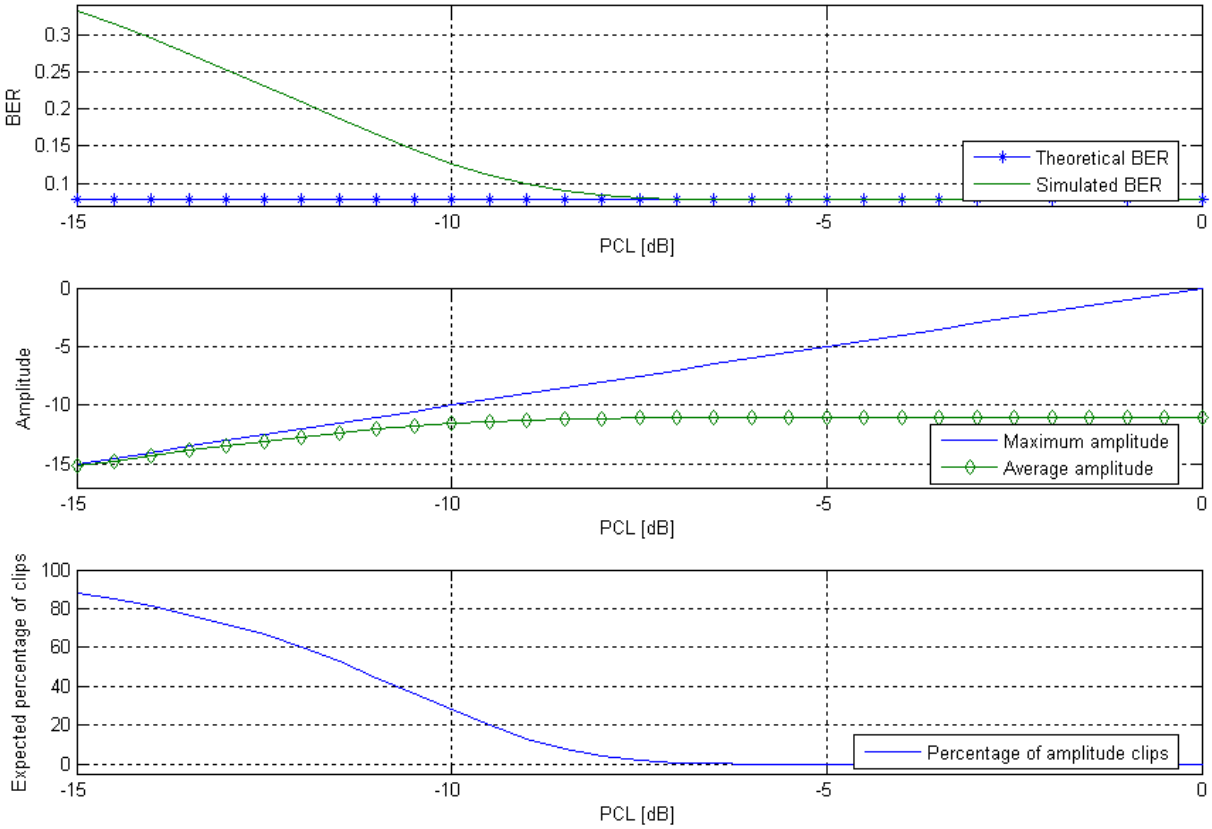

FIGURE 2.5: Simulated statistics of an OFDM system.

2.4.3 Channel Estimation and Equalization

The advantage of using OFDM as modulation scheme is the ability to mitigate the effects of multipath propagation. This is acquired by accurately estimating the channel impulse response (CIR) from the reference symbols [52]. The CIR is used to equalize the data symbols in an OFDM symbol [38]. This process is realized by appending a cyclic prefix (CP) to the OFDM

symbol before transmission [8, 9]. The CP is a copy of the last fraction of time symbols and is illustrated in Figure 2.6.

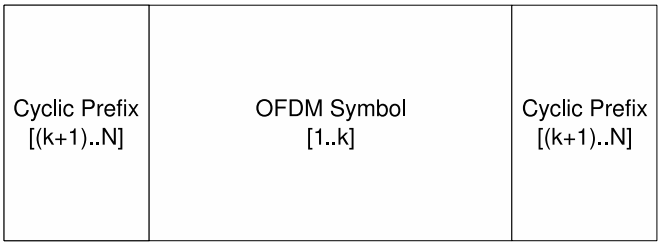

FIGURE 2.6: OFDM symbol with cyclic prefix appended.

The CP is compulsory in mobile WiMAX[1] and needs to be included in the analysis of this dissertation even though channel estimation and equalization is not the focus. The appending of the CP to each transmission sequence reduces system's bandwidth utilization [8, 9] and this loss in signal to noise ratio is denoted as

$$Loss_{cp}\,[\mathrm{dB}] = 10\log_{10}\left(1 - \frac{T_{cp}}{T_{\mathrm{x}} + T_{cp}}\right). \tag{2.39}$$

With the transmission time of the CP and OFDM symbol denoted as T_{cp} and T_{x} respectively. The typical losses experienced in mobile WiMAX is tabulated in table 2.1 as

TABLE 2.1: Power loss in mobile WiMAX

Cyclic prefix length	**Power loss**
CP = $\frac{1}{4}$	-0.9691 dB
CP = $\frac{1}{8}$	-0.5115 dB
CP = $\frac{1}{16}$	-0.2632 dB
CP = $\frac{1}{32}$	-0.1336 dB

It should be noted that this is a neccessary loss in bandwidth utilization for the gain in BER performance over a communication system in a multipath propagation environment that uses no equalization. It was for this reason that the bandwidth addition is included in all simulation results to make a fair comparison to other technologies.

[1] Mobile WiMAX supports cyclic prefix length of $\frac{1}{4}$, $\frac{1}{8}$, $\frac{1}{16}$ and $\frac{1}{32}$

2.5 SIMULATING A MOBILE FADING CHANNEL

2.5.1 Simulating an AWGN Channel

This section gives a description on how to generate accurate AWGN noise samples and how these samples are scaled by their variance to obtain a specific quantity of energy per bit for a normalized noise band at the receiver (E_b/N_0). In this dissertation a PDF transformation algorithm known as the Bray-Marsagalia algorithm [53] was used to transform a uniform amplitude PDF distribution into a Gaussian amplitude PDF with zero mean and unit variance. The two moments of the Gaussian process will be denoted as $\mathcal{N}(m_{\eta(t)}, \sigma^2_{\eta(t)})$ with mean $m_{\eta(t)}$ and variance $\sigma^2_{\eta(t)}$. The PDF transformation algorithm is only as strong as the uniformly generated samples that are used as inputs. The Wichmann-Hill algorithm [54, 55] was used to produce uniform distributed samples $U_{wh(t)} \in [0, 1]$. There exists two advantages in using the Wichmann-Hill algorithm as uniform number generator, the first is that the length of the repetition sequence can be extended without deteriorating the statistical properties [54]. The second advantage is that the uniform number generator can be adjusted to opertate on any hardware/software platform.

When investigating the performance of a communication system, most research characterizes the performance of the system by evaluating the BER for a given signal strength. The signal strength can either be expressed as a signal-to-noise ratio (SNR) or energy per bit to noise power ratio (E_b/N_0). The SNR is defined as the average signal power to noise power at the receiver [56]. Using the SNR quantity is meaningless if the noise equivalent bandwidth is not specified [40] and even then it is difficult to compare and analyze communication systems. Consequently the SNR is normalized as shown in [39, 40] to the E_b/N_0 quantity and will now be derived in this section to accommodate an OFDM communication platform. The following deriviation is an extention to the scaling factor derived in [40]. The following relationship between SNR and E_b/N_0 holds as

$$\mathrm{SNR} = \frac{\sigma^2_{x(t)}}{\sigma^2_{\eta(t)}} = \frac{E_b\, f_{bit}}{N_0 \int_0^\infty |H_{\mathrm{RX}}(f)|^2\, df} = \frac{E_c\, f_{bit}}{R_c\, N_0 \int_0^\infty |H_{\mathrm{RX}}(f)|^2\, df}, \tag{2.40}$$

where $\sigma^2_{x(t)}$ is the variance of the transmitted signal and $\sigma^2_{\eta(t)}$ is the variance of the required Gaussian distributed signal. The energy of a bit for an uncoded transmission stream is denoted by E_b, while the energy of a bit for a coded transmission stream is denoted by E_c. f_{bit} is the uncoded bit rate of the transmission signal and the code rate for the current coding scheme is

denoted by R_c. $H_{\mathrm{RX}}(f)$ is the frequency response of the receiver's noise limiting filter with the single sided PSD level of the AWGN channel denoted by N_0. $Eq.$ (2.40) can be written in terms of the required noise variance to normalize the SNR to E_b/N_0 as

$$\sigma^2_{\eta(t)} = \frac{\sigma^2_{x(t)} R_c \int_0^\infty |H_{\mathrm{RX}}(f)|^2 \, df}{\frac{E_c}{N_0} f_{bit}}. \tag{2.41}$$

Now if Gaussian variables are produced with a Gaussian generator [53] at a constant rate of f_{samp} [Hz], the effective noise bandwidth [40] for this generator is equal to

$$B_{ns} = \frac{f_{samp}}{2}. \tag{2.42}$$

The Gaussian amplitude samples are produced with unit variance and zero mean [53] and has the property [40] of

$$N_{ns} \cdot B_{ns} = \sigma^2_{ns(t)} = 1, \tag{2.43}$$

with N_{ns} denoting the single-sided PSD of the noise generated. By substituting $Eq.$ (2.43) into $Eq.$ (2.42) yields [40] a relation of

$$N_{ns} = \frac{2}{f_{samp}}. \tag{2.44}$$

This equates to the power of the Gaussian amplitude generator at the output of the receive filter as [40]

$$\sigma^2_{r(t)} = N_{ns} \int_0^\infty |H_{\mathrm{RX}}(f)|^2 \, df = \frac{2}{f_{samp}} \int_0^\infty |H_{\mathrm{RX}}(f)|^2 \, df. \tag{2.45}$$

The Gaussian amplitude generator was scaled by k_η [40] to obtain the required normalized noise bandwidth as expressed in $Eq.$ (2.41), with k_η given as

$$k_\eta = \frac{\sigma^2_{\eta(t)}}{\sigma^2_{r(t)}}. \tag{2.46}$$

By substituting $Eq.$ (2.41) and $Eq.$ (2.45) into $Eq.$ (2.46) the scaling factor k_η [40] is given as

$$k_\eta = \frac{\sigma^2_{x(t)} f_{samp}}{2 \, f_{bit} \, \frac{E_b}{N_0}}. \tag{2.47}$$

To incorporate an OFDM transmission system into the scaling factor k_η, some attributes of the system must first be discussed. The first extension is to include the power [48] of an OFDM symbol and is expressed as

$$\mathcal{P}_{x(t)} = \mathcal{F}^{-1}(\mathcal{P}_{s(f)}), \tag{2.48}$$

where $\mathcal{F}^{-1}$ denotes the OFDM modulator which is the IFFT function given in $Eq.$ (2.35). The power of $\mathcal{P}_{s(f)}$ can be computed [48] as

$$\mathcal{P}_{s(f)} = \lim_{F\to\infty} \frac{1}{2F} \int_{-F}^{F} |s(f)|^2 df. \tag{2.49}$$

Substituting $Eq.$ (2.49) and $Eq.$ (2.35) into $Eq.$ (2.48), the power in the time domain is expressed as

$$\mathcal{P}_{x(t)} = \lim_{N\to\infty} \frac{1}{N} \sum_{j=1}^{N} \left(\left| \frac{1}{N} \sum_{k=1}^{N} s_k(f) \exp\left(\frac{2\,i\,\pi(j-1)(k-1)}{N} \right) \right|^2 \right), \tag{2.50}$$

which equates to

$$\mathcal{P}_{x(t)} = \lim_{N\to N_{\mathrm{FFT}}} \frac{\mathcal{P}_{s(f)}}{N}. \tag{2.51}$$

The N_{FFT} denotes the number of subcarriers within the OFDM system and for mobile WiMAX these N_{FFT} values are typically 128, 512, 1024 and 2048 respectively. The second extension is to include the cyclic prefix that utilizes system bandwidth. The number of time symbols in an OFDM symbol is extended to

$$N_{\mathrm{Total}} = N_{\mathrm{FFT}} + N_{\mathrm{CP}}, \tag{2.52}$$

with N_{FFT} and N_{CP} denoting the number of samples in an OFDM symbols and the CP in the time domain respectively. The last extension is the uncoded bit rate f_{bit} in $Eq.$ (2.47) needs to be replaced by N_{bit} for the uncoded bit rate in an OFDM system. N_{bit} represents the parallel uncoded bit rate of all the subcarriers and is calculated by the summation of all the uncoded data rates in all the subcarriers in a single OFDM symbol and is expressed as

$$N_{bit} = \sum_{j=1}^{N} f_{bit,\,j}, \tag{2.53}$$

with $f_{bit,\,j}$ denoting the uncoded bit rate of j^{th} subcarrier. Thus the final power scaling factor in an OFDM modulation system for the required noise variance as a function of E_b/N_0 [dB] is given as

$$k_\eta = \frac{\sigma^2_{x(t)}.f_{samp}.(N_{\text{FFT}} + N_{\text{CP}})}{10^{(0.1.E_b/N_0)}.2.N_{\text{FFT}}.N_{bit}}. \tag{2.54}$$

Figure 2.7 on page 28 illustrates how the power scaling factor k_η is scaled to produce Gaussian noise samples with the correct variance required for a given E_b/N_0 value.

2.5.2 Simulating a Jakes Flat Fading Channel

When using a fading process to emulate a fading channel, the fading process should have statistical properties resembling a mobile fading channel's characteristics [42]. Well known algorithms have been presented in the literature [57, 58] and among all the contenders the two most well known mathematical reference models are the Clarke [59] and Jakes [60] model. Various implementations of both models have been proposed in the literature [40, 57, 58]. With the high sampling period required for the carrier frequency of mobile WiMAX, a deficiency was discovered in using the Clarke model with a time domain filter [40] and for this reason the Jakes model was implemented. Various improvements have been made to the Jakes model and the improved Jakes model [61] was used because it is the best sum-of-sinusoid [57, 58] model. The improved Jakes model is given as

$$Z(t) = Z_I(t) + i\, Z_Q(t), \tag{2.55}$$

with

$$Z_I(t) = \sqrt{\frac{2}{M}}\left(\sum_{n=1}^{M} \cos(2\pi f_D t \cos(\alpha_n) + \phi_n)\right), \tag{2.56}$$

$$Z_Q(t) = \sqrt{\frac{2}{M}}\left(\sum_{n=1}^{M} \cos(2\pi f_D t \sin(\alpha_n) + \varphi_n)\right), \tag{2.57}$$

$$\alpha_n = \frac{2\pi n - \pi + \theta}{4M}, \qquad \text{for } n \in [1, 2, \ldots, M]. \tag{2.58}$$

Where ϕ_n, φ_n and θ are statistically independent uniform distributed samples on $[-\pi, \pi)$ for all n and f_D is the maximum Doppler frequency. The statistical properties required for any fading process is given as

$$R_{Z_Q Z_Q} = R_{Z_I Z_I} = J_0(2\pi f_D \tau), \tag{2.59}$$

$$R_{Z_Q Z_I} = R_{Z_I Z_Q} = 0, \tag{2.60}$$

$$R_{ZZ} = 2J_0(2\pi f_D \tau), \tag{2.61}$$

where $J_0()$ denotes the zero-order Bessel function of the first kind. It is proved that the improved Jakes model [61] complies with all required statistical properties [61] given in $Eq.$ (2.59) - $Eq.$ (2.61). The last parameter that needs to be addressed is the number of sinusoids M. For best statistical properties $M \rightarrow \infty$, but in [61] it was proven that a good approximation of the process can be observed for $M \geq 8$. The next step is to extract channel state information from the process and supply it to the receiver. The fading amplitude is extracted from the fading model as

$$|Z(t)| = \sqrt{Z_I(t)Z_I(t) + Z_Q(t)Z_Q(t)}, \tag{2.62}$$

and the phase as

$$\angle(Z(t)) = \arctan\left(\frac{Z_Q(t)}{Z_I(t)}\right). \tag{2.63}$$

Channel State Information (CSI) obtained from $Eq.$ (2.62-2.63) can be used to supply the receiver with perfect CSI to optimize the channel coding technique. The process of estimating the fading process is not the focus of this dissertation and only perfect estimation will be used within the channel decoders at the receiver.

2.5.3 Simulating a Mobile Fading Channel

In Figure 2.7, an illustration to simulate a frequency selective fading channel [40] is given. The communication model is capable of emulating a time-invariant multipath fading channel with each of the L propagation paths which are independently faded. The communication channel operates by receiving a OFDM symbol $\overline{x_{ext}(t)}$, which has $N_{\text{FFT}} + N_{\text{CP}}$ complex baseband signal points that are copied onto each of the L propagation paths and are delayed and attenuated according to the PDP. In addition, each propagation path is independently flat faded according to receiver's sampling rate and mobile speed using the *Improved Jakes Model* [61] given by $Eq.$ (2.55) in section 2.5.2. To maintain orthogonality between all the subcarriers, the flat faded propagation path is assumed to be slowly time-varing [62] and is valid if

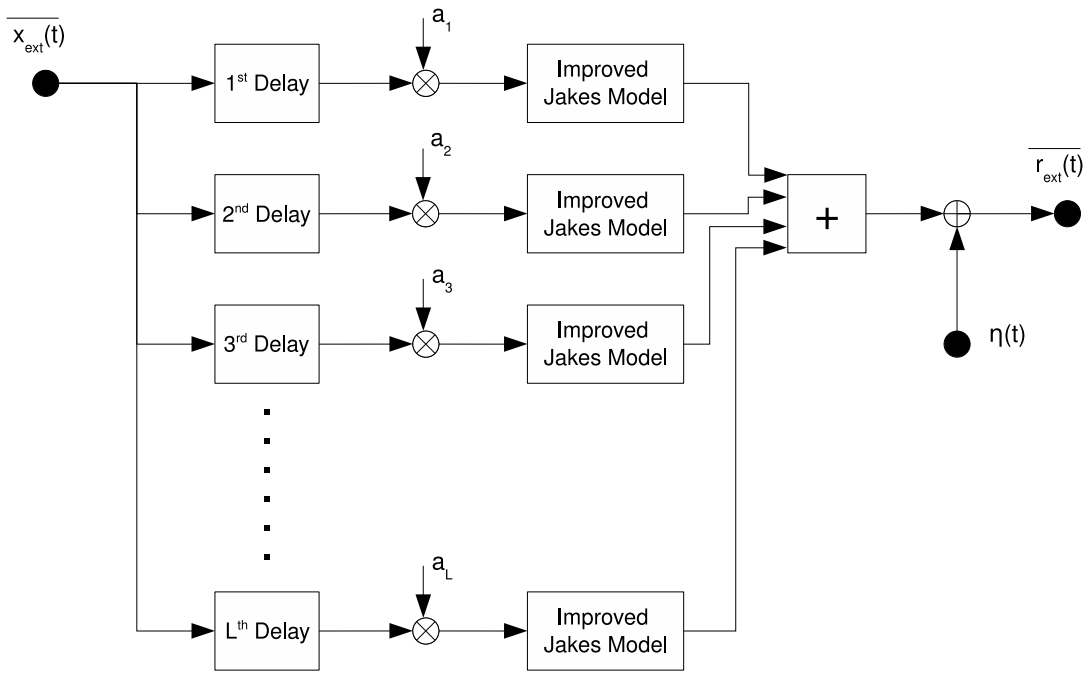

FIGURE 2.7: Simulating a mobile fading channel.

$$T_b \leq \frac{0.01}{f_D}. \tag{2.64}$$

Where T_b denotes the OFDM symbol time and f_D denotes the maximum Doppler frequency shift. The L propagation paths are combined at the receiver and corrupted by AWGN noise. The AWGN noise $\eta(t)$ is scaled accordingly using the power scaling factor k_η (see section 2.5.1). The output of the communication model after the AWGN noise is given by $\overline{r_{ext}(t)}$ and is fed to the receiver module.

2.5.4 Simulating a Mobile WiMAX System

The last section of this chapter addresses the two functional blocks, WiMAX Frame Constructor and WiMAX Frame Deconstructor, in Figure 2.2 on page 14 respectively.

The function of the WiMAX Frame Constructor is to ensure that the OFDM symbol's subcarriers are loaded with the correct control and data signals that conform to the WiMAX standard [8, 9]. There exist many different operating schemes and modes [8] in WiMAX. The more popular OFDMA was used as access scheme [32], with the FUSC chosen as the operation mode. There exist four different operating bandwidths available in mobile WiMAX and with each bandwidth there is a corresponding FFT size and they are 128, 512, 1024 and 2048 FFT

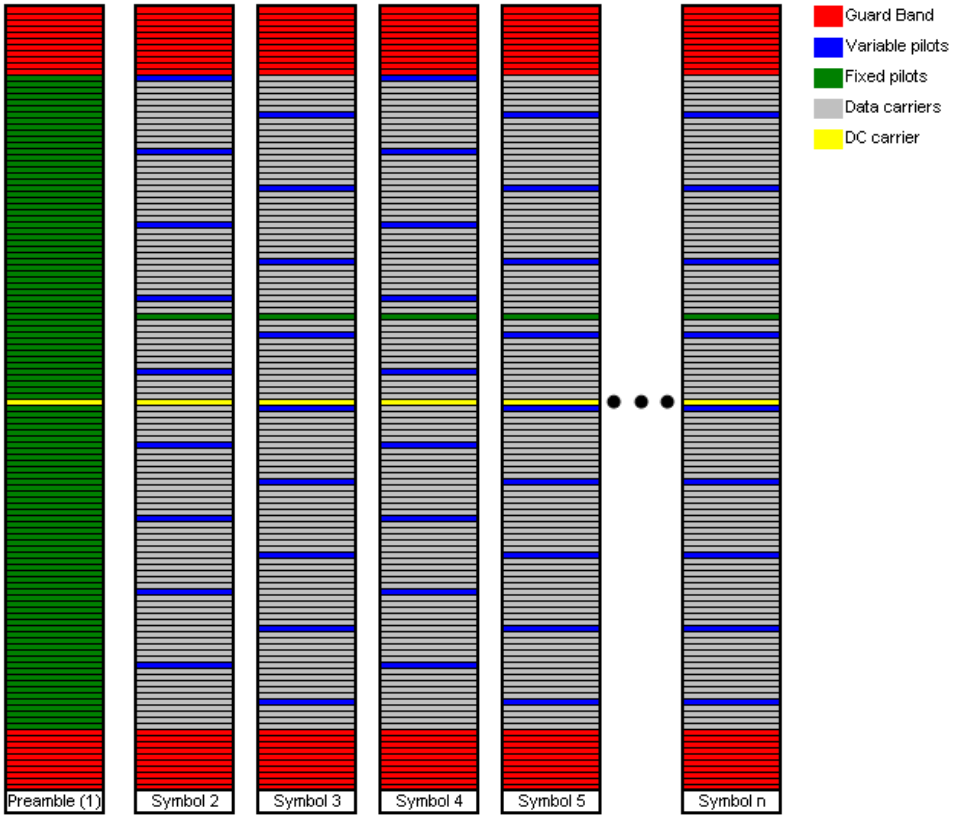

FIGURE 2.8: Frame structure for mobile WiMAX operating under FUSC mode.

size respectively with corresponding ranges of 1.25MHz to 20MHz system bandwidth. A frame structure for a 128 point FFT is shown in Figure 2.8 with all different types of subcarriers.

The frame constructor starts by filling in all the null carriers into their positions, which are the left, right and DC guardbands. The null carriers within the OFDMA symbol carries no information and the left and right guardbands are placed to reduce the adjacent carrier interference (ACI). The direct current (DC) guardband is placed to ensure that there is no DC information at the receiver, this is because most electronic devices are sensitive to a DC component [63].

The frame constructor continues by assigning a sequencial numerical value to all the unused subcarriers left in the OFDMA symbol. This is followed by placing the pilot (reference carriers) tones in the correct numerical valued subcarrier. There are two types of pilot tones in a WiMAX system, namely the constant and variable pilot tones. The constant pilot tones are always assigned to the same location, while the variable pilot tones use a predetermine vector *Variable Set#X* [8] to determine their positions as

$$\text{Pilot location} = \text{VariableSet\#X} + 6 \cdot ((\text{FUSC symbol number}) \bmod 2). \tag{2.65}$$

After assigning a location to each pilot, the pilot requires a synchronized reference source between the BS and SS, to supply pilots with pseudo-randomized data that is modulated.

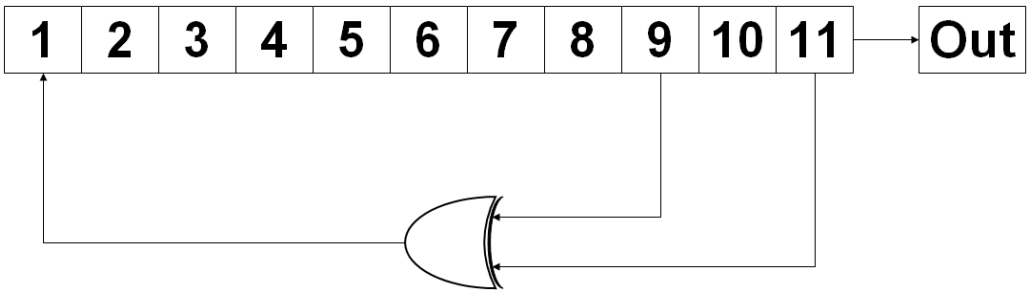

FIGURE 2.9: PRBS generator for pilot modulation.

This pseudorandom binary source (PRBS) is presented in Figure 2.9 and is initialized by loading five least significant bits (LSB) with the cell identification (CID) as indicated by the frame preamble in the first downlink zone into the five LSB bits of the register (Register 1-5). This is followed by loading register 6 and 7 with an increment (+1) sement number as indicated by the preamble in the first downlink zone. The last four registers (Register 8-11) is loaded with 1111_2 for the downlink burst. After this, the pilot amplitudes are clocked out serially for the OFDM symbol.

This PRBS will generate data for the pilot tones and is dictated by [8] to have a average boost of 2.5 dB over the average data subcarrier and is modulated with an amplified BPSK modulation scheme as

$$C_k = \frac{8}{3}\left(\frac{1}{2} - \text{Out}\right). \tag{2.66}$$

The frame constructor continues by assigning a sequencial numerical value to all the unused subcarriers left in the OFDMA symbol (after guard and pilot insertions) and will be used to insert the data carriers. Table 2.2 summarizes the subcarrier distributions for FUSC operations within mobile WiMAX.

All the data subcarriers (SC) are further subdivided into groups of subcarriers known as subchannels. In FUSC mode each subchannel has 48 subcarriers assigned to it and the number of available subchannels are also documented in Table 2.2. To allocate the subcarriers of each subchannel the positions can be computed as

$$\text{subcarrier}(k,s) = N_{subch} \cdot n_k + \left(p_s \cdot \left(n_k \bmod N_{subch}\right) + DL_{PermBase}\right) \bmod \left(N_{subch}\right). \quad (2.67)$$

where the k^{th} subcarrier, $k \in [0, N_{subcar}-1]$, of the s^{th} subchannel, $s \in [0, N_{subch}-1]$, is denoted as subcarrier(k,s). The constant n_k is equal to n_k = $(k + 13 \cdot s)$mod N_{subcar} and $p_s(j)$ is the series obtained from the basic permutation sequence [8] that was cyclically shifted to the left s times. The $DL_{PermBase}$ is a $\mathbb{N}_0$, with $DL_{PermBase} \in [0, 31]$, which is set to preamble CID in the first zone.

TABLE 2.2: Subcarrier distribution in mobile WiMAX frame

FFT size	# Left SC	# Right SC	# DC SC	# Pilot SC	# Data SC	# Subchannel
128	11	10	1	10	96	2
512	43	42	1	42	384	8
1024	87	86	1	82	768	16
2048	173	172	1	166	1536	32

The modulated symbols that are mapped to each of these subcarriers have already been discussed in section 2.4.1 and section 2.4.2. After all the subcarriers have been assigned, they are passed to the OFDM modulator for transmission. At the receiver's module the WiMAX Frame Deconstructor is used to reverse the entire process discussed in this section and supply the mapped information symbols to the correct subchannel.

2.6 CONCLUDING REMARKS

The chapter embarks on describing the realistic mobile WiMAX platform that was implemented (section 2.5.4) for the simulation study of this dissertation. In section 2.4.1.2 a formula was presented to calculate the bit probability for any baseband signal constellation that was used within the simulator. The discussion continues on mobile WiMAX using OFDMA as modulation scheme and in section 2.4.2 we give a mathematical description on the effects PAPR will exert on the transmitted symbol. To compensate for the OFDM system an extension to the AWGN scaling factor [40] is shown in section 2.5.1.

CHAPTER THREE
CONVOLUTIONAL CODES

3.1 CHAPTER OVERVIEW

Binary convolutional codes [6] have been found to have many applications in numerous communication systems [5] and is seen as a benchmark for performance analysis in most coding schemes. The chapter begins by explaining the procedures of how channel coding is applied in a systematic approach (section 3.2) to the mobile WiMAX standard [8]. The chapter continues by discussing the standardized convolutional code used with all its design parameters (section 3.3). The block interleaver proposed in the mobile WiMAX was shown in section 3.4. Section 3.5 discusses the Viterbi decoding algorithm that employs the maximum-likelihood (ML) sequence detection for the decoding of a convolutional code. The chapter concludes in section 3.5.3 with a mathematical description of the performance of the convolutional code and its decoding implementation constraints.

3.2 CHANNEL CODING - MOBILE WiMAX

In this section a brief discussion follows on how coding was applied in the mobile WiMAX. Figure 3.1 represents the encoding process at the transmission module and Figure 3.2 represents the decoding process at the receiver module. The binary source supplies the system with binary user payload data and is shuffled by use of a randomizer [8]. For the purpose of this dissertation the binary source with the randomizer is seen as a source coding block and it was assumed that perfect source coding has been used and entropy has been reached with acceptable distortion. The source encoded data $\overline{b}$ is passed to the forward error control (FEC) encoder (section 3.3) that

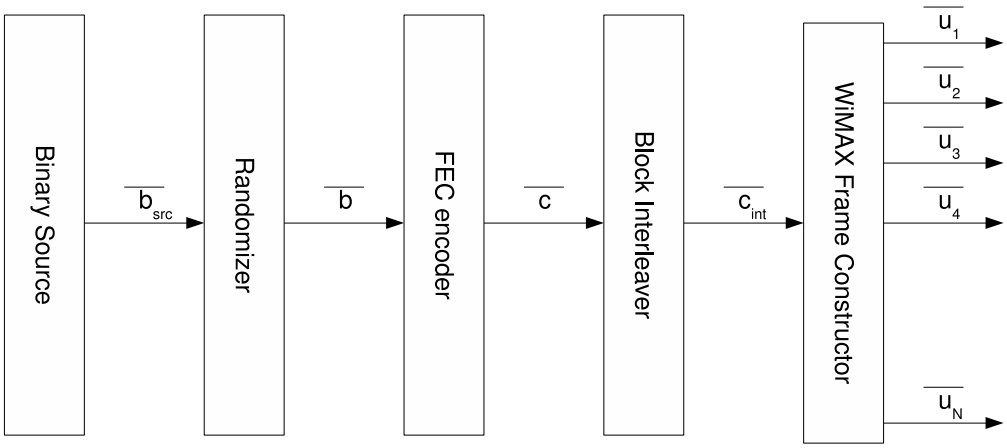

FIGURE 3.1: Channel coding process for mobile WiMAX transmitter.

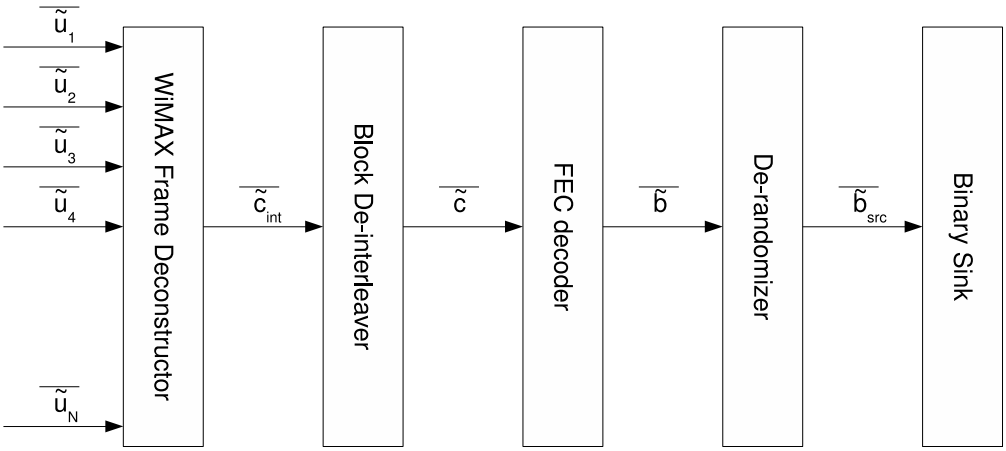

FIGURE 3.2: Channel coding process for mobile WiMAX receiver.

adds redundant bits to the information stream and this coded stream $\overline{c}$ is shuffled by the block interleaver (section 3.4). After all the operations are performed, the coded binary stream $\overline{c_{int}}$ is passed to the WiMAX frame constructor that loads all subcarriers to conform to the mobile WiMAX standard [8]. The complete process is reversed at the receiver module with the FEC decoder (section 3.5) estimating the most probable coded bit sequence sent from $\overline{\tilde{c}}$ and decoding it to the most probable information bit stream $\overline{\tilde{b}}$.

3.3 BINARY CONVOLUTIONAL CODE

Definition 3.3.1 *A code $\mathcal{C}$ of length $n_{\mathcal{C}}$ and cardinality $M_{\mathcal{C}}$ over a finite field $\mathbb{F}$ is a subset of $\mathbb{F}^{n_{\mathcal{C}}}$ with $M_{\mathcal{C}}$ elements.*

$$\mathcal{C} \triangleq \left\{\overline{c}^{[1]}, \overline{c}^{[2]}, \ldots, \overline{c}^{[M_{\mathcal{C}}]}\right\}, \overline{c}^{[i]} \in \mathbb{F}^{n_{\mathcal{C}}},\ m \in [1, M_{\mathcal{C}}]. \tag{3.1}$$

The elements of code $\mathcal{C}$ are called codewords [64].

Definition 3.3.2 *The rate R_c of a code $\mathcal{C}$ is used to define the number of information bits per transmission bits for a given channel coding scheme of length $n_{\mathcal{C}}$ and cardinality $M_{\mathcal{C}}$ over a finite field $\mathbb{F}$ and is given as $R_c \triangleq n_{\mathcal{C}}^{-1}\log_{|\mathbb{F}|}M_{\mathcal{C}}$.*

Definition 3.3.3 *The total number of shift registers within a convolutional encoder is referred to as the $memory$ of the convolutional code and is denoted by m and the number of input bits into the encoder is presented by k.*

A convolutional code is an error correcting code (ECC) that uses a finite state diagram to process memory into a serial stream of information bits.

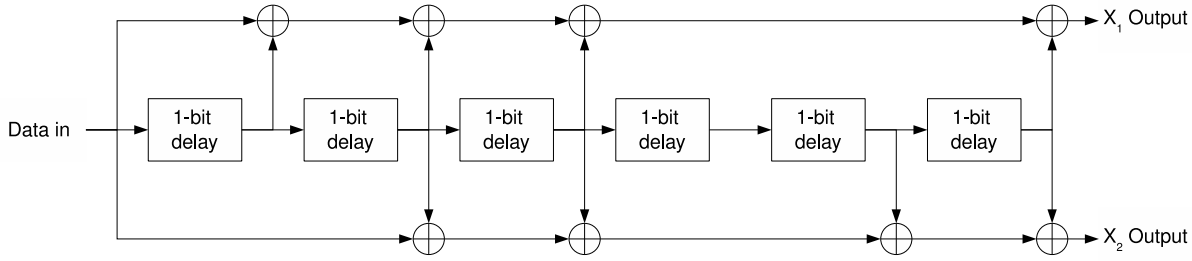

FIGURE 3.3: Convolutional encoder, $R_c = \frac{1}{2}$, $\mathcal{K} = 7$.

Figure 3.3 illustrates the design of the convolutional encoder [5] used in this dissertation.

Definition 3.3.4 *The constraint length $\mathcal{K}$, is equal to the $memory$ of the convolutional encoder incremented by 1, in short $\mathcal{K} = m + 1$.*

The constraint length $\mathcal{K}$ of a convolutional code is the fundamental design parameter and will be discussed in section 3.5.3. It is traditional to define the convolutional encoder by expressing the generator taps in octal form. The convolutional encoder presented in Figure 3.3 is of interest, as it is proposed in [8, 9] as a mandatory channel coding scheme and its generator taps are given as

$$g = (171; 133)_{oct}, \tag{3.2}$$

or as finite impulse response (FIR) system [5] given as

$$\overline{g}_1 = 1 + D + D^2 + D^3 + D^6 \quad and \quad \overline{g}_2 = 1 + D^2 + D^3 + D^5 + D^6. \tag{3.3}$$

Since the output of the encoder is dependent on the input bit and the current stored memory in the registers, the $memory$-m rate-R_c convolutional encoder can then be presented as a state diagram [65]. The state diagram is a graph of all the state nodes of the encoder and all possible transitions from a current state (current register contents) to another state (new register contents). There are 2^m states in a convolutional encoder and only 2^k branches entering and 2^k branches leaving each state of the diagram, with k denoting the number of input bits into the encoder. The state diagram for the proposed convolutional code is not illustrated in this dissertation, as there are 64 states with 4 branches eminating at each state node. The state diagram information is given in table format in appendix B and can be extended to a state diagram.

After the state diagram has been obtained from the structure of the convolutional encoder, it can be further developed to a time transition state diagram [5] known as a trellis diagram [5, 30, 40]. Zero tailing bits are appended to the information bits to ensure that the trellis always terminates in the all-zero state, this simplifies the decoding process and only requires m zero bits to flush the convolutional encoder.

3.4 TIME DIVERSITY - INTERLEAVER

The main idea of an interleaver [66, 67] is to obtain time diversity in a digital communications system [1]. Time diversity in a communication system is the transmission of information symbols at time spacings that are longer than the coherence time T_c of the communication channel. This is exploited by taking bursty error symbols and de-interleaving it over an entire frame after which a channel coding algorithm is used to control the number of errors within the frame. Time diversity can be mathematically expressed by shuffling the data stream according to a certain permutation vector. It must be remembered not to add any redundancy bits to the information stream. The mapping of a m_1 x m_2 block of input bits according to a permutation is

$$\overline{c} = (c_0;\ c_1;\ \ldots\ ;\ c_{m_1 m_2 - 1}), \tag{3.4}$$

with $\overline{c}$ denoting the input block and the interleaved block as

$$\overline{c_{int}} = (c_{int(0)};\ c_{int(1)};\ \ldots\ ;\ c_{int(m_1 m_2 - 1)}). \tag{3.5}$$

The proposed interleaver for mobile WiMAX [8] in this dissertation is the block interleaver. This block interleaver is defined by a two step permutation. The first permutation ensures that adjacent coded bits are mapped to non-adjacent subcarriers and the second permutation ensures that the adjacent code bits are mapped alternatively onto different significant bits on the constellation map [9]. The first permutation of the interleaver is defined as

$$m_k = \frac{N_{cbps}}{d} \cdot (k \bmod d) + \left\lfloor \frac{k}{d} \right\rfloor. \tag{3.6}$$

Where the number of input bits to the block interleaver is denoted by N_{cbps}. Integer k, $k \in [0, N_{cbps}\text{-}1]$, is the index of the code bits before the first permutation and integer m_k, $m_k \in [0, N_{cbps}\text{-}1]$, is the index of the code bits after the first permutation. The integer d is equal to $16n_{sc}$, with n_{sc} denoting the number of allocated slots per FEC block. The second permutation of the interleaver is defined as

$$j_k = s\left\lfloor \frac{m_k}{s} \right\rfloor + \left(\left(m_k + N_{cbps} - \left\lfloor \frac{d \cdot m_k}{N_{cbps}} \right\rfloor \right) \bmod s \right). \tag{3.7}$$

Where $s = N_{cpc}/2$, with N_{cpc} equal to the coded bits per subcarrier, i.e., 2,4 or 6 for 4-QAM, 16-QAM or 64-QAM, respectively. Integer m_k, $m_k \in [0, N_{cbps} - 1]$, is the index of the code bits before the second permutation, and integer j_k, $j_k \in [0, N_{cbps} - 1]$, is the index of the code bits after the second permutation. After the interleaving is done on the coded bits stream the data is transfered to the modulation scheme in use. To reverse the process at the receiver module just prior to the passing of the coded bits to the channel decoder, the first permutation of the de-interleaver is equal to

$$m_j = s \cdot \left\lfloor \frac{j}{s} \right\rfloor + \left(\left(j + \left\lfloor \frac{d \cdot j}{N_{cbps}} \right\rfloor \right) \bmod s \right). \tag{3.8}$$

Where integer j, $j \in [0, N_{cbps} - 1]$, is the index of the coded bit before the first permutation and integer m_j, $m_j \in [0, N_{cbps} - 1]$, is the index of the coded bit after the first permutation. The second permutation of the de-interleaver is given as

$$k_j = d \cdot m_j - (N_{cbps} - 1) \cdot \left\lfloor \frac{d \cdot m_j}{N_{cbps}} \right\rfloor. \tag{3.9}$$

With integer m_j, $m_j \in [0, N_{cbps} - 1]$, is the index of the code bit before the second permutation and integer k_j, $k_j \in [0, N_{cbps} - 1]$, is the index of the code bit after the second permutation. This block interleaver was used in all simulations in this dissertation as it is mandatory to bit interleave all coded bits in a mobile WiMAX communication system.

3.5 DECODING METHOD - VITERBI ALGORITHM

The function of the decoding algorithm is to estimate the correct stream of uncoded bits that will result in the minimum number of errors. There is of course a one-to-one mapping between the coded bits and the information bits [1]. In the design of a convolutional encoder, a unique trellis diagram can be extracted, as discussed in section 3.3. The decoding of a convolutional code is used to estimate the most likely path through the trellis given a vector of received coded bits. The most popular decoding algorithm for the convolutional codes is the Viterbi algorithm [7, 68].

Definition 3.5.1 *Hamming distance is the number of bit differences there are between two binary sequences of the same length [65].*

Definition 3.5.2 *Hamming weight is the Hamming distance between a given binary sequence and the all-zero sequence of the same length.*

Definition 3.5.3 *The free distance d_{free} of a convolutional code is the smallest Hamming distance between any two distinct code sequences.*

Definition 3.5.4 *A non-systematic code is a code $\mathcal{C}$ that has no information bits within the encoder's output bits stream (only parity bits), while a systematic code has information bits included in the coded bits of the encoder's output stream [5].*

Definition 3.5.5 *Coding gain is defined as the difference in SNR between a coded and uncoded system or two coded systems with the same rate.*

The main decoding rule of the Viterbi algorithm is to solve

$$\overline{d}^{ML}\big(\overline{\tilde{c}}\big) \triangleq \operatorname{argmax}_{\overline{c}\in\mathcal{C}}\, p_{\overline{\tilde{C}}\,|\,\overline{C}}\big(\overline{\tilde{c}}\,|\,\overline{c}\big), \tag{3.10}$$

where $\overline{c}$ is the transmitted codeword and $\overline{\tilde{c}}$ is the received codeword. The decoded codeword of the ML estimator is presented by $\overline{d}^{ML}\big(\overline{\tilde{c}}\big)$. The probability is maximized by obtaining the codeword that yields a minimum distance to the received codeword as

$$\overline{d}^{ML}\big(\overline{\tilde{c}}\big) \triangleq \operatorname{argmin}_{\overline{c}\in\mathcal{C}}\, D\big(\overline{\tilde{c}},\overline{c}\big), \tag{3.11}$$

where $D(\,)$ presents a function for calculating the distance between two binary sequences, but this will be discussed in more detail in section 3.5.1 and 3.5.2. There are 2^{Mc} codewords that

need to be tested for each decoding step and proves to be a daunting task even for the small values of $M_{\mathcal{C}}$. The Viterbi algorithm utilizes the trellis to decode the received codeword, but the advantage of the Viterbi algorithm is that it exploits the property in the trellis that when two contending paths enter a given node that only the strongest path is considered. This advantage significantly decreases decoding complexity in computations and for this reason the Viterbi algorithm is the preferred decoding algorithm for a convolutional code.

The Viterbi algorithm starts by subdividing the codeword of length $n_{\mathcal{C}}$ into $k_{\mathcal{C}}$ equal size bit sequences. The length of these equally sized bit sequences is equal to the number of output bits at the encoder. Let each of the sequences be presented by $r_{branch}(i)$, with $i \in [0, k_{\mathcal{C}} - 1]$. By mapping $r_{branch}(i)$ sequential to each time transition in the trellis the Viterbi algorithm can compute all possible branch metrics to obtain the shortest path distance. Soft decision and hard decision detection of branch metrics will be explained in the following section.

3.5.1 Hard Decision - Viterbi Algorithm

The Viterbi algorithm uses the branch weight to calculate the distance between the received code sequence and a particular branch, in an effect to compute the cumulative path metric for every surviving path. The path with the lowest metric at the end of the decoding process, as shown in $Eq.$ (3.11), is accepted as the most correct path. The received information is obtained by reading the information bits in reverse from the trellis path. The branch metric for hard decision decoding is computed as

$$d_{branch}\big(\, r_{branch}(i)\,,\, BM_{q,w}^{(i)}\big) = \sqrt{D_{hamming}\big(\, r_{branch}(i)\,,\, BM_{q,w}^{(i)}\big)}\,, \quad \forall\, q, w \in [0, 2^m{-}1], \tag{3.12}$$

with $D_{hamming}(\,)$ denoting a function to calculate the Hamming distance (Def. *3.5.1*) between two sequences of length $k_{\mathcal{C}}$. $BM_{q,w}^{(i)}$ denotes the output of the encoder given a state transition from state q to state w at time instance i. It should be noted that if there exists no state transition between state q and w at time instance i, that the Hamming distance is equal to ∞. As a result of only the surviving paths being stored, the cumulative path metric is calculated as

$$d_{cum}\big(\,\overline{\overline{c}}\,,\, R_{branch}\big) = \sum_{i=0}^{k_{\mathcal{C}}-1} d_{branch}\big(\, r_{branch}(i)\,,\, BM_{q,w}^{(i)}\big), \tag{3.13}$$

where R_{branch} is the concatenated branches of $r_{branch}(i)$ for the surviving path. The procedures

for decoding the convolutional code using the Viterbi algorithm for an arbitrary received code sequence is given as summary in the following steps: (1) Set all starting nodes path metrics equal to ∞ in the trellis except the all-zero state. (2) Draw the trellis in memory to the size of your received code sequence. (3) Start at the first node in all-zero state with i=0. (4) Find the branch metric in all subsequence branches to all nodes at time instance i=0. (5) Save the smallest metric into all nodes at destination states w and add the cumulative metric at all the nodes. (6) Discard all other branches into nodes at all states $w \in [0, 2^m-1]$. (7) Repeat the three steps before and increasing i to move through the complete trellis. (8) Discard all paths that dont terminate in the all-zero state. (9) Trace back the path with lowest cumulative metric and save all corresponding input bits. (10) Output bits from decoder to system.

3.5.2 Soft Decision - Viterbi Algorithm

The advantage of soft decision decoding (SDD) is the extra information that is preserved for the decoding process. This excess of information can be measured from the cutoff rate [30] used at the receiver. If hard decision decoding (HDD) is used with a binary signal and two-quantization levels, the cutoff rate R_2 [30] is given as

$$R_2 = 1 - \log_2\left(1 + \sqrt{4\mathcal{Q}\left(\sqrt{\frac{2R_cE_b}{N_0}}\right)\left(1 - \mathcal{Q}\left(\sqrt{\frac{2R_cE_b}{N_0}}\right)\right)}\right), \tag{3.14}$$

where $\mathcal{Q}(\,)$ is the *$\mathcal{Q}$-function* [30] that is expressed as

$$\mathcal{Q}(x) = \frac{1}{\sqrt{2\pi}}\int_x^\infty \exp\left(\frac{-t^2}{2}\right)dt. \tag{3.15}$$

The cutoff rate R_Q [30] for soft decision detection is given below with $Q \to \infty$ as

$$R_Q = \max_{\{p(s_j(f))\}}\left(-\log_2\sum_{i=0}^{Q-1}\left(\sum_{j=0}^{q-1}p(s_j(f))\sqrt{\int_{r_i}\left(\frac{1}{\sqrt{2\pi}\sigma_{\eta(t)}}\exp\left(-\frac{D(\tilde{s}_j(f), s_j(f))^2}{2\sigma^2_{\eta(t)}}\right)\right)d\tilde{s}_j(f)}\right)^2\right), \tag{3.16}$$

where $D()$ denotes the function to calculate the Euclidean distance and r_i corresponds to the region of the transition probability of quantization level i. The probability of transmitting a particular symbol is given by $p(s_j(f))$, $j \in [0, q-1]$ and q is the total number of symbols. The total number of quantization levels are presented by Q and $\sigma^2_{\eta(t)}$ is the noise variance of the AWGN process.

By comparing $Eq.$ (3.14) and $Eq.$ (3.16) [30] for any given code rate R_c, there will always be a 2dB gain in quantization at the receiver module when employing soft decision decoding for an AWGN channel. Another alternative is to only quantize the data to $Q = 8$ or more, then the loss of information is only 0.2dB from $Q = \infty$. It is noted that ∞-quantization levels are used in the Viterbi algorithm, the only change from hard decision detection is to update the branch metric $Eq.$ (3.12) to

$$d_{branch}\big(\, r_{branch}(i)\,,\, BM_{q,w}^{(i)}\big) = \sqrt{D\big(\, r_{branch}(i)\,,\, BM_{q,w}^{(i)}\big)}\,, \quad \forall\, q, w \in [0, 2^m{-}1]. \tag{3.17}$$

Where $r_{branch}(i)$ is now quantized by Q-levels and $D()$ is the Euclidean distance between the two quantized sequences.

3.5.3 Performance Analysis of Convolutional Codes

The free distance and the bit error rate performance can be derived from the state diagram of the convolutional code. A upper bound [30, 69] for the minimum free distance of a rate $\frac{1}{n_{\mathcal{C}}}$ convolutional code is given as

$$d_{free} \leq \min_{l \geq 1} \left\lfloor \frac{2^{l-1}}{2^l{-}1}(\mathcal{K} + l - 1)n_{\mathcal{C}} \right\rfloor. \tag{3.18}$$

The free distance d_{free} can also be directly derived from the transfer function [30, 39]. The advantage of having a large minimum free distance d_{free} code is that it lowers the decoded BER of the convolutional code. The disadvantage however is when a decoding process fails, the code induces more bit errors within the received coded sequence. For a more direct relation to performance enhancement [70] of the minimum free distance is the coding gain (CG) given by

$$CG[\,\mathrm{dB}\,] = 10\log_{10}(R_c\, d_{free}). \tag{3.19}$$

This is observed at high E_b/N_0 values as an asymptotic coding gain. The best performance comparison is found by obtaining a union bound for the bit error probability p_{CC} of the convolutional code. The following union bounds for a convolutional code in an AWGN channel is given as [5, 71]

$$p_{CC} < \mathcal{Q}\left(\sqrt{2R_c\, d_{free}\, \frac{E_b}{N_0}}\right) \exp\left(2R_c\, d_{free} \frac{E_b}{N_0}\right) \frac{dT(D, N, J)}{dN}\bigg|_{D=DO,\, N=1,\, J=1}, \tag{3.20}$$

with

$$DO = \begin{cases} \sqrt{4\mathcal{Q}(\sqrt{2R_cE_b/N_0})(1-\mathcal{Q}(\sqrt{2R_cE_b/N_0}))} & \text{Hard decision detection,} \\ \exp(-R_cE_b/N_0) & \text{Soft decision detection,} \end{cases} \tag{3.21}$$

where $T(D, N, J)$ is the transfer function [30, 39] with the Hamming weight of the input stream presented by the power of N. A connection between two states is presented by the power of J and the Hamming weight of the output stream is presented by the power of D. The union bound of the bit error probability for a convolutional code (expressed in $Eq.$ (3.20)) is a function of the minimum free distance d_{free}. The following relation is always present as

$$p_{CC} \propto \mathcal{K}. \tag{3.22}$$

Good BER performance has been acquired [72] for a convolutional code operating with a more complex QAM modulation scheme in an OFDM symbol. The relation in $Eq.$ (3.22) is a drawback in the improvement of the BER performance of a convolutional code. The reason behind it is that by increasing the constraint length $\mathcal{K}$, the memory m of the coding scheme is increased, which results in a massive increase of complexity in the system decoder. In summary, an increase in the constraint length $\mathcal{K}$ of 1, results in the total of number of states being doubled. This is because the number of states within the state diagram is equal to $2^{\mathcal{K}-1}$. This increase in complexity at the receiver module, makes it unfeasible for a practical implementation of the corresponding decoder. The next drawback is that there exists a maximum number of input bits k_{max} that saturates the memory property of the convolutional encoder and yields no more coding gain for large input blocks. This maximum number of input bits k_{max} is equal to

$$k_{max} = 5\,\mathcal{K} + 1. \tag{3.23}$$

Thus to effectively encode larger packets of binary data, the constraint length $\mathcal{K}$ must be increased. As discussed before, this is a practical limitation in all systems using a convolutional code.

3.6 CONCLUDING REMARKS

This chapter discussed the incorporation of the channel coding scheme into a mobile WiMAX platform. Thereafter the mandatory convolutional code [8] was discussed with particular

emphasis on the design parameters and constraints. It was observed from the constraints that the decoding complexity of the convolutional code will be too high to fully utilize a subchannel in an OFDM symbol (section 3.5.3).

CHAPTER FOUR

LOW-DENSITY PARITY CHECK CODES

4.1 CHAPTER OVERVIEW

Mackay [19] rediscovered the LDPC code in 1999 that was proposed by R. Gallager [16]. The LDPC code was optimized for a BEC channel [16] and in 2001, R.L. Urbanke and T. Richardson proposed a method for optimizing a LDPC code for a continuous channel [27, 28]. After the design and development of the LDPC code, it matured [18] and found an application as a new optional coding scheme to be used in the mobile WiMAX standard [8].

This chapter's focus is on explaining all the concepts necessary to understand the design of a LDPC code. The chapter starts by explaining the decoding process and properties of a linear block code and then translates this to a factor graph. A LDPC code is a very sparse graph code and will often be referred to as a graph code in this chapter. The chapter continues with a discussion on statistical notation[1] used to describe a graph code and is followed by explaining the notation in a LDPC code design and all necessary simplification required. *Density evolution* [16] is the method of optimizing a graph code (section 4.8) and can be illustrated as a visual process by means of an extrinsic information transfer (EXIT) chart [73]. The chapter concludes with showing how a LDPC code can be optimized for an OFDM modulation system with peak clipping conditions at the transmitter.

[1] See Appendix C for information on notation.

4.2 LINEAR BLOCK CODES

A linear block code is a code $\mathcal{C}(n_\mathcal{C}, k_\mathcal{C})$ that is completely defined by $M_\mathcal{C} = 2^{k_\mathcal{C}}$ codewords. Each codeword consists of $n_\mathcal{C}$ symbols of set $\mathbb{F}_2$ and all addition operations are done with a component-wise modulo-2 addition function [39]. A linear block code is a $k_\mathcal{C}$-dimensional subspace $\mathbb{F}$ of a $n_\mathcal{C}$-dimensional space $\mathbb{F}^{n_\mathcal{C}}$ [74].

Definition 4.2.1 *A block code $\mathcal{C}(n_\mathcal{C}, k_\mathcal{C})$ is linear if all combinations of two codewords results in a codeword.*

Definition 4.2.2 *The minimum distance $d_{min}(\mathcal{C})$ of code $\mathcal{C}$ is equal to the minimum Hamming distance between any two codewords [5, 39] and is expressed as*

$$d_{min}(\mathcal{C}) = \min\{D(\overline{c_q}, \overline{c_w}) : \overline{c_q}, \overline{c_w} \in \mathcal{C}, q \neq w\}. \tag{4.1}$$

Where $D(\,)$ is the function that calculates the Hamming distance between two binary sequences.

A design parameter of a linear block codes is to seperate the distance between all the $2^{k_\mathcal{C}}$ codewords in the space $\mathbb{F}^{n_\mathcal{C}}$ to a maximum. This $\mathbb{F}^{n_\mathcal{C}}$ space where all codewords are allocated is known as the *Hamming space*. A Hamming sphere $S_t(\overline{c_q})$ of radius t and centered around codeword $\overline{c_q}$ is the set of vectors at a Hamming distance less than or equal to t from codeword $\overline{c_q}$.

$$S_t(\overline{c_q}) = \{\overline{c_w} \in \mathbb{F}^{n_\mathcal{C}} | D(\overline{c_q}, \overline{c_w}) \leq t\}. \tag{4.2}$$

The idea of the Hamming sphere is that when any codeword $\overline{c_w}$ is received within the radius centered at $\overline{c_q}$ in the space of $\mathbb{F}^{n_\mathcal{C}}$, it will be mapped to the codeword $\overline{c_q}$. This concept illustrates the error correcting capabilities t of a linear code $\mathcal{C}(n_\mathcal{C}, k_\mathcal{C})$. To improve the average expected error correcting capability t it is good practice to strive to enlarge all the Hamming spheres in the space $\mathbb{F}^{n_\mathcal{C}}$ (seperating codewords as far as possible in the Hamming space). The larger the Hamming spheres, the more error must be induced to the codeword before the codeword is relocated to a new Hamming sphere and is mapped to an incorrect codeword. The error correcting capabilities can also be expressed in terms of the minimum distance d_{min} [5, 39] as

$$t = \left\lfloor \frac{d_{min} - 1}{2} \right\rfloor. \tag{4.3}$$

To compute the minimum distance d_{min} of the linear block code $\mathcal{C}(n_{\mathcal{C}}, k_{\mathcal{C}})$ all the codeword needs to be weighted against the all-zero codeword and is expressed as

$$d_{min} = \min_{2^{k_{\mathcal{C}}}-1} \{D(\overline{c_q}, \overline{0}) : \overline{c_q} \in \mathcal{C}, \overline{c_q} \neq \overline{0}\}. \tag{4.4}$$

In this dissertation it was not feasible to compute the minimum distance, as there were $2^{k_{\mathcal{C}}} - 1$ Hamming weights to be calculated and that $k_{\mathcal{C}} \geq 288$. This leads to more than $4.9732\text{x}10^{86}$ Hamming weight computations for a single LDPC code. The $k_{\mathcal{C}}$-dimensional subspace $\mathbb{F}$ is mapped to the $n_{\mathcal{C}}$-dimensional by defining a generator matrix $\mathcal{G}$ of size $k_{\mathcal{C}}$ x $n_{\mathcal{C}}$ to encode a message stream $\overline{b}$ of size 1 x $k_{\mathcal{C}}$ as

$$\overline{c} = \overline{b} \cdot \mathcal{G}. \tag{4.5}$$

The generator matrix $\mathcal{G}$ must be full rank of $k_{\mathcal{C}}$ to ensure that the linear block code $\mathcal{C}(n_{\mathcal{C}}, k_{\mathcal{C}})$ is a proper code [64], as an *all-zero column conveys zero information - no pun intended*. For every linear code $\mathcal{C}(n_{\mathcal{C}}, k_{\mathcal{C}})$ there exist a $n_{\mathcal{C}}$-$k_{\mathcal{C}}$ dual space $\mathcal{C}^{\top}$ generated by the rows of the matrix $\mathcal{H}$, where $\mathcal{H}$ is referred to as the parity check matrix and is a full rank ($n_{\mathcal{C}}$ -$k_{\mathcal{C}}$) x $n_{\mathcal{C}}$ matrix. The dual code is defined as

$$\mathcal{G} \cdot \mathcal{H}^{\top} = \overline{0}. \tag{4.6}$$

This property is used at the decoder to verify codewords and is given as

$$\overline{c} \cdot \mathcal{H}^{\top} = \overline{0}. \tag{4.7}$$

The complexity of encoding the information stream $\overline{b}$ with the generator matrix can be accomplished with $O(n^2)$ operations [75] and the linear code $\mathcal{C}$ has a description size of $\min\{R_c \cdot n_{\mathcal{C}}^2, (1 - R_c) \cdot n_{\mathcal{C}}^2\}$ bits at most [64]. In the decoding of the received codeword to their correct codeword in the Hamming space, it is conventional in linear codes to first check if an incorrect codeword has been received at the decoder. This is done by verifying the dual code property in $Eq.$ (4.7) and the result is termed as the syndrome $\overline{s_{\mathcal{C}}}$ of the codeword $\overline{\tilde{c}}$. This dual code is computed as

$$\overline{s_{\mathcal{C}}} = \overline{\tilde{c}} \cdot \mathcal{H}^{\top}. \tag{4.8}$$

If an error vector $\overline{\varepsilon}$ is induced onto the codeword as $\overline{\tilde{c}} = \overline{c} + \overline{\varepsilon}$, then $Eq.$ (4.7) will not yield an all-zero vector and is expanded as

$$\overline{s_{\mathcal{C}}} = (\overline{c} + \overline{\varepsilon}) \cdot \mathcal{H}^{\top} \pmod 2. \tag{4.9}$$

With linear addition, the syndrome can be divided as

$$\overline{s_{\mathcal{C}}} = \overline{c} \cdot \mathcal{H}^{\top} + \overline{\varepsilon} \cdot \mathcal{H}^{\top} \pmod 2. \tag{4.10}$$

By substituting $Eq.$ (4.7) into $Eq.$ (4.10) yields a syndrome $\overline{s_{\mathcal{C}}}$ of

$$\overline{s_{\mathcal{C}}} = \overline{\varepsilon} \cdot \mathcal{H}^{\top}. \tag{4.11}$$

The next section will cover on how to construct a good specific linear code and show how the decoder attempts to eliminate the error vector in a given received codeword.

4.3 SPARSE GRAPH CODES

A linear block code known as the LDPC code was first invented by Robert Gallager in 1963 [16]. The main characteristics of a LDPC code is that the parity-check matrix $\mathcal{H}$ is very sparse (usually a density of less than 1% in the matrix). This has the effect of lowering the number of dependencies (received coded bits $\overline{c}^{[q]}, q \in [0, n_{\mathcal{C}} - 1]$) for each element in the syndrome vector $\overline{s_{\mathcal{C}}}^{[w]}, w \in [0, (n_{\mathcal{C}}$ -$k_{\mathcal{C}}$-1)]. This sparse matrix enables the linear block code to exhibit exceptional BER performance using a message-passing decoder (discussed in section 4.5). These dependencies of each syndrome can be illustrated in a bipartite graph (Tanner graph) and is discussed in section 4.4.

4.4 FACTOR GRAPHS

In iterative decoding of a LDPC code, the decoding process can be understood in terms of a graphical model of a code $\mathcal{C}$ [76, 77]. A factor graph provides a structure to take advantage of the distributive law to reduce complexity in the decoding process significantly. The Viterbi decoding algorithm can be graphically presented by a trellis diagram [40] which is a special case of a factor graph and offers a reduction in complexity for a convolutional code. The approach with a factor graph is to factorize the function that need to be solved and identify groups of subfunctions for global functions and execute them once off. A factor graph for a LDPC code can be generalized to a Tanner graph [78] and is an efficient method in expressing the operations

of the sum of product algorithm. Belief propagation [24] which operates by message-passing is an instance of the sum-product algorithm and the operation of the algorithm will be discussed in section 4.5.

Definition 4.4.1 *A factor graph is a bipartite graph that expresses the structure of the factorization [64, 77] as*

$$g(\tilde{c}_1, \tilde{c}_2, \ldots, \tilde{c}_{n_\mathcal{C}}) = \prod_{j \in J} f_j(\tilde{C}_j). \tag{4.12}$$

Where $g(\tilde{c}_1, \tilde{c}_2, \ldots, \tilde{c}_{n_\mathcal{C}})$ factors into several local functions. A factor graph has a variable node for each variable $\tilde{c}_i$ with $i \in [1, n_\mathcal{C}]$ and a factor node for each local function f_j. An edge connecting a variable node with a factor node exists only if an argument is made between them.

A factor node is known as a check node in coding theory field and will be used in this dissertation.

4.4.1 Tanner Graphs

A Tanner graph is an example of a factor graph [77] and is tailor made to fit the decoding process of a LDPC code. With a linear code $\mathcal{C}(n_\mathcal{C}, k_\mathcal{C})$ the parity-check matrix $\mathcal{H}$ was used to describe the bipartite graph of the decoder. The Tanner graph of code $\mathcal{C}(n_\mathcal{C}, k_\mathcal{C})$ has $n_\mathcal{C}$ variable nodes that corresponds to each element of the codeword and $m_\mathcal{C}$=($n_\mathcal{C}$ -$k_\mathcal{C}$) check nodes that corresponds to each of the parity-check constraints (syndromes) of $\mathcal{H}$. An edge in the Tanner graph exist only if the corresponding matrix value $\mathcal{H}_{ij}$ has a 1, where i and j denotes the column and row of the parity-check matrix respectively.

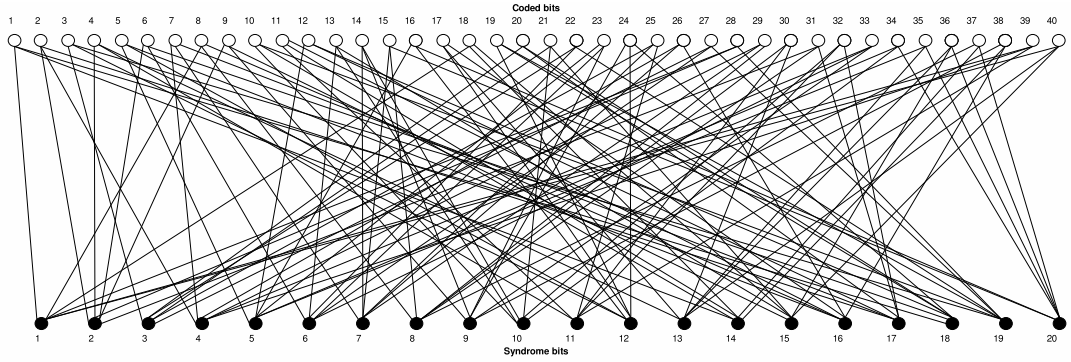

FIGURE 4.1: Example Tanner graph of LDPC (40,20) code.

As seen in Figure 4.1 even a short length LDPC code that is sparse is graphically concentrated. The density of edges in the graph for a LDPC code grows linearly with the codeword length $n_{\mathcal{C}}$, but is intense since $n_{\mathcal{C}} \geq 576$ in this dissertation. The next attribute that is addressed is the degree of connection that exists at each variable and check node. The degree is equal to the number of edges that emanate from a node, which can either be a check or variable node.

Definition 4.4.2 *When all the check nodes have the same degree of edges and all the variable nodes have the same degree of edges, then it is a regular graph code.*

Definition 4.4.3 *A LDPC code with all check nodes of degree r and variable nodes of degree l is known as a regular LDPC code.*

Definition 4.4.4 *A LDPC code with a degree distribution for all degrees of check nodes and a seperate degree distribution for all degrees of variable nodes, is known as a irregular LDPC code.*

A Tanner graph describes an ensemble of codes given a certain connection between nodes [79] and is a statistical approach [16, 64, 79] to defining the ensemble. Assuming that the graph has Λ_i variable nodes of degree i and P_j check nodes of degree j the following equalities hold in the Tanner graph as

$$\Lambda(x) = \sum_{i=1}^{\mathsf{l}_{\max}} \Lambda_i \, x^i, \tag{4.13}$$

and

$$P(x) = \sum_{j=1}^{\mathsf{r}_{\max}} P_j \, x^j. \tag{4.14}$$

Where $\Lambda(x)$ and $P(x)$ denotes the variable and check node degree distributions of the graph code respectively. This notation presented in $Eq.$ (4.13) - $Eq.$ (4.14) must satisfy the following relationships for the graph code as

$$\sum_{i=1}^{\mathtt{l}_{\max}} \Lambda_i = n_{\mathcal{C}}, \tag{4.15}$$

$$\sum_{j=1}^{\mathtt{r}_{\max}} P_j = n_{\mathcal{C}}(1 - R_c), \tag{4.16}$$

$$\Lambda(1) = n_{\mathcal{C}}, \tag{4.17}$$

$$P(1) = n_{\mathcal{C}}(1 - R_c), \tag{4.18}$$

$$P'(1) = \Lambda'(1). \tag{4.19}$$

Definition 4.4.5 *A new code rate R_c is defined for the sparse code $\mathcal{C}$ and is known as the design rate [64] given as*

$$R_c(\Lambda, P) = 1 - \frac{P(1)}{\Lambda(1)}. \tag{4.20}$$

This new design rate and code rate have a difference [64] given by

$$P(R_c - R_c(\Lambda, P) \geq \varrho) \leq \exp(-0.34657\, n_{\mathcal{C}}\, \varrho). \tag{4.21}$$

By choosing $n_{\mathcal{C}}$ substantial large enough the difference between the design rate and code rate is negligible and are seen as the same parameter.

The degree distributions can be normalized as

$$L(x) = \frac{\Lambda(x)}{\Lambda(1)}, \tag{4.22}$$

$$R(x) = \frac{P(x)}{P(1)}. \tag{4.23}$$

With the normalized variable node degree distribution denoted by $L(x)$ and the normalized check node degree distribution denoted by $R(x)$ for a graph code. A variable nodes with degree 1 tends not to propagate messages efficiently and exerts early error floors in all graph designs [64]. Due to this, only variable nodes with degree > 1 were evaluated. The asymptotic analysis of a graph code is easier from a edge perspective rather than a node perspective as presented in $Eq.$ (4.13) - (4.14). The edge perspective for a graph code is given as

$$\lambda(x) = \sum_{i=1}^{\mathtt{l}_{\max}} \lambda_i\, x^{i-1} = \frac{\Lambda'(x)}{\Lambda'(1)} = \frac{L'(x)}{L'(1)}, \tag{4.24}$$

and

$$\rho(x) = \sum_{j=1}^{\mathrm{r}_{\max}} \rho_j \, x^{j-1} = \frac{P'(x)}{P'(1)} = \frac{R'(x)}{R'(1)}. \tag{4.25}$$

Where $\lambda(x)$ and $\rho(x)$ denotes the variable and check edge degree distributions of the graph code respectively. All degree distributions are polynomials with non-negative expansions around zero. The graph code has λ_i fraction of edges that connect to a variable node with degree i and ρ_j fraction of edges that connect to a check node with degree j. The following relationships hold for the edge perspective [64] as

$$\frac{\Lambda(x)}{n} = L(x) = \frac{\int_0^x \lambda(z)dz}{\int_0^1 \lambda(z)dz}, \tag{4.26}$$

$$\frac{P(x)}{n(1-R_c)} = R(x) = \frac{\int_0^x \rho(z)dz}{\int_0^1 \rho(z)dz}. \tag{4.27}$$

The design code rate from a edge perspective is given by

$$R_c(\lambda, \rho) = 1 - \frac{\int_0^1 \rho(x)dx}{\int_0^1 \lambda(x)dx}. \tag{4.28}$$

4.5 BELIEF PROPAGATION

An ensemble of codes with a given characteristic can be evaluated by means of a Tanner graph [80], which simplifies the analytical investigation into the search for good codes [19]. There are many different message passing decoders that operate on a factor graph, but the coding scheme of interest is the LDPC which is now optional in the mobile WiMAX standard [9]. Many methods exist for decoding a LDPC code, but the Belief propagation algorithm [24, 81] was chosen for its optimality. In [19, 82] a Belief propagation is conditioned to operate in a iterative decoding structure to relay the messages between the nodes in the Tanner graph. The decoding process of the belief propagation solves the following

$$\overline{\tilde{c}} \cdot \mathcal{H}^\top = \overline{s_{\mathcal{C}}} \, (\mathrm{mod}\, 2). \tag{4.29}$$

Each check node (equation) is dependent (edge exist) on a set of variable nodes (coded bits $\overline{\tilde{c}}_i$, $i \in [0, n_{\mathcal{C}} - 1]$) and each variable node is dependent on a set of check nodes. The aim of the Belief propagation is to compute the marginal posterior probabilities: $P(\overline{\tilde{c}}_i = 1 | \overline{s_{\mathcal{C}}}, \mathcal{H}),\ i \in [0, n_{\mathcal{C}} - 1]$ and these computations of the graph code are intractable due to the vast cycles [82]

inherent a Tanner graph. This is not problematic as the decoding process produces codewords, not marginal posterior probabilities. Lets denote the set l of coded bits $\overline{\tilde{c}}_l$ that participate in the m^{th} check equation of $\overline{s_{\mathcal{C}}}$ as $\mathcal{L}(m) \triangleq \{l : \mathcal{H}_{ml} = 1\}$. Likewise, lets define the set m check bits that code bit l of received vector $\overline{\tilde{c}}_l$ participate in as $\mathcal{M}(l) \triangleq \{m : \mathcal{H}_{ml} = 1\}$.

The algorithm starts by computing the soft values of the received codeword and to iteratively update the two a-posteriori probability ratios q^x_{ml} and r^x_{ml} [5, 19, 24]. Let q^x_{ml} denotes the probability that the l^{th} bit of the received codeword $\overline{\tilde{c}}_l$ has a value x, $x \in \mathbb{F}_2$, given the information obtained via the check nodes $\mathcal{M}(l) \setminus m$. Let r^x_{ml} denotes the probability that a check node m is satisfied when bit l is fixed to a value x and the other bits are independent with probabilities $q_{ml'}$, with $l' = \mathcal{L}(m) \setminus l'$.

Circulating the extrinsic information within a message passing decoder enhances the performance within a Bayesian network [19]. This is accomplished by excluding the outgoing edge when calculating the current node. This property of circulation of extrinsic information only, is expressed in the degree distribution from a edge perspective as

$$\lambda(x) = \sum_{i=1}^{\mathsf{l}_{\max}} \lambda_i \, x^{i-1}, \tag{4.30}$$

for the variable node and as

$$\rho(x) = \sum_{i=1}^{\mathsf{r}_{\max}} \rho_i \, x^{i-1}, \tag{4.31}$$

for the check node. The coefficients λ_i and ρ_i are associated with x^{i-1} rather than with x^i [27, 28]. During the examination of the message passing decoder it became apparent that $(i\text{-}1)$ incoming branches should be used and that outgoing branches be excluded to eliminate the use of self information. The decoding steps are in the following sections.

4.5.1 Log-Likelihood Ratios

It is more convenient to map the codeword $\overline{c}$ to an antipodal signal of $\{\pm 1\}$ for analysis. The log-likelihood ratio (LLR) is defined as function $LLR(\,\tilde{c}\,)$ expressed as

$$LLR(\,\tilde{c}_i\,) = ln\left(\frac{P(\tilde{c}_i = 1)}{P(\tilde{c}_i = 0)}\right) \qquad i \in [0, n_{\mathcal{C}} - 1], \tag{4.32}$$

given the probabilistic information for each coded bit from the mobile WiMAX receiver module. For a binary memoryless channel, the $LLR(\,\tilde{c}\,)$ of the received codeword $\overline{\tilde{c}}$ constitutes a

sufficient statistic with respect to decoding the codeword on a Tanner graph [64]. The rest of this section, both normal Belief propagation (plain text) and LLR operated Belief propagation (italic text) [83] will be explained [5].

4.5.2 Belief Propagation - Decoding Steps

4.5.2.1 Initialization Step

The Belief propagation decoder starts by buffering the initial prior probability values of the entire codeword into two seperate buffers as

$$p_l^1 = P(\tilde{c}_l = 1) \qquad l = 0, 1, 2, \ldots, (n_{\mathcal{C}} - 1), \tag{4.33}$$

$$p_l^0 = P(\tilde{c}_l = 0) \qquad l = 0, 1, 2, \ldots, (n_{\mathcal{C}} - 1). \tag{4.34}$$

The conditional matrix q_{ml}^x is preloaded respectively as

$$q_{ml}^1 = P(\tilde{c}_l = 1 | H_{ml} = 1) \qquad \text{for every } (l, m), \tag{4.35}$$

$$q_{ml}^0 = P(\tilde{c}_l = 0 | H_{ml} = 1) \qquad \text{for every } (l, m). \tag{4.36}$$

The Belief propagation decoder buffers the initial prior LLR values of the entire codeword into a buffer as

$$p_l = LLR(\tilde{c}_l) \qquad l = 0, 1, 2, \ldots, (n_{\mathcal{C}} - 1). \tag{4.37}$$

The LLR matrix q_{ml} is preloaded respectively with the initial prior LLR values as

$$q_{ml} = p_l \qquad \text{for every } (l, m). \tag{4.38}$$

4.5.2.2 Horizontal Step

In the horizontal step the conditional matrix r_{ml}^x is updated by going through all the check equations and computing the following two equations given as

$$r_{ml}^0 = \sum_{\{\tilde{c}_{l'} : l' \in \mathcal{L}(m) \setminus l\}} P(s_m | \tilde{c}_l = 0, \{\tilde{c}_{l'} : l' \in \mathcal{L}(m) \setminus l\}) \cdot \prod_{l' \in \mathcal{L}(m) \setminus l} q_{ml'}^{\tilde{c}_{l'}}, \tag{4.39}$$

$$r_{ml}^1 = \sum_{\{\tilde{c}_{l'} : l' \in \mathcal{L}(m) \setminus l\}} P(s_m | \tilde{c}_l = 1, \{\tilde{c}_{l'} : l' \in \mathcal{L}(m) \setminus l\}) \cdot \prod_{l' \in \mathcal{L}(m) \setminus l} q_{ml'}^{\tilde{c}_{l'}}, \tag{4.40}$$

and the syndrome vector is given as

$$\overline{s_{\mathcal{C}}} = [s_0\ s_1\ \ldots\ s_{nc}], \tag{4.41}$$

obtained from $Eq.$ (4.29). Finally, note that r^0_{ml}+r^1_{ml}=1 and was scaled accordingly [19, 83].

In the horizontal step the LLR matrix r_{ml} is updated by going through all the check equations and computing the following equation for all combinations of (l,m) as

$$r_{ml} = \ln\left(\left(1 - \prod_{l' \in \mathcal{L}(m)\backslash l} \frac{1-\exp(q_{ml'})}{1+\exp(q_{ml'})}\right) \cdot \left(1 + \prod_{l' \in \mathcal{L}(m)\backslash l} \frac{1-\exp(q_{ml'})}{1+\exp(q_{ml'})}\right)^{-1}\right). \tag{4.42}$$

4.5.2.3 Vertical Step

In the vertical step the conditional matrix q^x_{ml} is updated by going through all the variable nodes and computing the following equations as

$$q^0_{ml} = \zeta_{ml} \cdot p^0_l \prod_{m' \in \mathcal{M}(l)\backslash m} r^0_{m'l}\,, \tag{4.43}$$

and

$$q^1_{ml} = \zeta_{ml} \cdot p^1_l \prod_{m' \in \mathcal{M}(l)\backslash m} r^1_{m'l}\,, \tag{4.44}$$

with

$$\zeta_{ml} = \frac{1}{q^0_{ml} + q^1_{ml}}. \tag{4.45}$$

The posterior probabilities [19] are computed after each iteration as

$$q^0_l = \zeta_l \cdot p^0_l \prod_{m \in \mathcal{M}(l)} r^0_{ml}\,, \tag{4.46}$$

$$q^1_l = \zeta_l \cdot p^1_l \prod_{m \in \mathcal{M}(l)} r^1_{ml}\,. \tag{4.47}$$

In the vertical step the LLR matrix q_{ml} is updated by going through all the variable nodes and computing the following equation

$$q_{ml} = p_l + \sum_{m' \in \mathcal{M}(l)\backslash m} r_{m'l}\,. \tag{4.48}$$

The posterior LLR [19] is computed after each iteration as

$$q_l = p_l + \sum_{m \in \mathcal{M}(l)} r_{ml}\,. \tag{4.49}$$

4.5.2.4 Decoding Verification Step

In this step a provisional decoded codeword $\overline{d} = [d_0\ d_1\ \ldots\ d_{n_\mathcal{C}-1}]$ is created as

$$d_l = \begin{cases} 1 & \text{if } q_l^1 > q_l^0 \\ 0 & \text{if } q_l^1 < q_l^0 \end{cases} \qquad l = [0, 1, \ldots, n_\mathcal{C}-1]. \tag{4.50}$$

In this step a provisional decoded codeword $\overline{d} = [d_0\ d_1\ \ldots\ d_{n_\mathcal{C}-1}]$ *is created as*

$$d_l = \begin{cases} 1 & \text{if } q_l \geq 0 \\ 0 & \text{if } q_l < 0 \end{cases} \qquad l = [0, 1, \ldots, n_\mathcal{C}-1]. \tag{4.51}$$

A new syndrome $\overline{s_\mathcal{C}}$ is calculated as

$$\overline{d} \cdot \mathcal{H}^\top = \overline{s_\mathcal{C}} \,(\mathrm{mod}\, 2). \tag{4.52}$$

Both versions of the belief propagation algorithm terminates all processes if the syndrome satisfies a valid codeword ($\overline{s_\mathcal{C}} = \overline{0}$). If codeword $\overline{d}$ is not a valid codeword, then the decoder attempts another iteration (repeats $Eq.$ (4.39) - $Eq.$ (4.52)) until a valid codeword is found. The decoder declares a decoding failure and outputs the current codeword $\overline{d}$ when a preset maximum number of iterations are reached. It is shown in [28] that some degree distributions using Belief propagation message-passing can take up to 1800 iterations to propagate the fraction of error messages to zero. There exist several suboptimal Belief propagation implementations that yield nearly optimal results with reduced complexity [83, 84].

4.6 SIMPLIFICATIONS FOR ANALYSIS

The performance of a graph code can be analyze by tracking the propagating error messages inside the corresponding Tanner graph. Analyzing these messages is a daunting task and some simplifications were needed. These simplifications in the analysis process is presented in the next two sections.

4.6.1 Restriction to the All-Zero Codeword

It is convention to assume that the source encoder will produce an information symbols $\overline{b} = [b_0\ b_1\ \ldots\ b_{k_\mathcal{C}}]$ that is completely random in nature with the following properties as

$$P(b_i = 1) \triangleq P(b_i = 0), \qquad i = 0, 1, \ldots, k_\mathcal{C}, \tag{4.53}$$

$$R_{b_i b_i}(i) = \begin{cases} 1 & \text{if } i \triangleq 0, \\ 0 & \text{if otherwise,} \end{cases} \tag{4.54}$$

with R_{xx} denoting the autocorrelation function of the binary stream. Because the information source is uniformly distributed, then the codewords were produced uniformly. Tracking propagating error messages are possible only if the transmitted codeword is known prior to analysis. Finding codewords for the analysis is an extensive task for a code ensemble. This is accomplished by generating a parity-check matrix for a LDPC code that conforms to a certain degree distribution and from this the dual code (generator matrix) is found. Due to the sparseness of matrix $\mathcal{H}$, there exist orders of valid $\mathcal{G}$ that will provide correct encoding. The encoding process as stated in section 4.2 is a higher order complexity than the decoding process. In [17] the authors address the problem of lowering the complexity of the encoder, but in the process much of the designed degree distribution is lost and the graph code degrades in performance. The next step for analysis was to generate codewords to test is the Tanner graph and thereafter multiple LDPC codes must be generated to obtain the ensemble's average performance.

In [27] the concept of restricting the encoder to produce only the all-zero codeword is introduced for analysis. The all-zero codeword is always present in any linear block code to simplify analysis. The next important characteristic of the graph code is that is operates with message-passing of symbol/bit probabilities and is concerned with the fraction of error messages and how they are distributed. It is not dependent on the value of the coded bits but only on the reliability of the messages. As a consequence, we can transmit any particular codeword to analyze the system performance.

4.6.2 Concentration

The second simplification in the analysis of a code $\mathcal{C}$ was to observe the ensemble average performance rather than to analyze individual codes. It is shown in [27, 28] that an individual

code of the ensemble distribution has a performance equal to the ensemble average with a high probability. In Figure 4.2 an example of a tree graph is give on how all the messages stem from different neighbourhoods [27, 64] and propagate their message contents to the initial node in the center of the graph.

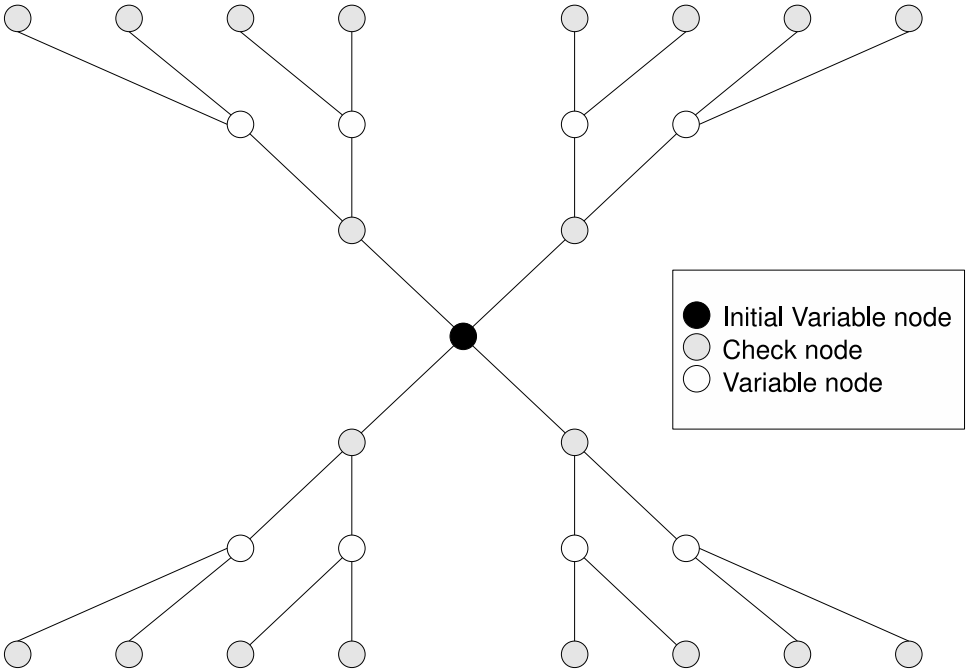

FIGURE 4.2: Tree graph with depth of 2 iterations for code $\mathcal{C}$

The check node update rule was given in $Eq.$ (4.42) and the variable node update rule was given in $Eq.$ (4.48). A tree graph is a visual presentation of all messages passed to a single node and is an alternative illustration of a Tanner graph. The probability of cycles being present in a given degree distribution can be calculated and is proved to be a function of the codeword length [64]. As $n_{\mathcal{C}} \rightarrow \infty$, the probability of cycles being present in the graph converges to zero. The edge distribution converges to a complete tree distributed graph that is express as

$$\lim_{n_{\mathcal{C}} \rightarrow \infty} \mathbb{E}_{\mathcal{C} \in LDPC(\lambda(x), \rho(x), n_{\mathcal{C}})}[P_b(\mathcal{C}, \sigma_{\eta(t)}, l)] = P_{T_l(\lambda(x), \rho(x))}(\sigma_{\eta(t)}). \tag{4.55}$$

Where $\sigma_{\eta(t)}$ is the noise variance and l is the number of iterations performed within the Belief propagation decoder. The tree ensemble graph is denoted by T_l with the corresponding expected error as P_{T_l}. An example of a tree graph is shown in Figure 4.2 and when used the code only circulates extrinsic information [19, 85] and will always converge to a stable edge network. After the edge network converged, the network can provide conditional probabilities as outputs. From all the design properties and the concentration theorem holds that the ensemble average

performace [27, 64] is given as

$$P\{|P_b(\mathcal{C}, \sigma_{\eta(t)}, l) - \mathbb{E}_{\mathcal{C}' \in LDPC(\lambda(x),\rho(x),n_\mathcal{C})}[P_b(\mathcal{C}', \sigma_{\eta(t)}, l)]| \geq \delta\} \leq \exp(-\varpi n_\mathcal{C}), \tag{4.56}$$

with $\varpi > 0$ and $\delta > 0$. In summary, by increasing the length of the codeword $n_\mathcal{C}$, the expected number of cycles are decreased within the Tanner graph. This converges the Bayesian network to a tree graph that the Belief propagation operates on and will result in a high probability of similiar results being produced from the belief propagation decoder.

4.7 NOISE THRESHOLD

The performance of the decoding process is a function of the fraction and distribution of unreliable messages. Thus if there exist enough incorrect messages at key positions, the Belief propagation will fail to converge to a valid codeword in the Hamming space. From this follows two classifications of decoding solutions. The first is a successful decoding process and is expressed as

$$\lim_{l\to\infty} P_{T_l(\lambda(x),\rho(x))}(\sigma_{\eta(t)}|\sigma_{\eta(t)} \leq \sigma^*_{\eta(t)}(\lambda(x), \rho(x))) \approx 0. \tag{4.57}$$

Where $\sigma_{\eta(t)}$ is the noise variance and $\sigma^*_{\eta(t)}$ is the threshold variance for a given code. $Eq.$ (4.57) states that the fraction of errors within a Tanner graph is expected to converge to zero when the noise variance of the channel is less than the noise threshold of the code. A failed decoding process is expressed as

$$\lim_{l\to\infty} P_{T_l(\lambda(x),\rho(x))}(\sigma_{\eta(t)}|\sigma_{\eta(t)} > \sigma^*_{\eta(t)}(\lambda(x), \rho(x))) \geq \psi. \tag{4.58}$$

Where ψ is a positive constant and $\sigma^*_{\eta(t)}$ is the threshold variance for a given code. $Eq.$ (4.58) states that the fraction of error within a Tanner graph is expected to converge to a constant value of ψ when the channel's variance is larger than the threshold's variance. The noise threshold $\sigma^*_{\eta(t)}$ is the largest variance that the Belief propagation decoder can accommodate to iterate to a zero bit probability. This threshold is the supremum of the channel's variance range and is defined as

$$\sigma^*_{\eta(t)}(\lambda(x), \rho(x)) = \sup\{\sigma_{\eta(t)} \in [0, \infty] : \lim_{l\to\infty} P_{T_l(\lambda(x),\rho(x))}(\sigma_{\eta(t)}) \to 0\}. \tag{4.59}$$

The goal of graph code optimization is to obtain a degree distribution pair $(\lambda(x), \rho(x))$ of a predetermined code rate $R_c(\lambda(x), \rho(x))$=R_c that would yields the largest possible noise threshold $\sigma^*_{\eta(t)}(\lambda(x), \rho(x))$.

4.8 DENSITY EVOLUTION

Density evolution is an algorithm that determines the noise threshold $\sigma^*_{\eta(t)}$ for a given degree distribution pair $(\lambda(x), \rho(x))$. This is accomplished by computing the density evolution equation

$$a_{iter}(l) = a_0(l) * \lambda(\rho(a_{iter-1})), \tag{4.60}$$

where the L-density a (see appendix C) is a presentation of the LLR probability density function and define the following operators as

$$\lambda(a_{iter}(l)) = \sum_{j=2}^{\mathsf{l}_{\max}} \lambda_j (a_{iter}(l)^{*(j-1)}), \tag{4.61}$$

and

$$\rho(a_{iter}(l)) = \Gamma^{-1}\left(\sum_{j=2}^{\mathsf{r}_{\max}} \rho_j (\Gamma(a_{iter})^{\circledast(j-1)}) \right). \tag{4.62}$$

With $iter$ denoting the current iteration number. The density evolution algorithm starts by obtaining an initial log-likelihood statistical distribution (L-density) of the communication channel. The mean of the l-density is positive due to the analysis of the all-zero codeword with the mapping of $0 \rightarrow 1$ and $1 \rightarrow -1$ that was used in the analyzing modulation scheme (see section 4.5.1). The probability of the bit error expected in a l-density is computed as

$$P_b(a_{iter}(l)) = \int_{-\infty}^{0} a_{iter}(z) dz. \tag{4.63}$$

The initial l-density for both AWGN and a Rayleigh faded channel [29] is given as

$$a_0(l) = a_{\text{AWGN}}(l) = \frac{\sigma_{\eta(t)}}{2\sqrt{2\pi}} \exp\left(-\frac{(l - 2/\sigma^2_{\eta(t)})^2}{2(4/\sigma^2_{\eta(t)})} \right), \tag{4.64}$$

and

$$a_0(l) = a_{\text{Ray}}(l) = \frac{\sigma_{\eta(t)}}{2\alpha\sqrt{2\pi}} \exp\left(\frac{(l - 2\alpha^2/\sigma^2_{\eta(t)})^2}{8\alpha^2/\sigma^2_{\eta(t)}} \right). \tag{4.65}$$

With l being the log-likelihood ratio of the code bit obtained after detection and α being the corresponding fading amplitude for the current code bit. After the initial density function for the communication channel is obtained, $Eq.$ (4.60) is recursively executed for a specific $\sigma^2_{\eta(t)}$ until $P_{a_i(l)} \leq \mathcal{E}$ is satisfied from $Eq.$ (4.63), where $\mathcal{E}$ is a preset bit error probability[2]. If $\sigma_{\eta(t)} < \sigma^*_{\eta(t)}$, then the recursive computation of $Eq.$ (4.60) yields a l-density of

$$\lim_{iter\to\infty} a_{iter}(l) \approx \Delta_\infty. \tag{4.66}$$

If the recursive computation of $Eq.$ (4.60) yield the desired $\mathcal{E}$, then the noise variance $\sigma^2_{\eta(t)}$ is increased and the density evolution is performed once more. This is done continually until a large enough noise variance $\sigma^2_{\eta(t)}$ is obtained for which the criteria can't be satisfied. The largest noise variance that yields the criteria is defined as the noise threshold (see section 4.7). It is shown in [28], that almost 1800 iterations is needed to attain the required bit error probability. The complete process discussed above is utilized to obtain the noise threshold of a single graph code's $\mathcal{C}$ degree distribution pair. Many authors [27–29] have used differential evolution [29, 86] to acquire degree distributions near Shannon's capacity [26] and several suboptimal methods have been proposed [87, 88] that uses the central limit theorem to simplify the process [75].

4.8.1 Stability Conditions

It is always desirable to ensure stability in the message-passing decoder so that it will converge to a zero bit error probability. This stability is of importance in the operable range of $\sigma_{\eta(t)} < \sigma^*_{\eta(t)}$. If the following condition holds

$$\mathcal{B}(a_{\text{channel}}(l))\lambda'(0)\rho'(1) < 1, \tag{4.67}$$

(where $\mathcal{B}(\cdot)$ is the Bhattacharyya constant [89]) then the l-density will evolve according to $Eq.$ (4.66). For an AWGN channel this reduces from

$$\mathcal{B}(a_{\text{AWGN}}(l))\lambda'(0)\rho'(1) < 1, \tag{4.68}$$

to

$$\exp\left(\frac{-1}{2\sigma^2_{\eta(t)}}\right)\lambda'(0)\rho'(1) < 1. \tag{4.69}$$

[2] Typically $\mathcal{E}$=10^{-8}

Now a upper bound for the noise threshold is equal to

$$\sigma^*_{\eta(t)} \leq \frac{1}{\sqrt{2\ln(\lambda'(0)\rho'(1))}}. \tag{4.70}$$

4.9 LIMITATIONS OF CYCLE-FREE LOOPS

In this section one of the drawbacks in the design of LDPC code was discussed. The edges in the Tanner graph has a high probability of taking on the shape of a tree ensemble $T_l(\lambda(x), \rho(x))$ when the codeword length increases. This is desirable due to the fact that the graph will then converge to a stable condition, given enough iterations were performed by the belief propagation decoder.

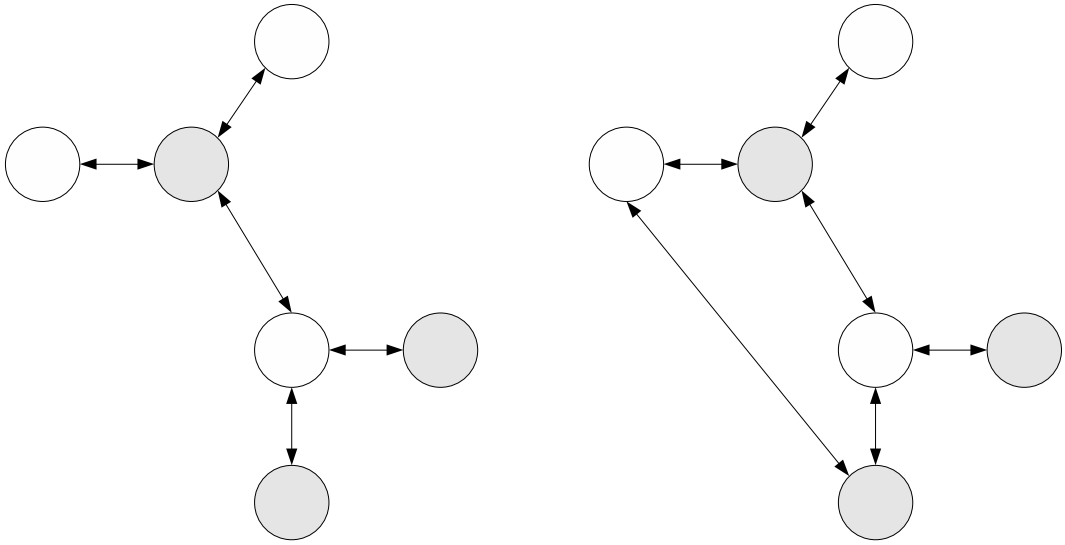

FIGURE 4.3: Left: Tree ensemble example. Right: Cycle-4 graph example.

In the construction of a LDPC code there is always a probability that an edge connects two nodes to form a cycle within a graph. In Figure 4.3 an example of a graph with a cycle of length 4 is given. The property of passing only extrinsic information is lost in the presence of a cycle and this causes a reduction of the performance of the graph code.

Definition 4.9.1 *The shortest cycle that is present inside a graph is known as the girth of the code $\mathcal{C}$.*

The girth for a tree shape graph is infinite and according to [19] is the most effective shape for decoding a graph. A method of detecting cycles (loops) inside a graph is proposed in

[90, 91] and was used in the construction of the codes. The *Progressive Edge Growth (PEG)* algorithm [92, 93] is a method used for constructing codes with large girths. The PEG algorithm progressively connects an edge between two nodes and then verifies if the girth of the code is higher than a preset quantity. This method was used for code construction in this dissertation and has shown to lower the error floor [94] that are expected with cycles in the design of a LDPC code [95].

From this discussion it appears that only tree ensembles should be pursued in code construction. Unfortunately there are some drawbacks in using a tree ensemble for finite length analysis of a code. For a fixed codeword length $n_{\mathcal{C}}$, a very sparse[3] parity-check matrix $\mathcal{H}$ is required to create a tree shape graph. This very sparse matrix lowers the overall Hamming distance and decreases the overall code $\mathcal{C}$ performance. A code with a tree graph has at least $\#_{\mathcal{C}}$ codewords of Hamming weight 2 [64], where $\#_{\mathcal{C}}$ is equal to

$$\#_{\mathcal{C}} = n_{\mathcal{C}} \cdot \frac{2R_c - 1}{2}. \tag{4.71}$$

From $Eq.$ (4.71), a rate above or below $R_c = \frac{1}{2}$ has a high probability of containing more low weight codewords $\#_{\mathcal{C}}$ and hence deteriorates the overall performance [96], and hence only half-rate codes will be evaluated. The bit error probability for a tree graph can also be characterized by the initial l-density $a_0(l)$ of the communication channel and MAP decoding as [64] as

$$P_b = (2R_c - 1) \cdot P_b(a_{iter}(l) * a_{iter}(l)). \tag{4.72}$$

The drawback of using a very sparse code is the slow converging in the Tanner graph to eliminate the error messages. A *wave effect* [19] is found in dense factor nodes because the reliable information messages are spread over the Tanner graph rapidly and results in fast converging networks. In Figure 4.4 and 4.5 the evolution of the degree distribution is shown as the performance of the LDPC approaches the Shannon's capacity [2] limit. In [28] the authors presents optimized degree distributions that are within 0.06dB of capacity for a AWGN channel and in [29] the authors presents optimized degree distributions that are within 0.07dB of capacity for a Rayleigh faded channel.

Good codes' [19] degree distribution require a heavy weight at λ_2 and at $\lim_{x\to\infty} \lambda_x$. For example, the authors in [28, 29] use heavy distribution weight of λ_{50} to obtain excellent BER

[3] Very sparse codes are more than a constant factor sparser than sparse codes

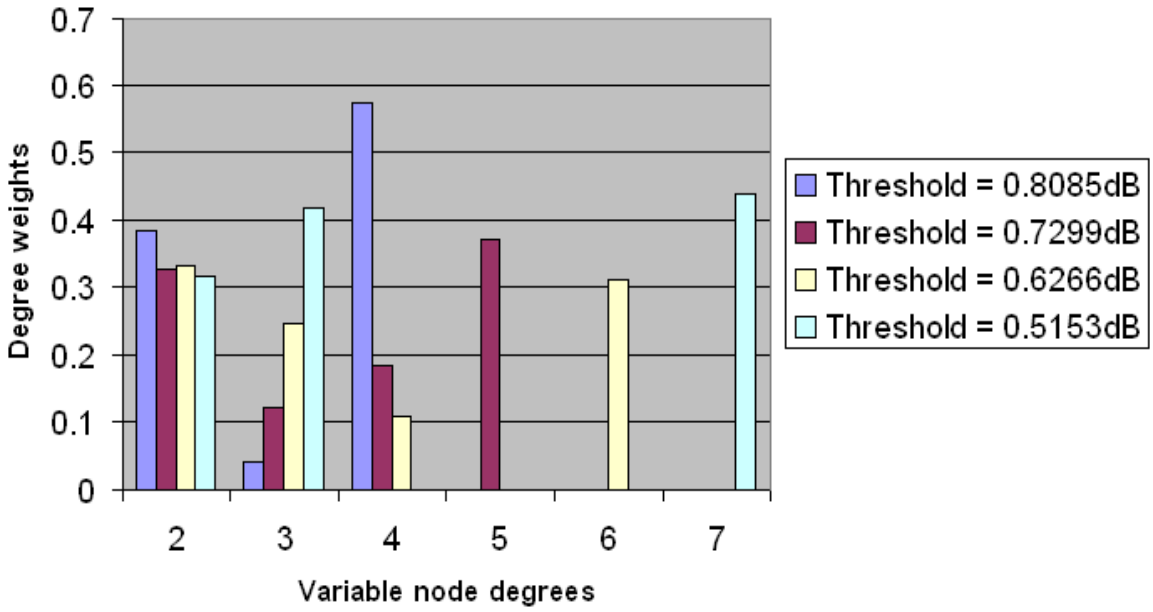

FIGURE 4.4: Optimized variable node degree distribution for a half-rate LDPC code.

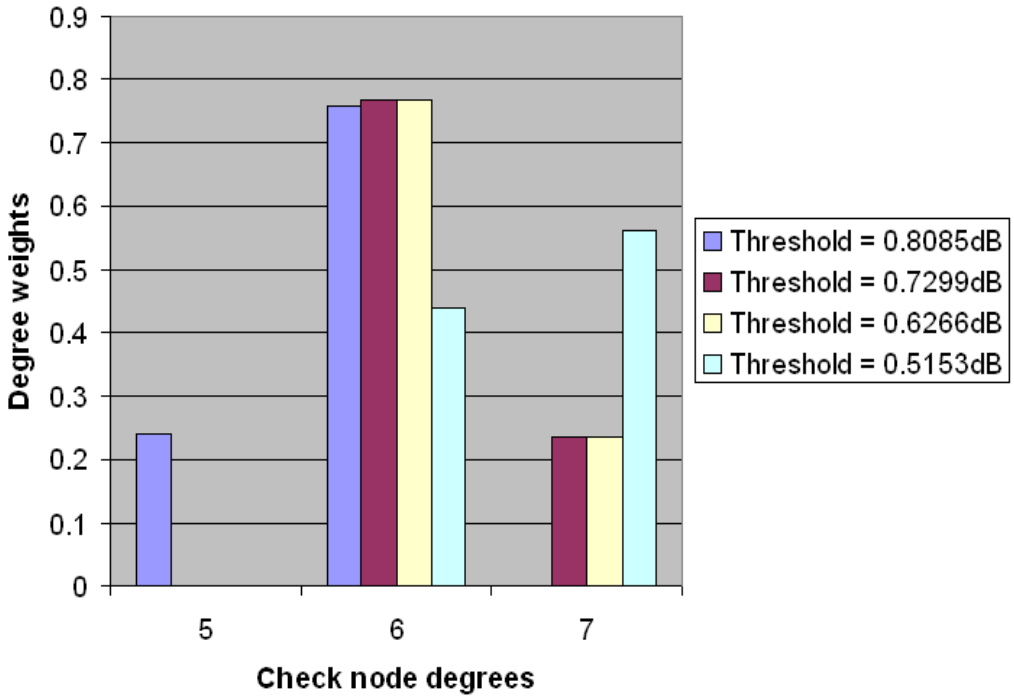

FIGURE 4.5: Optimized check node degree distribution for a half-rate LDPC code.

results. This is unfortunately an extremely limiting factor if working with codeword length $n_C < 2500$ and the graph code causes groups of cycles. Thus a balance must be achieved that uses heavy degrees but limits the number of cycles, while also extending the length of the girth to a maximum. In summary, a balance between the density of matrix and the induce error

floor must be found. The higher the density, the lower the noise threshold but the higher the error floor for a finite length LDPC code. The reverse is true that the lower the density the higher the noise threshold but the lower the error floor. Another method was to modify the belief propagation decoder to compensate for the deliberately induced cycles [97, 98], that will improve BER performance for short length codewords.

4.10 OPTIMIZING A LDPC CODE FOR A SATURATED AMPLIFIER

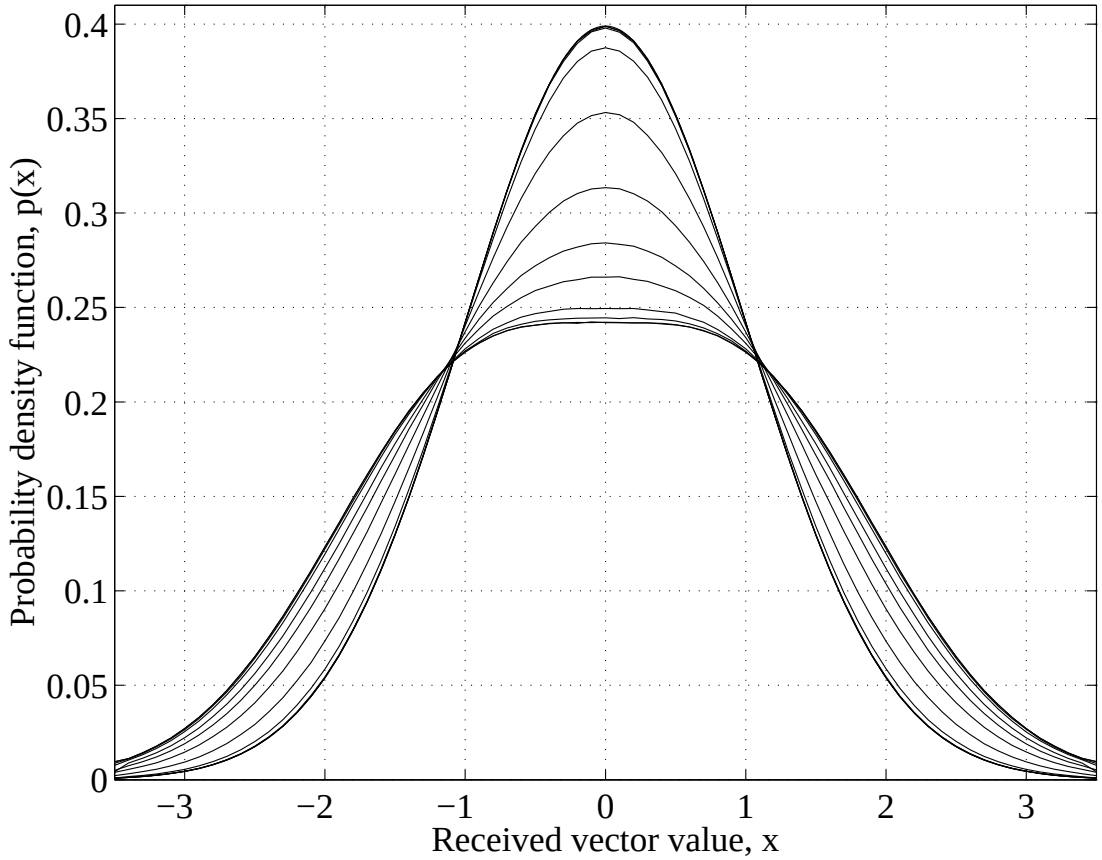

FIGURE 4.6: Density evolution of the channel's PDF with increasing PCL.

The objective of this dissertation is the optimization of a LDPC code for an OFDM modulation scheme with a saturated power amplifier. The effect that peak windowing and clipping has on a turbo code and LDPC code was evaluated in [51] and shows the loss in BER performance to the gain in distance with more saturation at the amplifier. Several methods have been developed to further improve the BER performance in this saturated amplifier OFDM system.

An improvement was acquired by employing a selective mapping approach with an error control code [99]. Another method was to form clusters in the parity-check matrix $\mathcal{H}$ of the LDPC code to spread the effects of the inband distortions to several OFDM symbols [100]. In this dissertation, the density evolution method was used to optimize a LDPC code for a saturated OFDM symbol. The first step in the analysis was to obtain an initial channel's distribution with the saturated OFDM symbol effect included. The initial l-density channel's distribution was acquired through numerical analsis and the results are shown in figure 4.6.

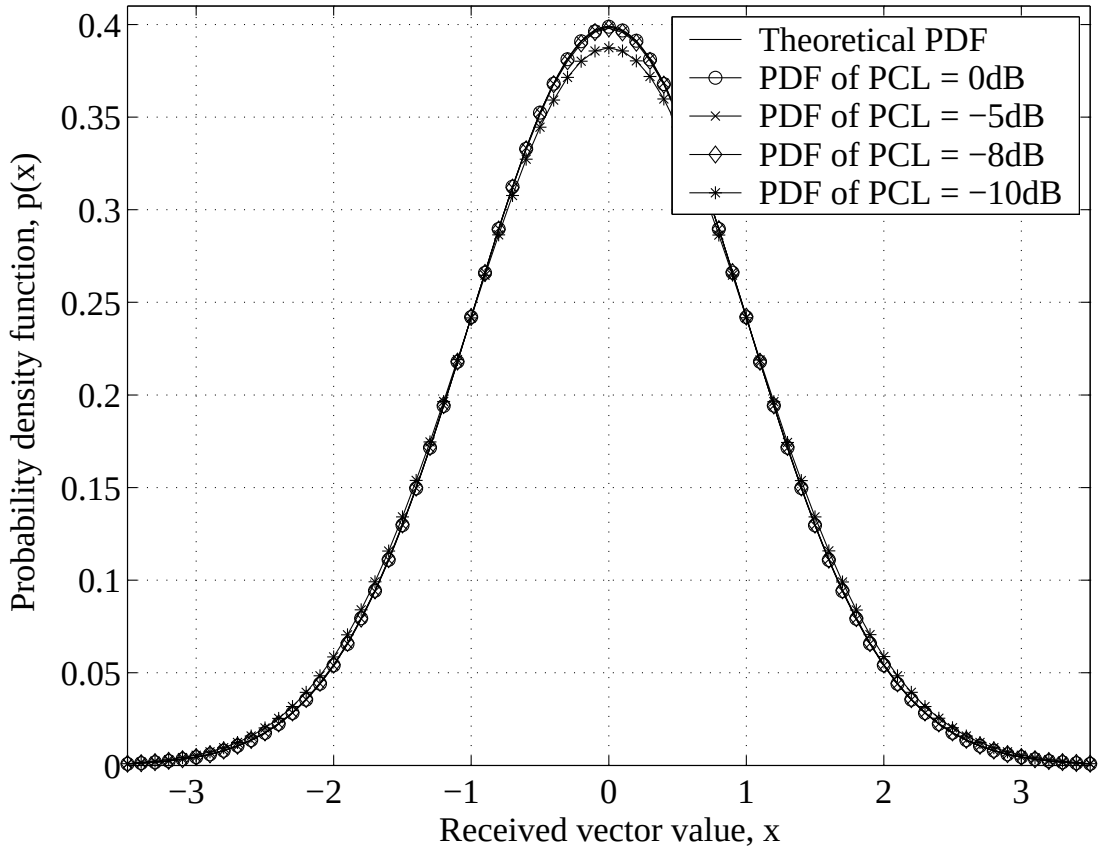

FIGURE 4.7: Density evolution of the channel's PDF with increasing PCL (above average transmission power).

It was shown that the initial channel's probability density function remained intact and is denoted by $a_0(l)$. The initial channel PDF $a_0(l)$ does not change in form with a saturated amplifier, except the variance of the process increases with saturation at the amplifier. The power clipping levels above the average transmission power was of interest otherwise too many unreliable messages are produced within the Tanner graph. The power clipped levels of interest is shown in Figure 4.7 and the results from the channel's PDF forming was desirable in obtaining a degree distributions for the LDPC code.

Degree distributions has been found to optimized both a static AWGN PDF and a Rayleigh PDF [28, 29]. The saturated amplifier in an OFDM symbol increases the noise threshold of the graph code. Degree distributions [28, 29] were used to construct LDPC codes according to the constraints presented in a finite length analysis. The constructed LDPC codes were compared to the standardized LDPC code to observe improvements for a mobile WiMAX system [8] and are shown in chapter 5. The optimized LDPC codes outperformed the standardized code because of the improved noise threshold [28, 29] calculated by the density evolution algorithm for the degree distributions. This is a motive to pursue optimized LDPC codes presented in [28, 29] for future developed communication standards.

4.11 CONCLUDING REMARKS

An alternative method was proposed in this chapter to combat the effect that a saturated amplifier has on an OFDM symbol. A graph code known as a LDPC code was used to combat these effects by means of a method known as density evolution. Density evolution analyzes the channel's PDF with the induced saturated amplifier to optimize a Tanner graph. When a Tanner graph is optimized in the design it will effectively eliminate the error messages through the use of the belief propagation algorithm.

CHAPTER FIVE
SIMULATION RESULTS

5.1 CHAPTER OVERVIEW

This chapter evaluates the performance of three coding schemes in a range of channel conditions. All the simulation results were performed on a mobile WiMAX simulation platform [8] developed as part of this dissertation. Table 5.1 lists the simulation parameters that were used in this chapter.

TABLE 5.1: Overall Simulation Environment Parameters

Description	**Value**
Transmission mode	FUSC
FFT size	128-point
Sampling Time	700ns
Carrier frequency	2.5GHz
Cell ID number	$< 0\ 0\ 0 >$
Subchannels	2

The FUSC mode was used in the physical layer for performance analysis. This mode was used for the frequency spreading of subchannels over the entire channel bandwidth. The simulation was setup to emulate a subscriber station that operates at the cell's edge of the serving base station. In section 5.2 the uncoded mobile WiMAX system was evaluated in a range of channel

conditions. Section 5.3 evaluates the performance of a convolutional code in a mobile WiMAX environment which was used as a benchmark for the other coding schemes. In section 5.4, the performance of the standardized LDPC code was evaluated and the optimized LDPC code was evaluated in section 5.5. The chapter concludes with a discussion of the overall performance observed and comments on future implementations.

5.2 EVALUATION OF THE MOBILE WIMAX PLATFORM

In this section the performance of the developed mobile WiMAX platform was evaluated by way of BER analysis. Three different channel scenarios were addressed as part of the analysis for mobile WiMAX while the channel encoder and channel decoder were omitted in this section.

5.2.1 Performance Analysis in a Static AWGN Channel

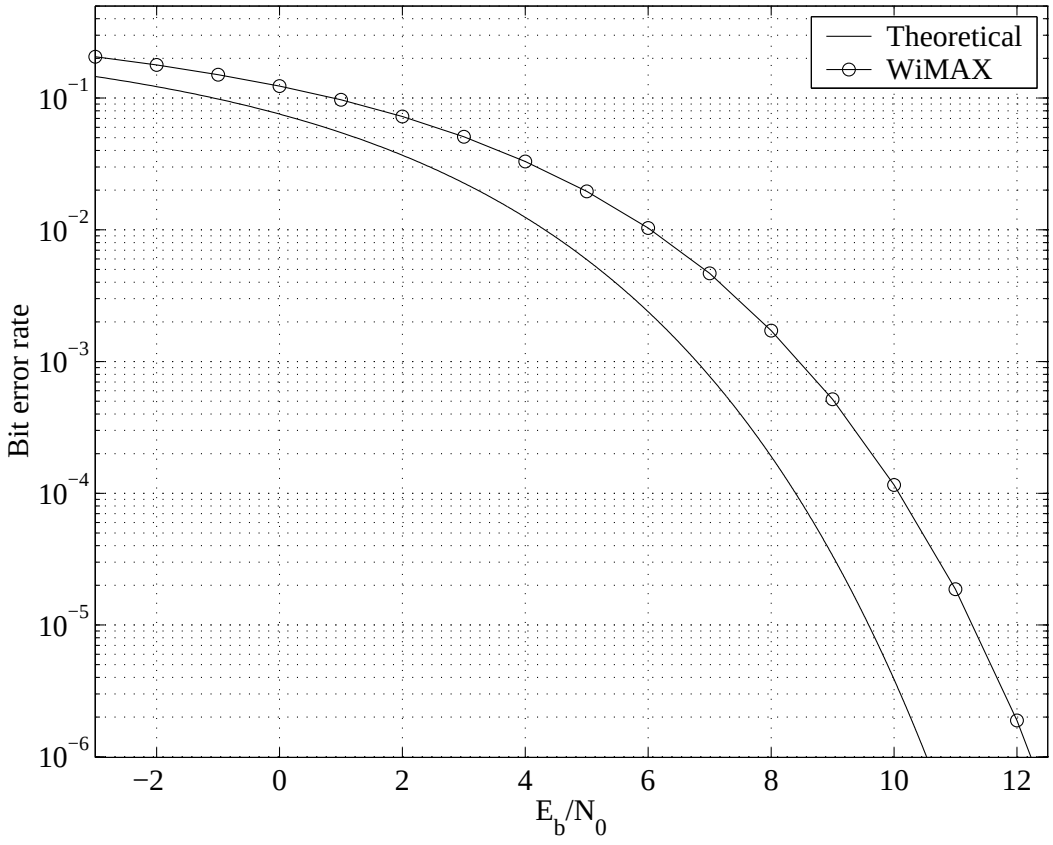

FIGURE 5.1: BER graph for an uncoded WiMAX system in a static AWGN channel.

The first channel condition to address was the static AWGN channel and the simulation

parameter for the uncoded mobile WiMAX platform is given in table 5.2.

TABLE 5.2: Simulation Environment Parameters for Figure 5.1

Description	**Value**
Channel	Static AWGN
Cyclic Prefix Length	1/4
Data Modulation	4-PSK
Channel PDP	Single-tap channel

In Figure 5.1 a comparison of the mobile WiMAX system is made to the narrowband complex QPSK theoretical curve [30, 39]. The mobile WiMAX system uses amplified pilot bands, guard bands (left, right and DC) and a cyclic prefix that makes up the difference in the two performance curves. The cyclic prefix was set to the maximum allowable length [8] to show the loss in bandwidth. The WiMAX system has an asymptotic loss of 1.6854 dB compared to the theoretical QPSK curve in a static AWGN channel. The asymptotic loss is of the overall throughput scaling calculated in $Eq.$ 2.54 on page 26 and the power normalization of the reference and guard bands in each OFDM symbol.

5.2.2 Performance Analysis in a Frequency Non-Selective Fading Channel

TABLE 5.3: Simulation Environment Parameters for Figure 5.2

Description	**Value**
Channel	Frequency non-selective fading
Maximum Doppler Shift	104Hz
Cyclic Prefix Length	1/4
Data Modulation	4-PSK
Channel PDP	Single-tap channel

The second channel condition to consider is a frequency non-selective fading channel and the simulation parameters are given in table 5.3. Figure 5.2 presents a comparison between the mobile WiMAX system and a narrowband complex QPSK theoretical curve for a flat fading channel [30]. The WiMAX system has an asymptotic loss of 1.674 dB compared to the theoretical QPSK curve in a frequency non-selective fading channel. The asymptotic loss is of the overall throughput scaling calculated in $Eq.$ 2.54 on page 26 and the power normalization of the reference and guard bands in each OFDM symbol.

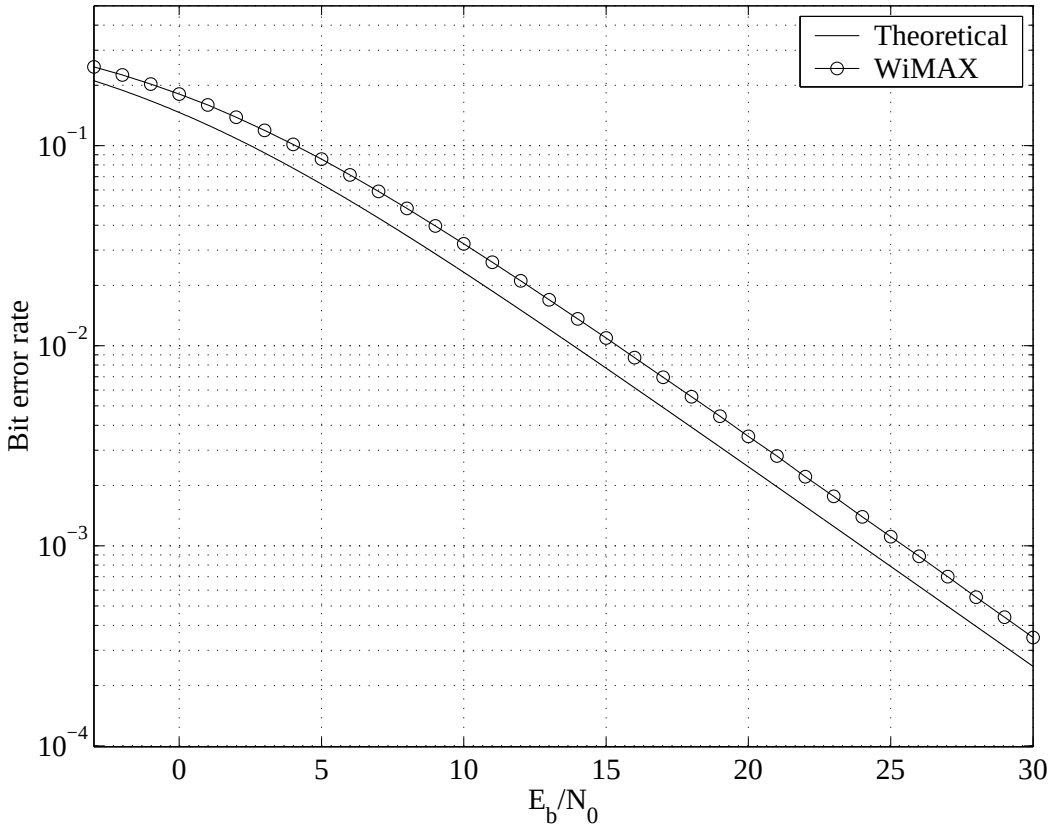

FIGURE 5.2: BER graph for uncoded WiMAX system in a frequency non-selective fading channel.

5.2.3 Performance Analysis with a Saturated Transmission Amplifier

The third channel condition is the frequency selective fading channel with four peak clipping levels (PCL). The simulation parameters are given in table 5.4 and the *ITU Pedestrian-B Channel 103 model*[1] was used in this simulation. A higher modulation scheme was used

[1] Physical degraded channel response presented in appendix A

for a more comprehensive observation of the effect that peak clipping levels have on a communication system.

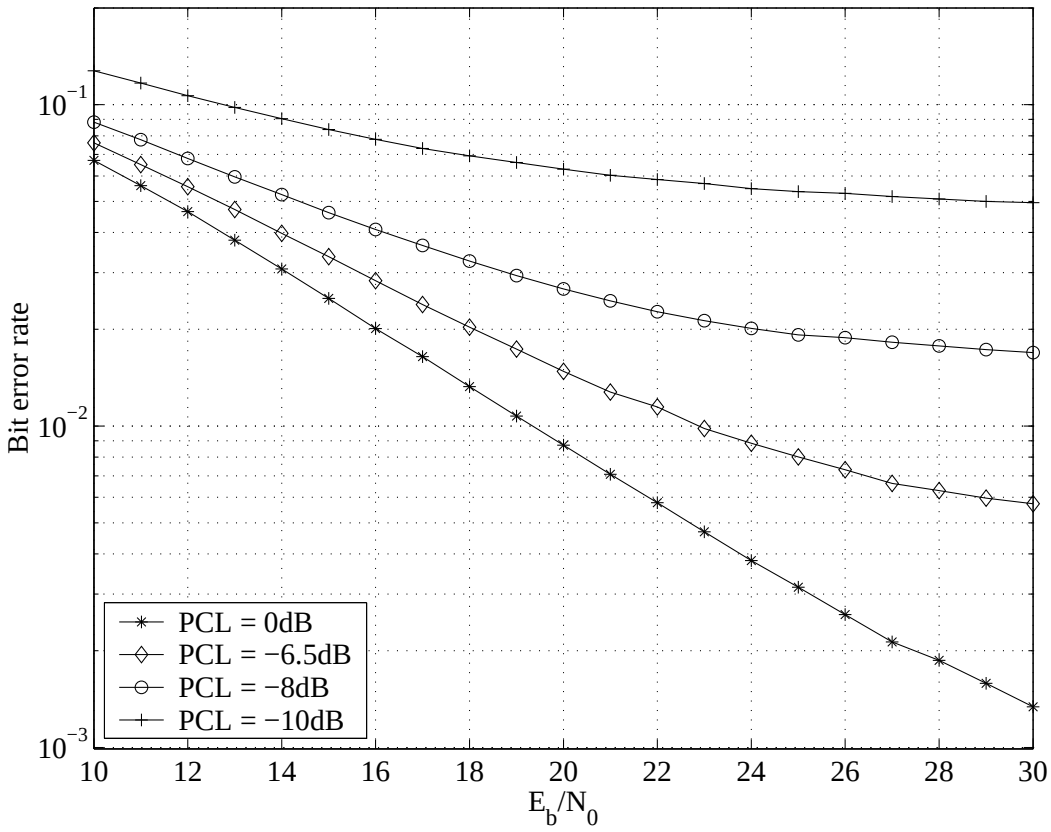

FIGURE 5.3: BER graph for a uncoded WiMAX system with peak clipping at the transmitter.

TABLE 5.4: Simulation Environment Parameters for Figure 5.3

Description	**Value**
Channel	Frequency selective fading
Maximum Doppler Shift	104Hz
Cyclic Prefix Length	1/8
Data Modulation	16-QAM
Channel PDP	ITU Pedestrian-B Channel 103
Channel Estimation	Least Square Estimation
Interpolation method	Wiener Interpolator

A least squares channel estimator was used to accurately estimate the channel impulse response in each of the OFDM symbols and a Wiener interpolator was used subsequently to interpolate the data subcarriers that were linearly equalized. In Figure 5.3 the four different peak clipping levels over the uncoded mobile WiMAX system was shown. The error floor increases as the peak clipping level decreases[2] and the system does not reach a BER of 10^{-3} in the evaluated E_b/N_0 range.

5.3 EVALUATION OF THE CONVOLUTIONAL CODE

In this section the focus was to establish a benchmark for other coding schemes and this was done by evaluating the mandatory convolutional code [8] on a mobile WiMAX platform.

5.3.1 Performance Analysis in a Static AWGN Channel

A $1/3$-rate convolutional code with a short constraint length $\mathcal{K} = 3$ was implemented to show the improvement by increasing the constraint length $\mathcal{K}$, as with the NASA code. The simulation parameters are given in table 5.5 for this section.

TABLE 5.5: Simulation Environment Parameters for Figure 5.4

Description	**Value**
Channel	Static AWGN
Cyclic Prefix Length	1/4
Data Modulation	4-PSK
Channel PDP	Single-tap channel

An asymptotic coding gain [70] of 1.4238 dB was observed with the hard decision Viterbi decoding algorithm for a convolutional code, $\mathcal{K} = 3$, compared to the uncoded mobile WiMAX system at a BER of 10^{-6}. An asymptotic coding gain of 3.7621 dB was obtained when using the soft decision Viterbi decoding algorithm at a BER of 10^{-6}. The NASA[3] code is plotted in Figure 5.4 with a coding gain of 3.4691 dB when the hard decision Viterbi decoding algorithm

[2] Lower peak clipping level at the transmitter
[3] $1/2$-rate convolutional code with constraint length $\mathcal{K} = 7$

was used and a coding gain of 5.80824 dB when the soft decision Viterbi decoding algorithm was used at a BER of 10^{-6}. A coding gain of 2.0461 dB was acquired when the number of states in the convolutional code was increased from 4 to 64. This concludes that while the performance gain is linear, the complexity growth is exponential. Thus increasing the constraint length of the convolutional code becomes an unfeasible solution.

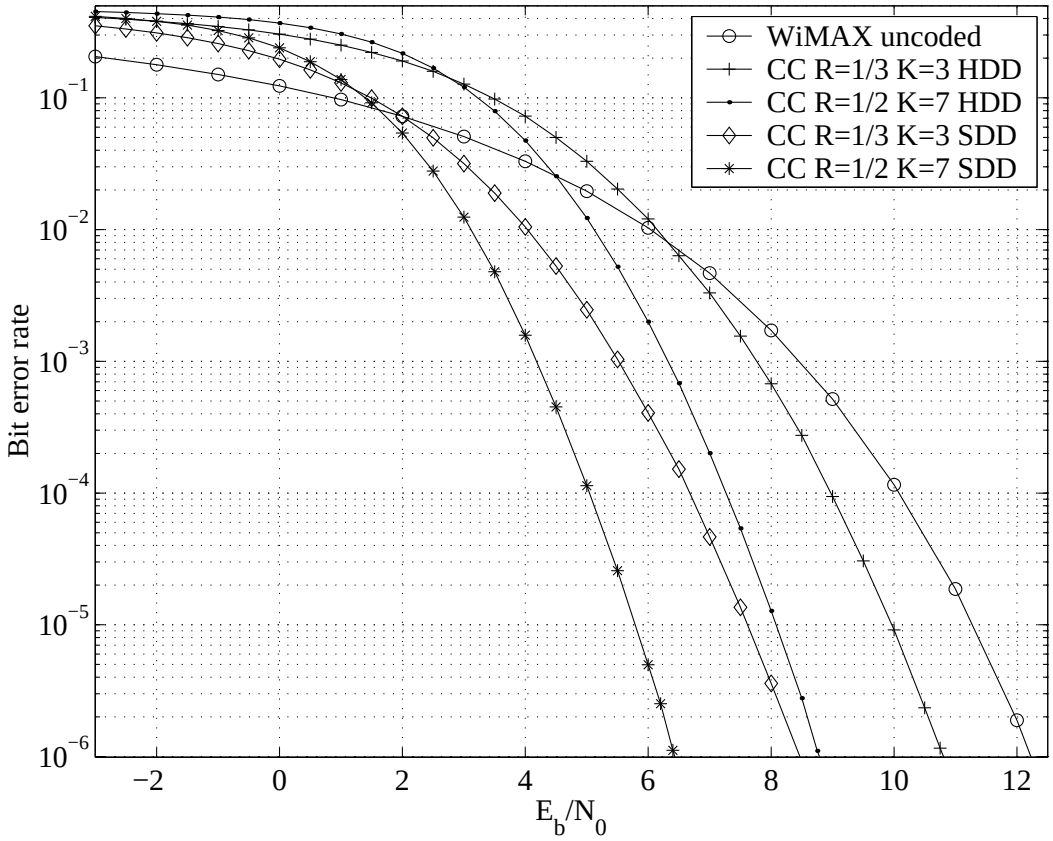

FIGURE 5.4: BER graph for a convolutional coded WiMAX system in a static AWGN channel.

5.3.2 Performance Analysis in a Frequency Non-Selective Fading Channel

In this section the convolutional codes were evaluated on a frequency non-selective fading channel and the simulation parameters are given in table 5.6.

The hard decision decoded $1/3$-rate convolutional code with $\mathcal{K} = 3$ has a asymptotic coding gain of -2.8866 dB to the uncoded mobile WiMAX system and the soft decision decoded $1/2$-rate convolutional code with $\mathcal{K} = 7$ has a coding gain of -1.0953 dB at a BER of 10^{-3}. This proves that a longer constraint length improves the performance on the communication

system. When perfect channel state information (CSI) was supplied to the Viterbi decoding algorithm an asymptotic coding gain of 0.7215 dB was observed to the uncoded WiMAX system at a BER of 10^{-3}. An interleaver was used to obtain more time diversity [40, 101] and for the NASA code an improvement in the system performance can be seen in Figure 5.5. For a hard decision Viterbi decoding algorithm a asymptotic coding gain of 7.755 dB was found for an expected BER of 10^{-3} and higher coding gains at higher E_b/N_0 values to the uncoded WiMAX system. The soft decision Viterbi decoding algorithm has an infinite[4] coding gain. The BER performance was further improved by 0.6372 dB when the decoding process was supplied with perfect CSI. The conclusion is that a convolutional code only exerts good performance when the memory inherent in the code is extended over a range of fades. This is accomplished by either an interleaver or a long contraint length that both have a length significantly longer than the inverse of the coherence bandwidth (section 2.3.1.2).

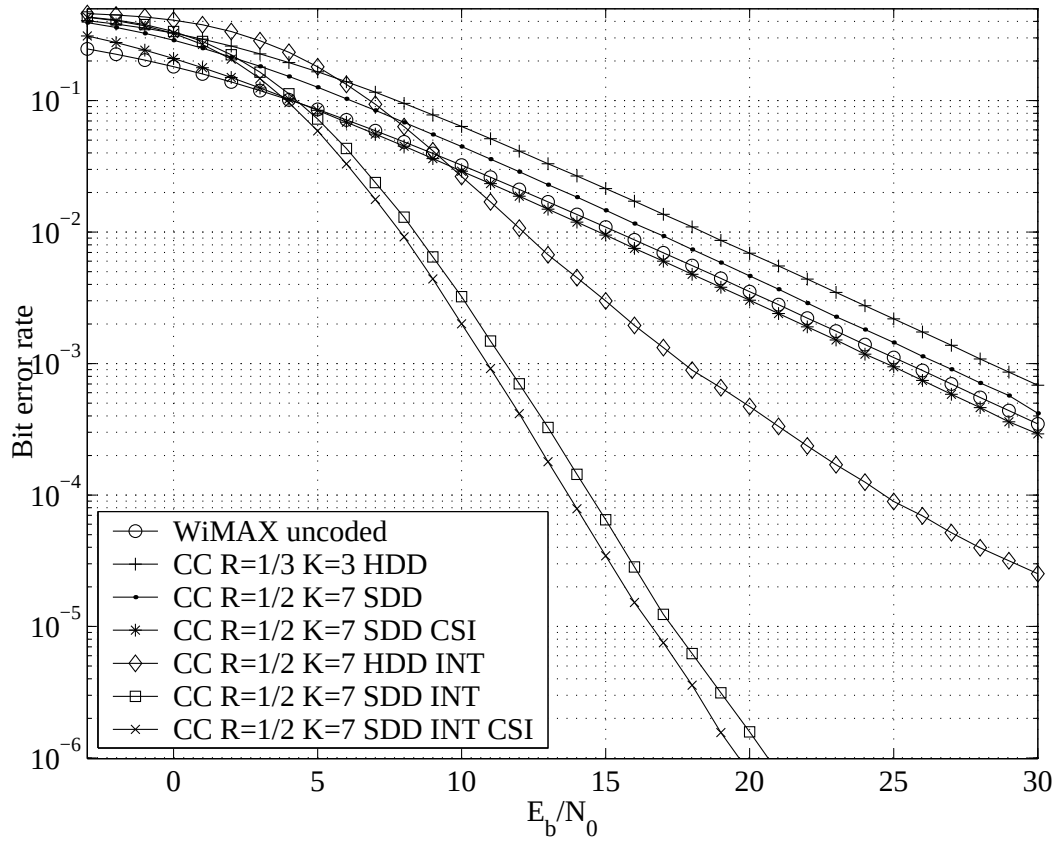

FIGURE 5.5: BER graph for a convolutional coded WiMAX system in a frequency non-selective fading channel.

[4] No asymptotic comparison to performance curves

TABLE 5.6: Simulation Environment Parameters for Figure 5.5

Description	**Value**
Channel	Frequency non-selective fading
Maximum Doppler Shift	104Hz
Cyclic Prefix Length	1/4
Data Modulation	4-PSK
Channel PDP	Single-tap channel

5.3.3 Performance Analysis with a Saturated Transmission Amplifier

In this section the performance in a frequency selective fading channel with four peak clipping levels (PCL) was evaluated and the simulation parameters are given in table 5.7.

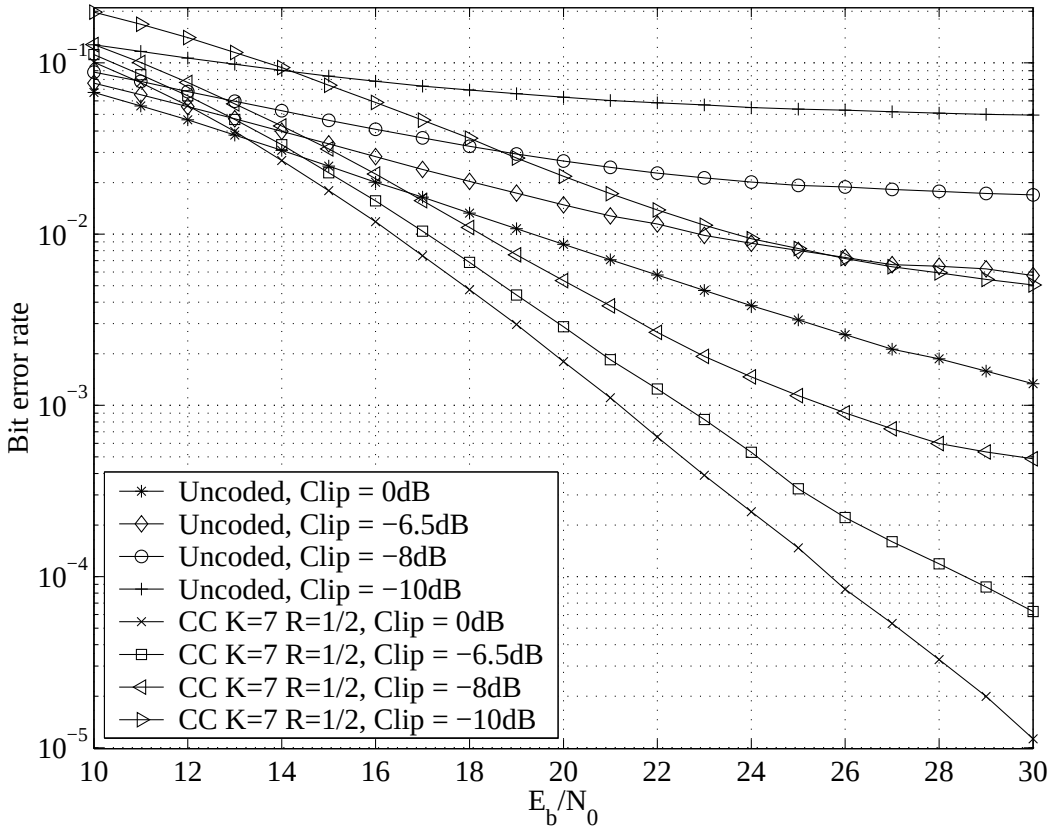

FIGURE 5.6: BER graph for a convolutional coded WiMAX system with peak clipping at transmitter.

In Figure 5.6 the performance of the NASA convolutional code was compared to the uncoded mobile WiMAX system. Three of the four peak clipped convolutional codes outperforms the uncoded system without any clipping and has an infinite coding gain. Convolutional codes have been applied to selective mapping techniques [102–105] to obtained a further 2.6 dB in coding gain with a saturated transmission amplifier. The selective mapping technique is a method that inserts redundant bits at the transmitter and treats the raised cosinus filter as a convolutional encoder. Due to the constraints of the mobile WiMAX standard [8], the selective mapping method was not implemented. The LDPC code still outperforms the convolutional code even with the additional 2.6 dB coding gain from the convolutional coded selective mapped OFDM symbol.

TABLE 5.7: Simulation Environment Parameters for Figure 5.6

Description	**Value**
Channel	Frequency selective fading
Maximum Doppler Shift	104Hz
Cyclic Prefix Length	1/8
Data Modulation	16-QAM
Channel PDP	ITU Pedestrian-B Channel 103
Channel Estimation	Least Square Estimation
Interpolation method	Wiener Interpolator

5.4 EVALUATION OF THE STANDARDIZED LDPC CODE

This section's focus was to establish the performance of the standardized LDPC coding scheme. The parity-check matrix used in [8] was defined as $\mathcal{H}_{\text{std}}$ and the code was constructed by concatenating circulated shifted identity matrices with each other. The variable node degree distribution for $\mathcal{H}_{\text{std}}$ is given by

$$\lambda_{\text{std}}(x) = 0.458x + 0.333x^2 + 0.208x^5, \tag{5.1}$$

and the check node degree distribution for $\mathcal{H}_{\text{std}}$ is given by

$$\rho_{\text{std}}(x) = 0.667x^5 + 0.333x^6. \tag{5.2}$$

5.4.1 Performance Analysis in a Static AWGN Channel

The simulation parameters of the LDPC coded mobile WiMAX platform using $\mathcal{H}_{\text{std}}$ in a static AWGN channel are given in table 5.8. In Figure 5.7 the noise threshold effect that was expected in a LDPC code using iterative decoding was seen at 4.2 dB.

TABLE 5.8: Simulation Environment Parameters for Figure 5.7

Description	**Value**
Channel	Static AWGN
Cyclic Prefix Length	1/4
Data Modulation	4-PSK
Channel PDP	Single-tap channel

Majority of the errors were corrected in the first hundred iterations performed on the LDPC code and for a BER below 10^{-18} more than 1500 iterations were required [28]. The BER range for this dissertation only requires 1000 iterations. With a single interation a coding gain (CG) of 1.6801 dB was obtained to the uncoded mobile WiMAX system and was the same for all lengths of LDPC code proposed in the WiMAX standard. Two lengths of LDPC code was evaluated in this section with respective lengths of $n_{\mathcal{C}} = 576$ and $n_{\mathcal{C}} = 1152$. A coding gain of 7.504 dB for length $n_{\mathcal{C}} = 576$ was observed while a coding gain of 7.9114 dB for length of $n_{\mathcal{C}} = 1152$ was observed at a BER of 10^{-6}. There was a coding gain of 1.6958 dB between the standardized $1/2$-rate $n_{\mathcal{C}} = 576$ LDPC code and the NASA convolutional code at a BER of 10^{-6} presented in the mobile WiMAX standard. A higher coding gain of 2.1032 dB was measured for a $1/2$-rate $n_{\mathcal{C}} = 1152$ LDPC code[5] compared to the use of the NASA convolutional code at a BER of 10^{-6}. The optional LDPC code in the mobile WiMAX standard was a much better choice in coding scheme for a static AWGN channel.

[5] The mobile WiMAX standard supports LDPC code lengths of $n_{\mathcal{C}} \in [576, 2304]$.

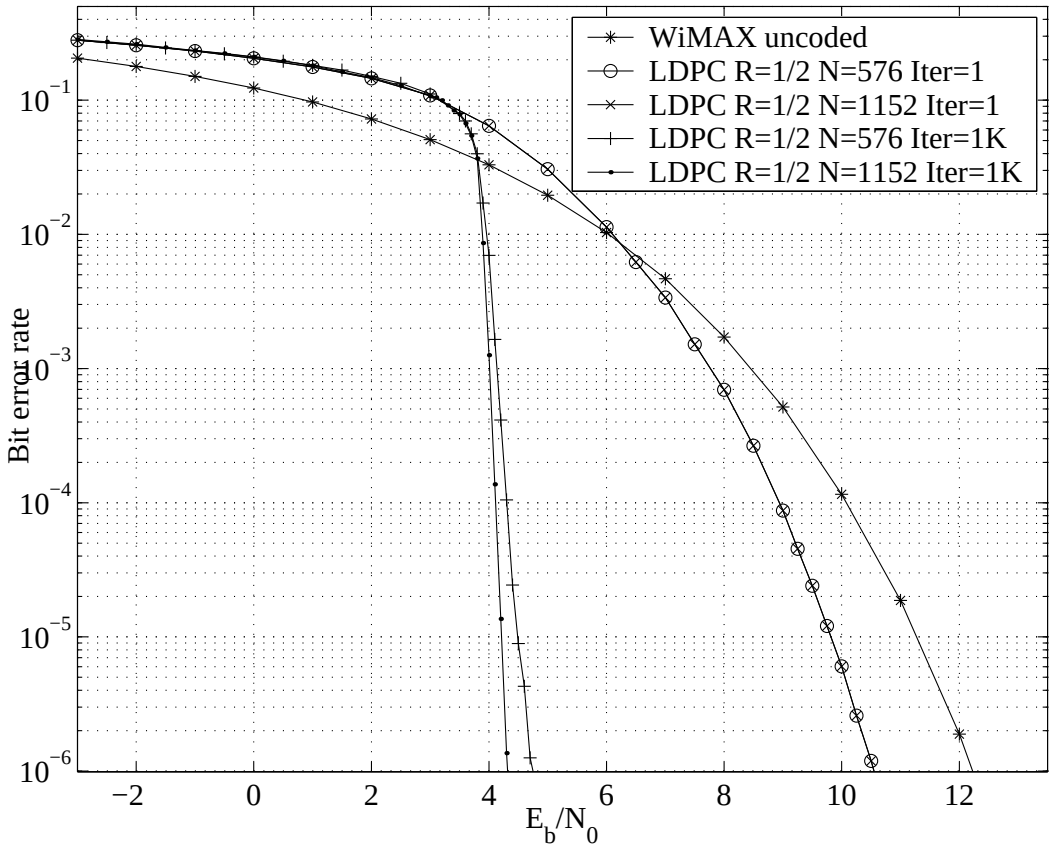

FIGURE 5.7: BER graph for LDPC coded WiMAX system in static AWGN channel.

5.4.2 Performance Analysis in a Frequency Non-Selective Fading Channel

The performance of the standardized LDPC code was analyzed in a frequency non-selective fading channel in this section and the simulation parameters are given in table 5.9. The result of the analysis showed that in Figure 5.8 a clear advantage is observed in using the LDPC code in a mobile WiMAX system. The coding gain in the evaluated range was infinite compared to the uncoded WiMAX system. It was observed that the LDPC code with length $n_{\mathcal{C}} = 576$ does not compete with the convolutional code in the observation region. By extending the length to $n_{\mathcal{C}} = 1152$ the LDPC code becomes long enough to combat the fades in a frequency non-selective fading channel and then outperforms the convolutional code.

There was no asymptotic nature between any of the BER performance graphs, but table 5.10 was compiled with coding gains for the LDPC code of length $n_{\mathcal{C}} = 1152$ and the mandatory convolutional code for a flat fading channel.

The results presented in table 5.10 shows that the LDPC code outperforms the convolutional

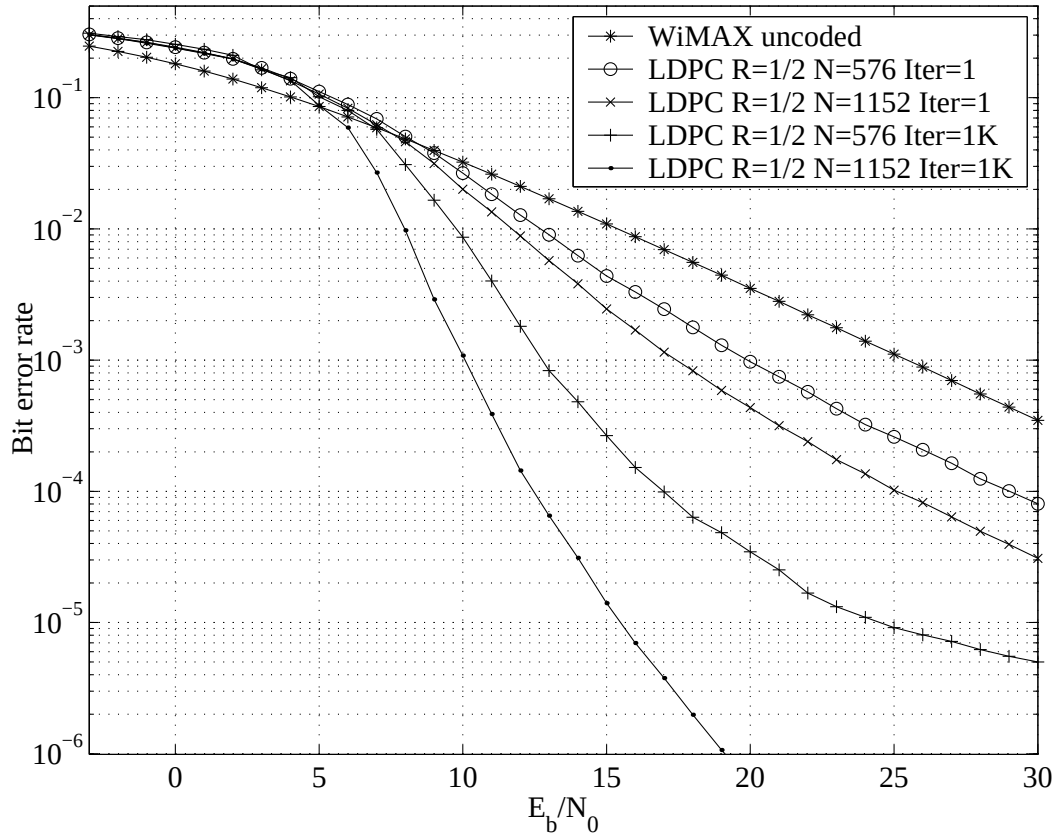

FIGURE 5.8: BER graph for a LDPC coded WiMAX system in a frequency non-selective fading channel.

TABLE 5.9: Simulation Environment Parameters for Figure 5.8

Description	**Value**
Channel	Frequency non-selective fading
Maximum Doppler Shift	104Hz
Cyclic Prefix Length	1/4
Data Modulation	4-PSK
Channel PDP	Single-tap channel

code at every BER level, except for a BER lower than 10^{-6}. Further performance improvement was expected when the codeword length grows ($n_{\mathcal{C}} > 1152$) of the LDPC code. The system complexity grows linear with the codeword length $n_{\mathcal{C}}$, making it a feasible solution. The coding gain is increased and the expected error floor is lowered when the codeword length is extended.

Table 5.10: BER comparison between the convolutional code and the standardized LDPC code

BER	Convolutional code	LDPC	Coding gain
10^{-3}	10.8893 dB	10.0781 dB	0.8112 dB
10^{-4}	13.7081 dB	12.4611 dB	1.2470 dB
10^{-5}	16.5965 dB	15.4870 dB	1.1095 dB
10^{-6}	19.6322 dB	19.1169 dB	0.5153 dB

5.4.3 Performance Analysis with a Saturated Transmission Amplifier

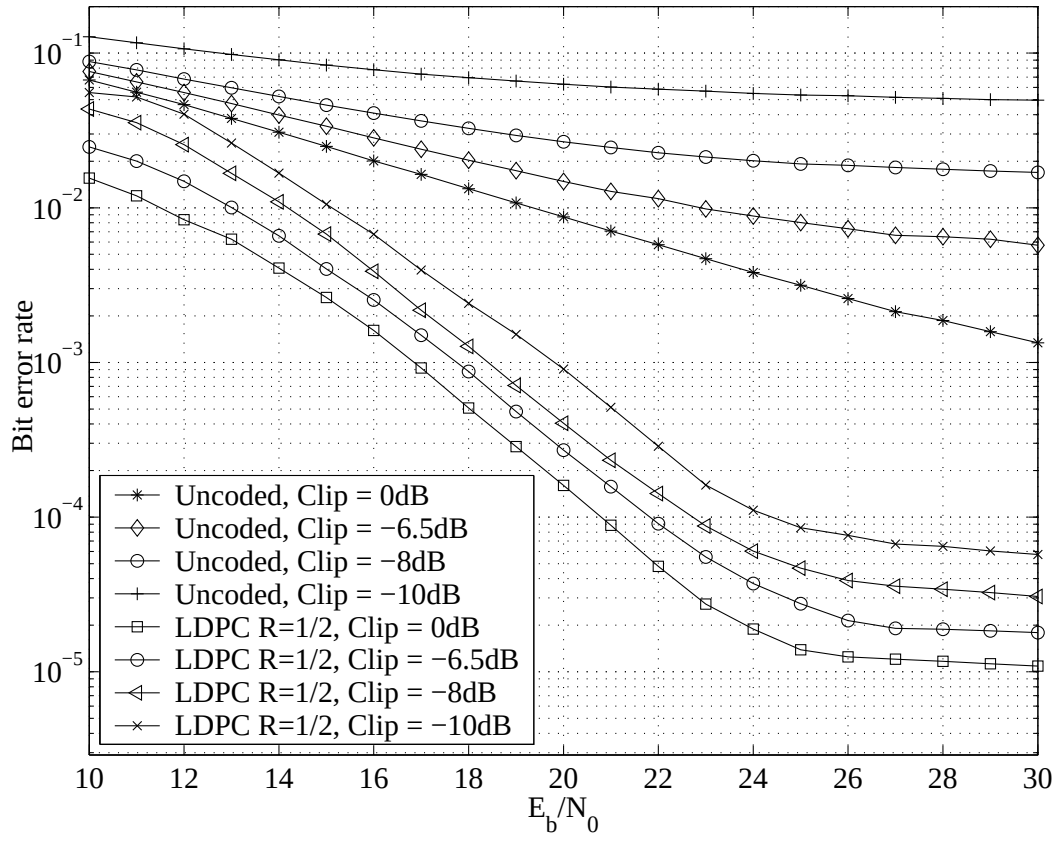

FIGURE 5.9: BER graph for a LDPC coded WiMAX system with peak clipping at the transmitter.

The next effect to evaluate was the loss in performance of the standardized LDPC code in the presence of a saturated transmission amplifier. The simulation parameters were given in table 5.11. In Figure 5.9 an infinite coding gain was observed to the uncoded WiMAX system.

The LDPC was more resilient to the effect of transmission amplifier saturation than the

TABLE 5.11: Simulation Environment Parameters for Figure 5.9

Description	**Value**
Channel	Frequency selective fading
Maximum Doppler Shift	104Hz
Cyclic Prefix Length	1/8
Data Modulation	16-QAM
Channel PDP	ITU Pedestrian-B Channel 103
Channel Estimation	Least Square Estimation
Interpolation method	Wiener Interpolator

TABLE 5.12: BER comparison of the convolutional code and standardized LDPC code

Peak clipping level	**BER**	**Convolutional code**	**Standardized LDPC**	**Coding gain**
0 dB	10^{-3}	21.1928 dB	16.8525 dB	4.3403 dB
0 dB	10^{-4}	25.6938 dB	20.7939 dB	4.8999 dB
-6.5 dB	10^{-3}	22.5355 dB	17.7499 dB	4.7856 dB
-6.5 dB	10^{-4}	28.5506 dB	21.8202 dB	6.7304 dB
-8 dB	10^{-3}	25.5598 dB	18.4102 dB	7.1496 dB
-10 dB	10^{-3}	>30 dB	19.8104 dB	>10.1896 dB

convolutional code. The disadvantage in using LDPC codes in a finite analysis of the codeword length, was that an error floor was observed in the BER graph. A codeword length of $n_{\mathcal{C}} > 10^4$ was required to reduce the error floor to a BER value of 10^{-18}. Table 5.12 with coding gains for the standardized LDPC code was compiled to illustrate the performance gains.

5.5 EVALUATION OF OPTIMIZED LDPC CODE

This section's focus was to use different degree distribution and design codes to improve performance in the current telecommunication system. The limiting factor in the construction of a code is the constraint of the short codeword length ($n_{\mathcal{C}} < 10^4$) and the design was a difficult task [28]. Long codewords ($10^6 < n_{\mathcal{C}} < 10^7$) have a low probability of producing cycles in a graph and can handle heavier degree distributions which results in improve BER performance [27]. The benchmark for the optimized design is the standardized LDPC code that was used in the mobile WiMAX (see section 5.4) standard [8]. The new codes were constructed by use of the optimized degree distributions and PEG algorithm. By observing that most designed codes follow a trend in performance (expected average ensemble's performance), there were still some good and poor codes found in the search. In the next three sections the results of the search is shown for the range of channel conditions.

5.5.1 Performance Analysis in a Static AWGN Channel

This section's results have been researched in [28] for a static AWGN channel. These optimized degree distributions were applied in the code construction in an attempt to improve on the current standardized LDPC code. This should have been a straightforward task, but due to the short length $n_{\mathcal{C}}$ of the LDPC code this proved to be a formidable task. A good LDPC code was found and the performance results were illustrated in Figure 5.10. The simulation parameters for this section are given in table 5.13 and a performance gain was observed.

TABLE 5.13: Simulation Environment Parameters for Figure 5.10

Description	**Value**
Channel	Static AWGN
Cyclic Prefix Length	1/4
Data Modulation	4-PSK
Channel PDP	Single-tap channel

A coding gain of 0.1954 dB was acquired for the shorter optimized LDPC code ($n_{\mathcal{C}} = 576$), compared to the standardized LDPC code (presented in section 5.4.1). A coding gain of 0.2106

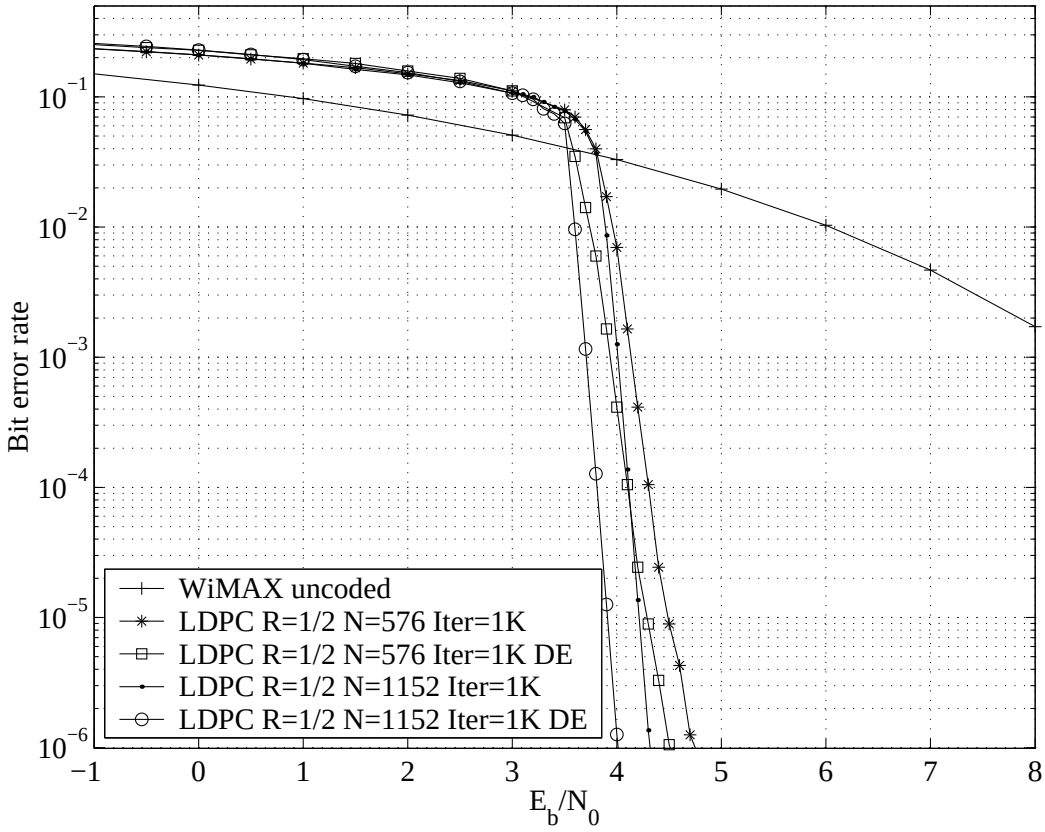

FIGURE 5.10: BER graph for a optimized LDPC (DE) coded WiMAX system in a static AWGN channel.

dB was obtained for the longer LDPC code ($n_{\mathcal{C}} = 1152$) compared to the standardized LDPC code of equivalent length. This was evident as the noise threshold for the optimized code was much lower than the noise threshold of the standardized LDPC code. This difference between the two code designs becomes more apparent as the codeword length grows ($n_{\mathcal{C}} \to \infty$) and concludes that there is room for improvement in a fixed length design of a LDPC code in a static AWGN channel.

5.5.2 Performance Analysis in a Frequency Non-Selective Fading Channel

The design of a LDPC code for a frequency non-selective fading channel has been researched in [29]. The constraint was again the short codeword length ($n_{\mathcal{C}} < 10^4$).

The problem with the degree distributions presented in [29] was that they were more dense than the degree distributions presented in [28]. The effect of heavy edge density is that the Tanner

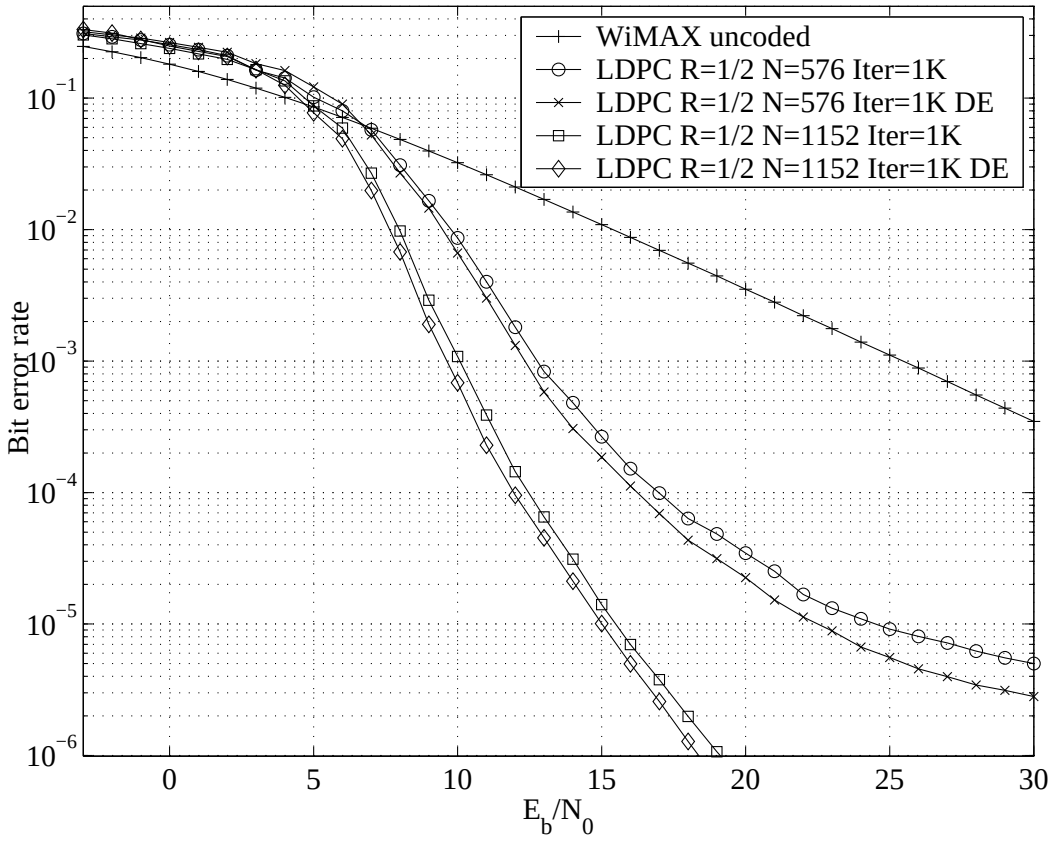

FIGURE 5.11: BER graph for a optimized LDPC (DE) coded WiMAX system in a frequency non-selective fading channel.

graph is not sparse[6] if $n_{\mathcal{C}}$ is not long enough.

Definition 5.5.1 *The number of edges E is given by [28]*

$$E = \frac{n_{\mathcal{C}}}{\int_0^1 \lambda(x)dx}. \tag{5.3}$$

When code construction was initiated many more rules were followed for cycle elimination and code construction proved to be more difficult. The simulation parameters are given in table 5.14 and the results of the optimized LDPC code are given in Figure 5.11.

The shorter LDPC code ($n_{\mathcal{C}} = 576$) presented a coding gain of 0.4292 dB compared to the standardized LDPC code and a coding gain of 0.5146 dB was observed for the longer LDPC code ($n_{\mathcal{C}} = 1152$). This observation was expected in the numerical analysis when the length of the codeword was increased to converges to the expected code ensemble's performance and corresponding noise threshold.

[6] High edge density with a short $n_{\mathcal{C}}$ results in high number of cycles that can't be eliminated.

TABLE 5.14: Simulation Environment Parameters for Figure 5.11

Description	**Value**
Channel	Frequency non-selective fading
Maximum Doppler Shift	104Hz
Cyclic Prefix Length	1/4
Data Modulation	4-PSK
Channel PDP	Single-tap channel

5.5.3 Performance Analysis with a Saturated Transmission Amplifier

This section shows the results of the contribution made in this dissertation. Effort has been made to bring the correlation down of the data in the subcarriers in an OFDM symbol, but unfortunately most methods requires an increase in network overhead. The idea was to assign data symbols to an OFDM symbol which have low correlation but required major network overhead to control placing within symbols. In this dissertation an alternative approach is presented in which a Tanner graph is used which exploits the nature of the communication system and attempt to optimize it by training with a given degree distribution.

TABLE 5.15: Simulation Environment Parameters for Figure 5.12

Description	**Value**
Channel	Frequency selective fading
Maximum Doppler Shift	104Hz
Cyclic Prefix Length	1/8
Data Modulation	16-QAM
Channel PDP	ITU Pedestrian-B Channel 103
Channel Estimation	Least Square Estimation
Interpolation method	Wiener Interpolator

Numerical analysis was done in section 4.10 and shows that information data transmitted

through a mobile channel still retains it original probability distribution even with an saturated amplifier. The only change was the variance was increased as more peak clipping was applied at the transmitter. In terms of a Tanner graph, only the noise threshold shifts accordingly and almost 10 dB of peak clipping can be applied while maintaining an operable communication system using an 128-FFT OFDM symbol.

This approach is more desirable due to the zero network overhead and proposed the use of coding theory as an alternative method for reducing the effects of peak clipping induced by the transmitter. A comparison of the optimized LDPC code was made to the existing optional LDPC code present in the mobile WiMAX system [8] in Figure 5.12.

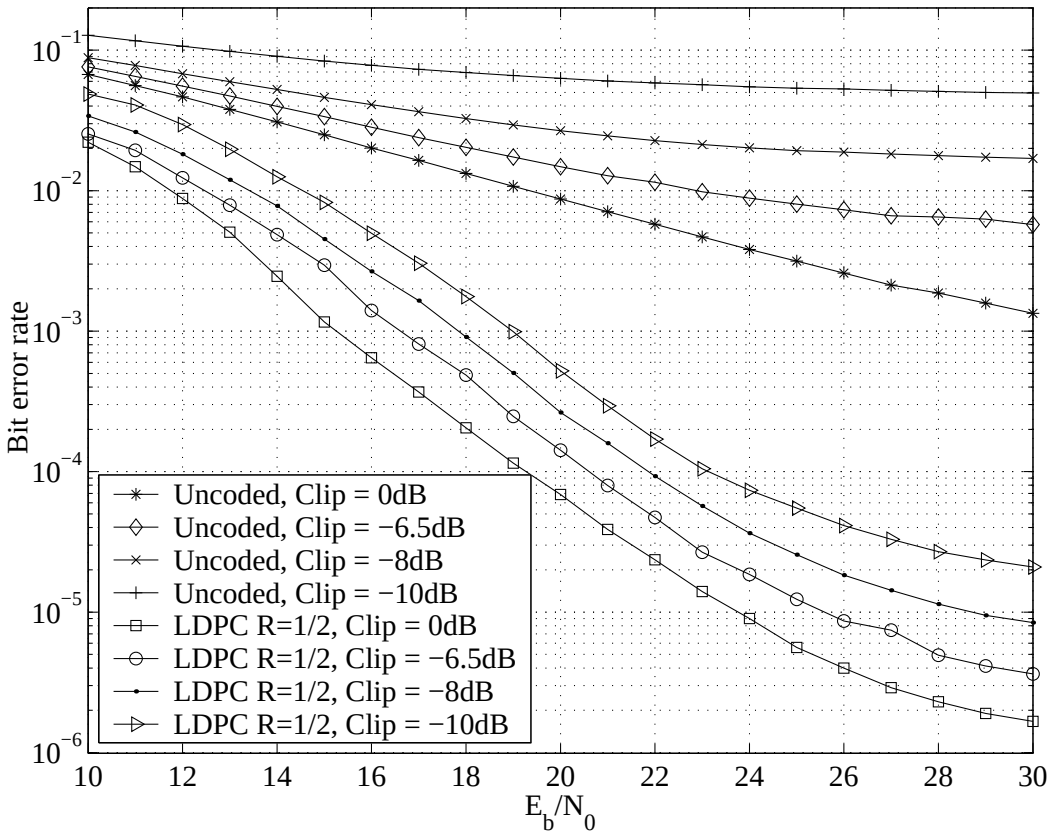

FIGURE 5.12: BER graph for a optimized LDPC (DE) coded WiMAX system with peak clipping at the transmitter.

Table 5.16 was compiled to show the performance improvement when using optimized LDPC code to combat the peak clipping levels induced by the transmitter.

These results indicate that the use of LDPC codes should rather be the mandatory coding scheme of choice in a frequency selective fading channel with peak clipping induced by the transmitter.

TABLE 5.16: BER comparison of an optimized LDPC code to the standardized LDPC code

Peak clipping level	**Coding gain**	**LDPC** $\mathcal{H}_{\text{std}}$ Error Floor	**LDPC** $\mathcal{H}_{\text{opt}}$ Error Floor
0 dB	1.5985 dB	$1.08725 \cdot 10^{-5}$	$1.6701 \cdot 10^{-6}$
-6.5 dB	1.1339 dB	$1.79023 \cdot 10^{-5}$	$3.63356 \cdot 10^{-6}$
-8 dB	0.8698 dB	$3.07068 \cdot 10^{-5}$	$8.43122 \cdot 10^{-6}$
-10 dB	0.8278 dB	$5.7298 \cdot 10^{-5}$	$2.09536 \cdot 10^{-5}$

The performance of LDPC code was good in a realistic channel model with an OFDM symbol that was peak clipped near the average transmission symbol power. The error floor will always be present when using a LDPC code and this can be compensated by the system designer by adjusting the link budget [1] accordingly in the communication link.

CHAPTER SIX
CONCLUSION

6.1 CHAPTER OVERVIEW

The conclusions and remarks from this dissertation are discussed in detail in this chapter. This chapter concludes with future research prospects that emanate from this dissertation.

6.2 REMARKS ON CODING SCHEMES USED IN THIS DISSERTATION

In this dissertation, a study was conducted on the feasibility and efficiency of the use of a LDPC code in a wireless communication system. The coding schemes were evaluated on a mobile WiMAX platform with channel conditions ranging from a static AWGN channel to a frequency selective fading channel with a saturated amplifier at the transmitter. The LDPC code was optimized for each of these channel conditions presented in this dissertation.

6.2.1 Remarks on the use of Convolutional Codes

The convolutional code [8], which has been researched over the last 30 years, was included in this dissertation solely as a performance benchmark for other coding schemes. The NASA convolutional code[1] was implemented to support any remarks pertaining to the performance of other coding schemes. The remarks on the use of a convolutional code are:

[1] Mandatory coding scheme in mobile WiMAX [8]

- The performance of the convolutional code is demonstrated in the design and the constraint length $\mathcal{K}$ of the encoder. The complexity of the convolutional encoding is low and the convolutional code was optimized through numerical searches in a finite space [30].

- A disadvantage for a convolutional code is that the decoding computation complexity grows exponentially while the constraint length grows only linearly in the channel encoder even when applying trellis expurgation [40].

- Good performance results were obtained by using a convolutional code in a frequency non-selective fading channel, but an operable state could only be achieved with an interleaver. Perfect CSI was required to enhance the performance of the convolutional code in order to compete against the LDPC code.

- A poor BER was observed with a convolutional code in a frequency selective fading channel when the transmitter's amplifier saturates the OFDM symbols. The BER performance could be improved when multiple codewords were interleaved over multiple transmission bursts to the subscriber station, but this was a daunting task to control the sequences over the network and to keep the latency low when using the multiple access scheme.

- The last drawback when using a convolutional code is the limitation in the length of the data packet. When longer data packets are generated, as demand increases, the convolutional coding scheme does not offer much improvement[2]. The alternative was to subdivide the packet into smaller packets to reduce the complexity of the channel decoder followed by interleaving all the packets, but the performance gain will only be minimal and limited.

6.2.2 Remarks on the Standardization of LDPC Codes

LDPC codes were first introduced by Gallager [16] in 1963, but unfortunately in that era the technology for applying very large sparse matrices was not feasible and interest was lost in the method. LDPC codes were revisited in 1999 [19] and standardized in the mobile WiMAX standard [8]. The following conclusions relating to the LDPC code used in the mobile WiMAX standard were made through this dissertation.

[2] The performance of a convolutional code is proportional to the number of memory registers in the encoder.

- The advantage of a LDPC code is that a parity-check matrix $\mathcal{H}$ can be tailor made for most channel conditions. The problem was in obtaining a generator matrix for the encoding process as well as the search for an effective generator matrix for a given parity-check matrix, this is an ongoing research topic. The mobile WiMAX standard employs a circular shifted generator matrix that enables the transmitter to encode the information stream with low latency. In summary, the standardized LDPC code was optimized for encoding and not for the channel conditions.

- The standardized LDPC code was found to be superior in performance to the convolutional code in a static AWGN channel, which was seen when the noise threshold was reached and the decoder could iterate the received sequence to have zero errors.

- Good BER performance was observed when using the standardized LDPC code in a frequency non-selective fading channel provided that the length of the code was at least $n_{\mathcal{C}} > 1000$ in order to outperform the convolutional code. This concludes that better BER performances can be obtained from a longer LDPC codeword length $n_{\mathcal{C}}$. The LDPC outperforms the convolutional code without any CSI.

- The standardized LDPC code illustrates that a sparse graph code is a method for improving BER performance in a communication system with amplifier saturation of an OFDM symbol at the transmitter. By adjusting the peak clipping levels, a desired BER performance can be obtained when the link budget includes the noise threshold of the LDPC.

6.2.3 Remarks on Optimizing LDPC Codes

The LDPC code was accepted as an optional coding scheme in the mobile WiMAX standard [8] and was optimized for the encoding at the transmitter with a short codeword length $n_{\mathcal{C}}$. The short length of the codeword was a significant impairment on the overall BER performance. Near capacity performing LDPC codes have been designed [28, 29] under the assumption that the codeword length was longer than 10^6. In this dissertation a search for good LDPC codes was found for codeword lengths of $n_{\mathcal{C}} < 10^4$ and was verified as in chapter 5.

- *Density evolution* was used to analyze the progress of the messages passed within the belief propagation decoder in order to optimize the graph code. The graph code was

optimized for the entropy [73] that the messages induce from a clipped OFDM modulated sequence and communication channel.

- These optimized graph codes were simulated on the mobile WiMAX platform to verify any performance gains. Performance improvements have been found for both the static AWGN channel and the frequency non-selective fading channel.

- It was shown that a graph code can be optimized for clipped OFDM symbols in a frequency selective fading channel. This decreased the overall link budget required for the system and lowers the error floor by a factor of 10.

6.3 FUTURE RECOMMENDATIONS AND RESEARCH

Some prospective research endeavours are listed below that can be performed on the mobile WiMAX with a short description of each.

- The mobile WiMAX platform can be expanded by means of MIMO capabilities that can be used for space-time-frequency diversity. From this a range of numerical analysis can be performed and the LDPC code can be optimized for this communication system.

- A current research field is to expand the density evolution method in order to analyze message passing algorithms in a Galois Field (GF) as well as the stability issues that arise in the use of this method.

- A thorough analysis of current source encoding techniques and their application in the mobile WiMAX standard.

- Higher network layer control can be implemented for adaptive modulation schemes and adaptive pilot modulation which can be used to optimize network utilization.

6.4 CONCLUSION

In this dissertation several coding schemes were analyzed on a mobile WiMAX platform which was developed as part of this dissertation. The mobile WiMAX and channel characteristics of interest in this dissertation were discussed in chapter 2. In chapter 2 the advantages and disadvantages of using the OFDM modulation as the access scheme in mobile WiMAX was

discussed. Emphasis was placed on the performance degradation that amplifier saturation has on an OFDM symbol and the limitations it presents on the mobile WiMAX system.

The mandatory convolutional coding scheme in mobile WiMAX [8] was implemented in this dissertation as a benchmark for other coding schemes. A cross road has been reached in the technology used in mobile WiMAX as most coding schemes[3] have started reaching their practical limits. Most of these codes were not feasible to improve the BER performance and were limited by the complexity of the decoder or by the limited provided error control capabilities. The contradiction was that the payload size was to short for the more powerful coding schemes[4] which thrives on long codeword lengths.

A performance evaluation was conducted on the standardized LDPC code used in the mobile WiMAX platform and it outperform the mandatory coding scheme. By means of the numerical analysis on the channel messages received at the Belief propagation decoder, a LDPC code was designed through graph analysis to compensate for the channel condition and amplifier impairments. This optimized LDPC code was compared on the mobile WiMAX platform to the other coding schemes and was found to have the best BER performance in all the channel conditions. LDPC codes will become more popular as the available payload size in the communication system becomes longer[5].

[3] Convolutional code, Reed Solomon code, Hamming code, Golay code, etc.
[4] LDPC code and Turbo code
[5] Typical codeword lengths of $n_{\mathcal{C}} > 10^4$

REFERENCES

[1] T. Rappaport, *Wireless communications, principles and practice*, 2nd ed. Upper Saddle River: Prentice Hall, 2002.

[2] C. Shannon, "A Mathematical theory of communications," *Bell Systems Technical Journal*, vol. 27, pp. 379–423 and 623–656, July and October 1948.

[3] R. Hamming, "Error detecting and error correcting codes," *Bell Systems Technical Journal*, vol. 29, no. 2, pp. 147–160, April 1950.

[4] M. Golay, "Notes on digital coding," *Proceedings on IRI(IEEE)*, vol. 37, p. 657, June 1949.

[5] R. Morelos-Zaragoza, *The art of error correcting coding*, 1st ed. The Atrium, Chichester: John Wiley and Sons, 2002.

[6] P. Elias, "Coding for noisy channels," *Institute of Radio Engineers Convention Record*, vol. 4, pp. 37–46, September 1955.

[7] A. Viterbi, "Error bounds for convolutional codes and an asymptotically optimum decoding algorithm," *IEEE Transactions on Information Theory*, vol. IT-13, no. 2, pp. 260–269, April 1967.

[8] *Air Interface for Fixed and Mobile Broadband Wireless Access Systems*, IEEE Amendment and Corrigendum to IEEE Std. 802.16-2004 802.16e-2005 Std. 802.16, 2005.

[9] *Air Interface for Fixed Broadband Wireless Access Systems*, IEEE Revision of IEEE Std. 802.16-2001 Std. 802.16, 2004.

[10] *Wireless LAN Medium Access Control (MAC) and Physical Layer (PHY) Specification*, IEEE Std. 802.11, 1997.

[11] I. Reed and G. Solomon, "Polynomial codes over certain finite fields," *Society for Industrial Applied Mathematics Journal*, vol. 8, no. 2, pp. 300–304, June 1960.

[12] R. Blahut, *Theory and Practice of error control codes*, 1st ed. Reading, Massachusetts: Addison-Wesley, 1983.

[13] G. Forney, "On decoding BCH codes," *IEEE Transactions on Information Theory*, vol. IT-11, no. 4, pp. 549–557, October 1965.

[14] J. Massey, "Step-by-step decoding of the BCH codes," *IEEE Transactions on Information Theory*, vol. IT-11, no. 4, pp. 580–585, October 1965.

[15] B. Sklar, *Digital Communications: Fundamentals and Applications*, 2nd ed. Prentice Hall, January 2001.

[16] R. Gallager, "Low-density parity-check codes," Ph.D. dissertation, MIT Press, Cambridge, MA, 1963.

[17] R. Urbanke and T. Richardson, "Efficient encoding of low-density parity-check codes," *IEEE Transactions on Information Theory*, vol. 47, no. 2, pp. 638–656, February 2001.

[18] T. Richardson and R. Urbanke, "The renaissance of Gallager's low-density parity-check codes," *IEEE Communications Magazine*, vol. 41, no. 8, pp. 126–131, August 2003.

[19] D. MacKay, "Good error correcting codes based on very sparse matrices," *IEEE Transactions on Information Theory*, vol. 45, no. 2, pp. 399–431, March 1999.

[20] G. Ungerboeck, "Channel coding with multilevel/ phase signaling," *IEEE Transactions on Information Theory*, vol. IT-25, no. 1, pp. 55–67, January 1982.

[21] C. Berrou, A. Glavieux, and P. Thitimajshima, "Near Shannon limit error-correcting coding and decoding: Turbo-codes," in *Proceedings of IEEE International Conference on Communications*, vol. 2, Geneva, Switzerland, May 1993, pp. 1064–1070.

[22] J. Yedidia, W. Freeman, and Y. Weiss, "Understanding Belief Propagation and its generalizations," Mitsubishi Electric Research Laboratories, 201 Broadway, Cambridge, Massachusetts 02139, Tech. Rep. TR-2001-22, January 2002.

[23] R. McEliece, D. MacKay, and J. Cheng, "Turbo decoding as an instance of Pearl's belief propagation algortihm," *IEEE Journal on Selected Areas of Communication*, vol. 16, no. 2, pp. 140–152, February 1998.

[24] J. Pearl, *Probabilistic Reasoning in Intelligent Systems*, 2nd ed. San Francisco, CA: Kauffmann, 1988.

[25] D. MacKay and R. Neal, "Near Shannon limit performance of low density parity check codes," *Electronics Letters*, vol. 32, no. 18, pp. 1645–1646, August 1996.

[26] S. Chung, G. Forney, T. Richardson, and R. Urbanke, "On the design of low-density parity-check codes within 0.0045dB of the shannon limit," *IEEE Communications Letters*, vol. 5, no. 2, pp. 58–60, February 2001.

[27] T. Richardson and R. Urbanke, "The capacity of low-density parity-check codes under message-passing decoding," *IEEE Transactions on Information Theory*, vol. 47, no. 2, pp. 599–618, February 2001.

[28] T. Richardson, M. Shokrollahi, and R. Urbanke, "Design of capacity-approaching irregular low-density parity-check codes," *IEEE Transactions on Information Theory*, vol. 47, no. 2, pp. 619–637, February 2001.

[29] J. Hou, P. Siegel, and L. Milstein, "Performance analysis and code optimization of low-density parity-check codes on Rayleigh fading channels," *IEEE Journal on Selected Areas of Communication*, vol. 19, no. 5, pp. 924–934, May 2001.

[30] J. Proakis, *Digital communication*, 4th ed. New York: McGraw-Hill, 2001.

[31] A. Salvekar *et al.*, "Multiple-antenna technology in WiMAX systems," *Intel Technology Journal*, vol. 8, no. 3, pp. 229–239, 2004.

[32] E. Agis *et al.*, "Global interoperable broadband wireless networks: Extending WiMAX technology to mobility," *Intel Technology Journal*, vol. 8, no. 3, pp. 173–187, 2004.

[33] K. Jeong, S. Kim, K. Chung, J. Kim, and J. Y. J. L. S. Seo, "Multipath channel models for wireless local and metropolitan area networks," in *International Conference on Information Technology and Applications, ICITA '05*, vol. 2, Sydney, Australia, July 2005, pp. 295–298.

[34] J. Parsons, *The mobile radio propagation channel*, 2nd ed. New York: Wiley, 2000.

[35] J. Seybold, *Introduction to RF propagation*, 1st ed. New Jersey: Wiley, 2005.

[36] G. Hufford, A. Longley, and W. Kissick, "A guide to the use of the ITS irregular terrain model in the area prediction mode," *Technical Report National Telecommunications and Information Administration (NTIA) Report pp. 82-100. (NTIS Order No. PB82-217977)*, 1982.

[37] G. Hufford, "The ITS irregular terrain model," Tech. Rep. version 1.2.2, the algorithm, 1995.

[38] W. Kleynhans, "On channel estimation for mobile WiMAX," Master's thesis, University of Pretoria, South Africa, 2007.

[39] J. Proakis and M. Salehi, *Communication system engineering*, 2nd ed. Upper Saddle River: Prentice Hall, 2002.

[40] L. Staphorst, "Viterbi decoded linear block codes for narrowband and wideband wireless communication over mobile fading channels," Master's thesis, University of Pretoria, South Africa, 2005.

[41] H. Steendam and M. Moeneclaey, "Analysis and optimization of the performance of OFDM on frequency-selective time-selective fading channels," *IEEE Transactions on Communications*, vol. 47, no. 12, pp. 1811–1819, December 1999.

[42] B. Sklar, "Rayleigh fading channels in mobile digital communication systems .i. Characterization," *IEEE Communications Magazine*, vol. 35, no. 7, pp. 90–100, July 1997.

[43] W. Lee, *Mobile cellular telecommunications systems*. New York: McGraw Hill Publication, 1989.

[44] R. Ertel and J. Reed, "Angle and time of arrival statistics for circular and elliptical scattering models," *IEEE Journal on Selected Areas of Communication*, vol. 17, no. 11, pp. 1829–1840, November 1999.

[45] H. Yagoobi, "Scalable OFDMA Physical layer in IEEE 802.16 WirelessMAN," *Intel Technology Journal*, vol. 8, no. 3, pp. 201–212, August 2004.

[46] Y. Leiba, Y. Segal, Z. Hadad, and I. Kitroser, "Coverage/capacity simulations for OFDMA PHY in ITU-T channel model including MRC, STC, AAS results," *Runcom Ltd., Hachoma 2 St. 75655, Technical Report IEEE C802.16e-04/16*, November 2004.

[47] S. Mitra, *Digital signal processing, a computer-based approach*, 2nd ed. New York: McGraw-Hill, 1998.

[48] G. Carlson, *Signal and linear system analysis*, 2nd ed. New York: John Wiley and Sons, 1998.

[49] L. Cimini, "Analysis and simulation of digital mobile channel using orthogonal frequency division multiplexing," *IEEE Transactions on Communications*, vol. 33, no. 7, pp. 665–675, July 1985.

[50] X. Li and L. Cimini, "Effects of clipping and filtering on the performance of OFDM," *IEEE Communications Letters*, vol. 2, no. 5, pp. 131–133, May 1998.

[51] R. Soriano, "The effect of signal distortion techniques for PAPR reduction on the BER performance of LDPC and turbo coded OFDM system," in *TENCON 2006. 2006 IEEE Region 10 Conference*, no. 2, Hong Kong, China, November 2006, pp. 1–4.

[52] B. Widrow and S. Stearns, *Adaptive signal processing*, 1st ed. New Jersey: Prentice-Hall, 1985.

[53] G. Marsagalia and T. Bray, "A convenient method for generating normal variables," *Society for Industrial Applied Mathematics Journal*, vol. 6, pp. 260–264, 1964.

[54] R. Coates, G. Janacek, and K. Lever, "Monte carlo simulation and random number generation," *IEEE Journal on Selected Areas of Communication*, vol. 6, no. 1, pp. 58–66, January 1988.

[55] B. Wichmann and D. Hill, "Building a random-number generator," *Byte Magazine*, pp. 127–128, 1987.

[56] S. Haykin, *Communications Systems*, 3rd ed. New York: John Wiley and Sons, 1994.

[57] A. M. Donald and J. Olivier, "A comparative study of deterministic and stochastic sum-of-sinusoids models of Rayleigh-fading wireless channels," in *Proceedings of IEEE Wireless Communication Networking Conference (WCNC)'2007*, vol. 1, Hong Kong, China, March 2007, pp. 2027–2031.

[58] C. Patel, G. Stuber, and T. Pratt, "Comparative analysis of statistical models for the simulation of Rayleigh faded cellular channels," *IEEE Transactions on Communications*, vol. 53, no. 6, pp. 1017–1026, June 2005.

[59] R. Clarke, "A statistical theory of mobile-radio reception," *Bell Systems Technical Journal*, vol. 47, pp. 957–1000, July 1968.

[60] W. Jakes, *Microwave mobile communications*, 2nd ed. Wiley, 1974, reprinted by IEEE Press in 1994.

[61] Y. Zheng and C. Xiao, "Improved models for the generation of multiple uncorrelated Rayleigh fading waveforms," *IEEE Communications Letters*, vol. 6, no. 6, pp. 256–258, June 2002.

[62] P. Chen and H. Kobayashi, "Maximum likelihood channel estimation and signal detection for OFDM systems," in *Proceedings of IEEE International Conference Communication (ICC)*, vol. 3, New York, USA, April 2002, pp. 1640–1645.

[63] B. Bisla, R. Eline, and L. Franca-Neto, "RF System and circuit challenges for WiMAX," *Intel Technology Journal*, vol. 8, no. 3, pp. 189–200, August 2004.

[64] T. Richardson and R. Urbanke, *Modern coding theory*, 1st ed. New York: Cambridge University Press, 2008.

[65] J. Wakerly, *Digital design, principles and practices*, 3rd ed. Upper Saddle River: Prentice Hall, 2000.

[66] J. Ramsey, "Realization of optimum interleavers," *IEEE Transactions on Information Theory*, vol. IT-16, no. 3, pp. 338–345, May 1970.

[67] G. Forney, "Burst correcting codes for the classic bursty channel," *IEEE Transactions on Communication Techology*, vol. COM-19, no. 5, pp. 272–281, October 1971.

[68] D. Forney, "The Viterbi algorithm," *Proceedings of the IEEE*, vol. 61, no. 3, pp. 268–278, March 1973.

[69] J. Heller, "Short constraint length convolutional codes," Jet Propulsion Laboratory, California Institute of Technology, Pasadena, CA, Space Program Summary , pp. 171-174, December 1968.

[70] J. Heiskala and J. Terry, *OFDM Wireless LANs: A Theoretical and Practical Guide*. Indianapolis: Sams, 2001.

[71] R. Johannesson and K. Zigangirov, *Fundamentals of Convolutional Coding*. Piscataway: IEEE Press, February 1999.

[72] T. May, H. Rohling, and V. Engels, "Performance analysis of Viterbi decoding for 64-DAPSK and 64-QAM modulated OFDM signals," *IEEE Transactions on Communications*, vol. 46, no. 2, pp. 182–190, February 1998.

[73] S. ten Brink, "Convergence of iterative decoding," *Electronics Letters*, vol. 35, no. 10, pp. 806–808, May 1999.

[74] J. Moura, J. Lu, and H. Zhang, "Structured Low-Density Parity-Check codes, methods to design regular LDPC codes with large girth," *IEEE Signal Processing Magazine*, vol. 21, no. 1, pp. 42–55, January 2004.

[75] F. Beichelt and L. Fatti, *Stochastic Processes and their Applications*, 1st ed. Boca Raton: CRC Press, 2002.

[76] H. Loeliger, "An introduction to factor graphs," *IEEE Signal Processing Magazine*, vol. 21, no. 1, pp. 28–41, January 2004.

[77] F. Kschinchang, B. Frey, and H. Loeliger, "Factor graphs and the Sum-Product algorithm," *IEEE Transactions on Information Theory*, vol. 47, no. 2, pp. 498–519, February 2001.

[78] R. Tanner, "A recursive approach to low complexity codes," *IEEE Transactions on Information Theory*, vol. IT-27, no. 5, pp. 533–547, September 1981.

[79] M. Luby, M. Mitzenmacher, A. Shokrollahi, and D. Spielman, "Analysis of low density codes and improved design using irregular graphs," in *Proceedings of the 30th Annual ACM Symposium on Theory of Computing*, Dallas, Texas, USA, 1998, pp. 249–258.

[80] M. Luby, A. Shokrollahi, D. Spielman, and M. Mitzenmacher, "Improved low-density parity-check codes using irregular graphs and belief propagation," *presented at the 1998 International Symposium on Information Theory, ISIT98, Cambridge, MA*, August 1998.

[81] J. Yedidia, W. Freeman, and Y. Weiss, "Understanding Belief Propagation and its generalization," Mitsubishi Electric Research Laboratories, 201 Broadway, Cambridge, Massachusetts 02139, Tech. Rep. TR-2001-22, January 2002.

[82] H. Loeliger, J. Dauwels, J. Hu, S. Korl, L. Ping, and F. Kschinchang, "The Factor graph approach to Model-based Signal processing," *Proceedings of IEEE*, vol. 95, no. 6, pp. 1295–1322, June 2007.

[83] J. Chen and M. Fossorier, "Near optimum universal belief propagation based decoding of low-density parity check codes," *IEEE Transactions on Communications*, vol. 50, no. 3, pp. 406–414, March 2002.

[84] S. Howard, V. Gaudet, and C. Schlegel, "Soft-bit decoding of regular low-density parity check codes," *IEEE Transactions on Circuit and Systems*, vol. 52, no. 10, pp. 646–650, October 2005.

[85] B. Salmon and J. Olivier, "Performance analysis of low-density parity-check codes on a WiMAX platform," in *Proceedings of IEEE Wireless Communication Networking Conference (WCNC)'2007*, vol. 1, Hong Kong, China, March 2007, pp. 569–571.

[86] R. Storn and K. Price, "Differential evolution - A simple and efficient heuristic adaptive scheme for global optimization over continuous spaces," *Journal of Global Optimization*, vol. 11, no. 4, pp. 341–359, December 1997.

[87] S. Chung, R. Urbanke, and T. Richardson, "Gaussian approximation for sum-product decoding of low-density parity-check codes," *IEEE Transactions on Information Theory*, vol. 47, no. 2, pp. 657–670, February 2001.

[88] S.-Y. Chung, R. Urbanke, and T. Richardson, "Gaussian approximation for sum-product decoding of low-density parity-check codes," in *Proceedings of IEEE International Symposium on Information Theory, ISIT2000*, Sorrento, June 2000, p. 318.

[89] H. Jin and T. Richardson, "Block error iterative decoding capacity for LDPC codes," in *International Symposium on Information Theory 2005, ISIT2005*, Adelaide, Australia, September 2005, pp. 52–56.

[90] J. Fan and Y. Xiao, "A method of counting the number of cycles in LDPC codes," in *8th International Conference on Signal Processing, ICSP 2006*, vol. 3, Budapest, Hungary, May 2006, pp. 16–20.

[91] T. Halford, "An algorithm for counting short cycles in bipartite graphs," *IEEE Transactions on Information Theory*, vol. 52, no. 1, pp. 287–292, January 2006.

[92] X. Hu, D. Arnold, and E. Eleftheriou, "Progressive edge-growth Tanner graphs," in *Proceedings of IEEE GLOBECOM'2001*, vol. 2, San Antonio, Texas, USA, November 2001, pp. 995–1001.

[93] X. Hu, E. Eleftheriou, and D. Arnold, "Regular and irregular Progressive Edge-Growth Tanner graphs," *IEEE Transactions on Information Theory*, vol. 51, no. 1, pp. 386–398, January 2005.

[94] T. Tian, C. Jones, J. Villasenor, and R. Wesel, "Construction of irregular LDPC codes with low error floors," in *Proceedings of IEEE International Conference Communication (ICC)'2003*, vol. 5, Anchorage, Alaska, USA, May 2003, pp. 3125–3129.

[95] H. Xiao and A. Banihashemi, "Improved Progressive-Edge-Growth (PEG) construction of irregular LDPC codes," *IEEE Communications Letters*, vol. 8, no. 12, pp. 715–717, December 2004.

[96] T. Etzion, A. Trachtenberg, and A. Vardy, "Which codes have cycle-free Tanner graphs," *IEEE Transactions on Information Theory*, vol. 45, no. 6, pp. 2173–2181, September 1999.

[97] M. Yazdani, S. Hemati, and A. Banihashemi, "Improving Belief Propagation on graphs with cycles," *IEEE Communications Letters*, vol. 8, no. 1, pp. 57–59, January 2004.

[98] K. Chung and J. Heo, "Improved Belief Propagation (BP) decoding for LDPC codes with a large number of short cycles," in *Proceedings of IEEE Vechicular Technology Conference (VTC), 2006*, vol. 3, Melbourne, Australia, May 2006, pp. 1464–1466.

[99] X. Yan and I. Fair, "Error-control selective mapping coding for PAPR reduction in OFDM systems," in *IEEE Vehicular Technology Conference, 2004*, vol. 1, Los Angeles, CA, September 2004, pp. 583–587.

[100] O. Muta and Y. Akaiwa, "Peak power reduction method based on structure of parity-check matrix for LDPC coded OFDM transmission," in *IEEE Vehicular Technology Conference, 2007*, Dublin, Ireland, April 2007, pp. 2841–2845.

[101] L. Staphorst and L. Linde, "Performance evaluation of Viterbi decoded Reed Solomon block codes in additive white Gaussian noise and flat fading channel conditions," in *Proceedings of IEEE Wireless Communication Networking Conference (WCNC)'2002*, vol. 2, Orlando, Florida, March 2002, pp. 675–681.

[102] E. Frontana and I. Fair, "Avoiding PAPR degradation in convolutional coded OFDM signals," in *Proceedings of IEEE Communications, Computers and Signal Processing Conference (PacRim)'2007*, vol. 1, University of Victoria, Victoria, B.C., Canada, August 2007, pp. 312–315.

[103] L. Sichao and Y. Dongfeng, "Reducing PAPR of OFDM wih convolutional code and 8-ASK mapping," in *Proceedings of IEEE Wireless Communications, Networking and Mobile Computing Conference (WCNM)'2005*, vol. 1, Wuhan, China, September 2005, pp. 253–256.

[104] M. Chen and O. Collins, "Trellis pruning for peak-to-average power ratio reduction," in *Proceedings of IEEE International Symposium on Information Theory (ISIT)'2005*, vol. 1, Adelaide, Australia, September 2005, pp. 1261–1265.

[105] S. Sumathi, "Peak to average power ratio reduction of OFDM signal," in *Proceedings of IEEE INDICON'2005*, vol. 1, Chennai, India, December 2005, pp. 241–244.

[106] L. Perez and D. Costello. (1993) A simulation study of the performance of the nasa (2,1,6) convolutional code on RFI/burst channels. [Online]. Available: http://www.sti.nasa.gov/STI-public-homepage.html. Last visited: November 2007

[107] A. Viterbi, J. Wolf, E. Zehavi, and R. Padovani, "A pragmatic approach to trellis-coded modulation," *IEEE Communications Magazine*, vol. 27, no. 7, pp. 11–19, July 1989.

[108] J. Wolf and E. Zehavi, "P2 codes: Pragmatic trellis codes utilizing punctured convolutional codes," *IEEE Communications Magazine*, vol. 33, no. 2, pp. 94–99, February 1995.

[109] J. Stewart, *Calculus Early Transcendentals*, 4th ed. Pacific Grove: Brooks and Cole, 1999.

APPENDIX A
POWER DELAY PROFILES

This section provides power delay profiles that are typically experienced in the 2.3 - 2.5 GHz band.

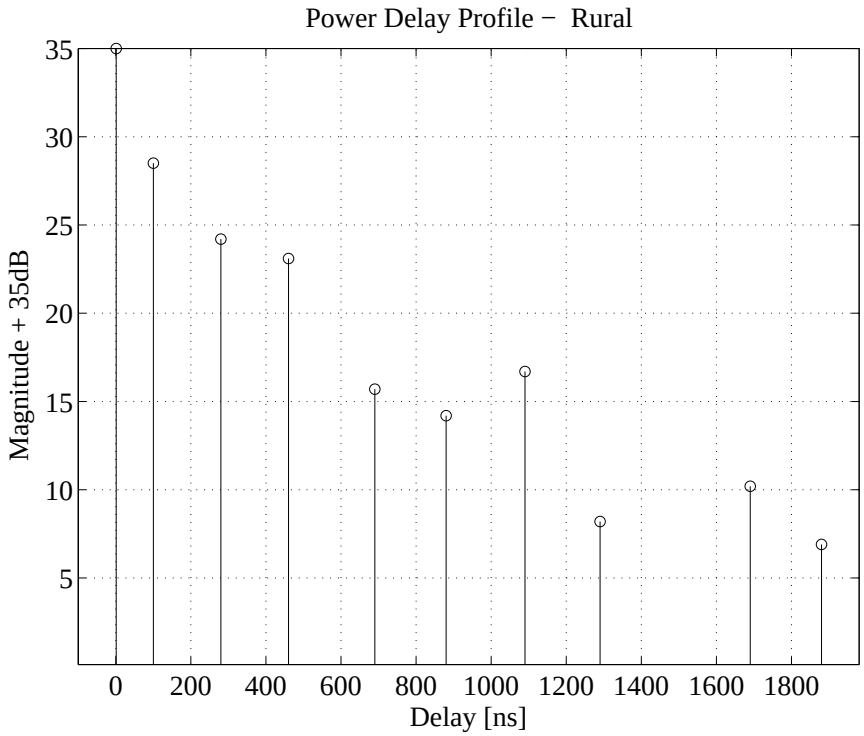

FIGURE A.1: Power delay profile for a rural area.

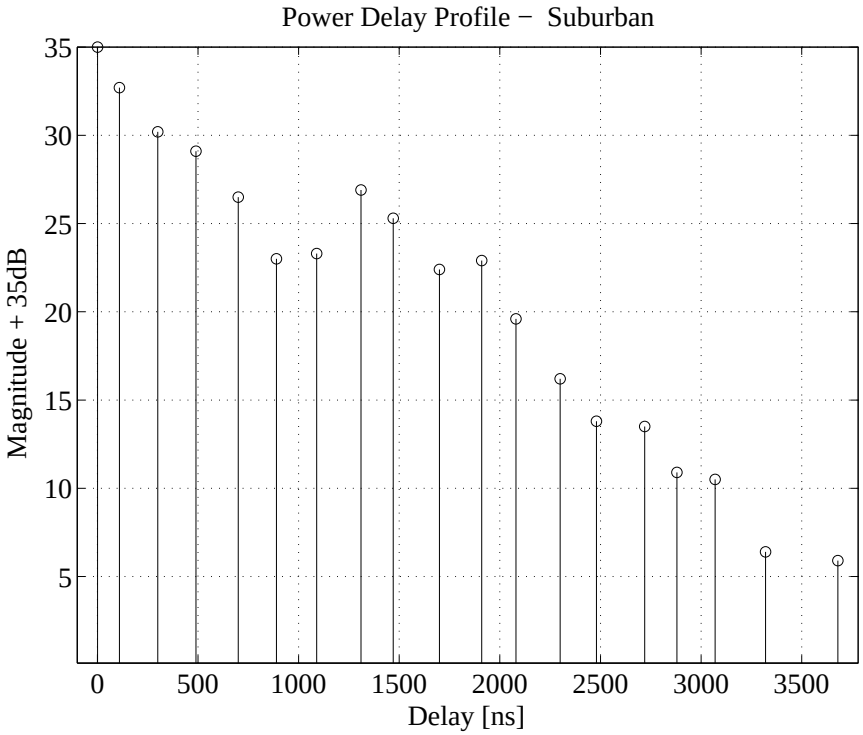

FIGURE A.2: Power delay profile for a suburban area.

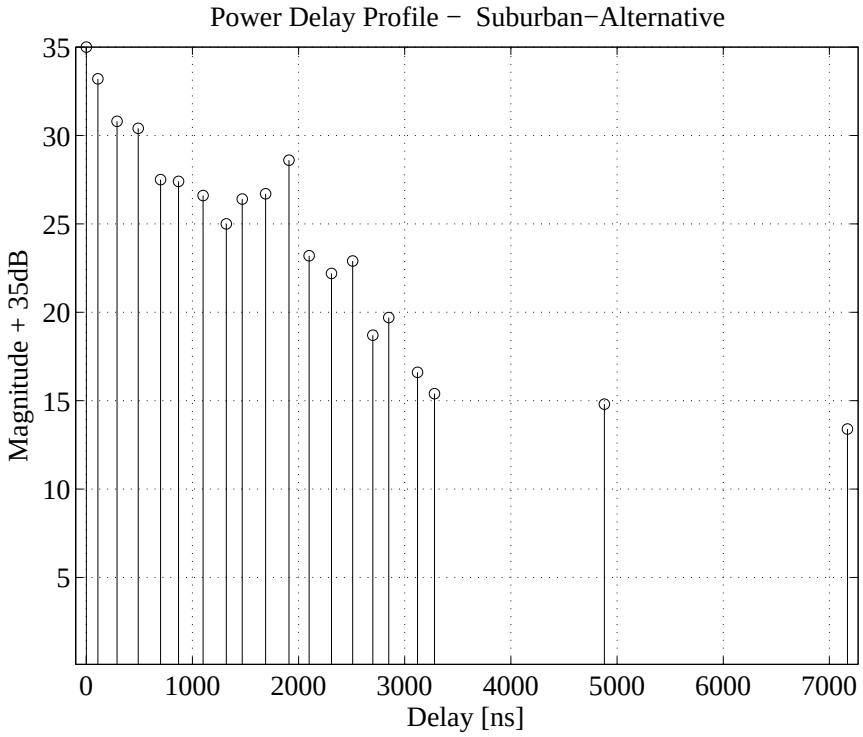

FIGURE A.3: Power delay profile for an alternative suburban area.

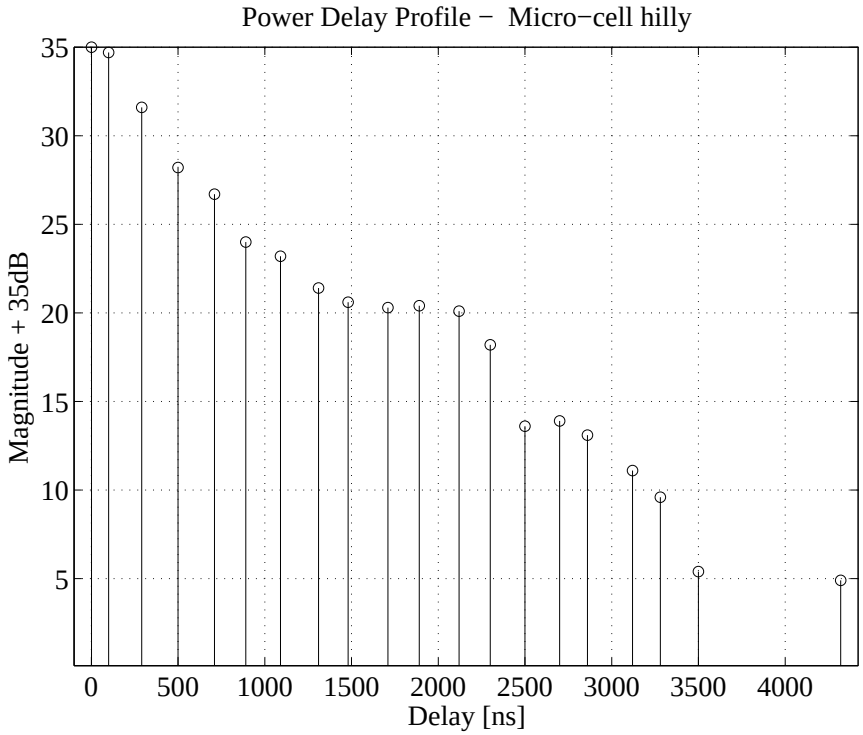

FIGURE A.4: Power delay profile for a micro-cell hilly area.

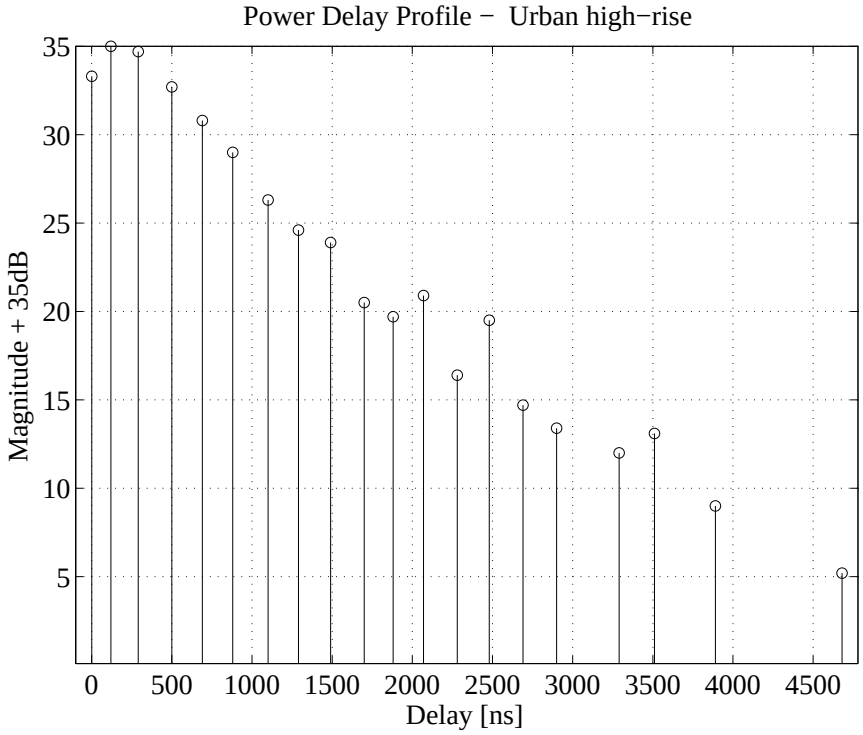

FIGURE A.5: Power delay profile for a urban high-rise area.

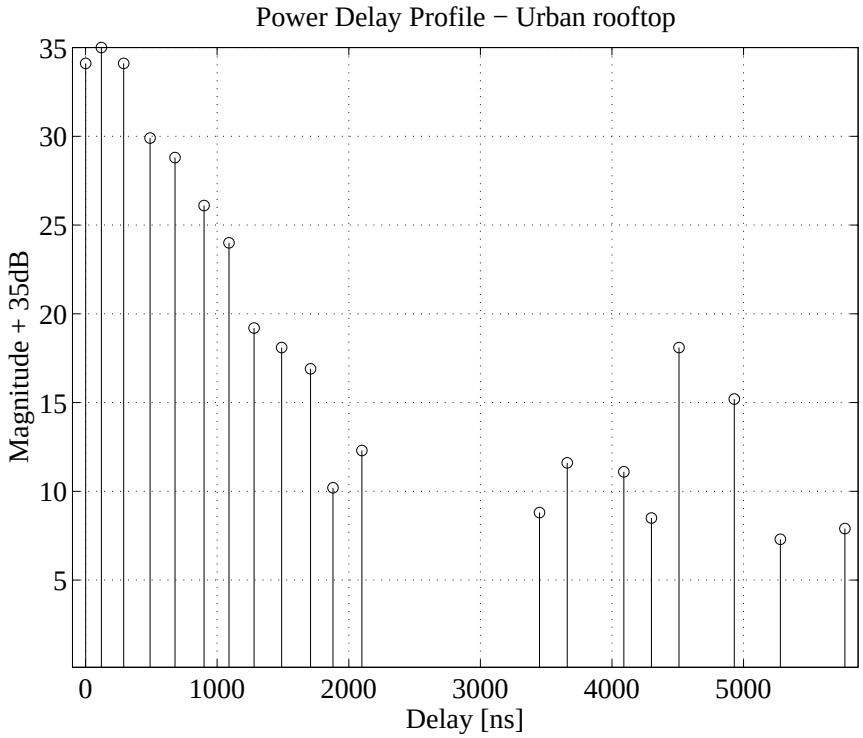

FIGURE A.6: Power delay profile for a urban rooftop area.

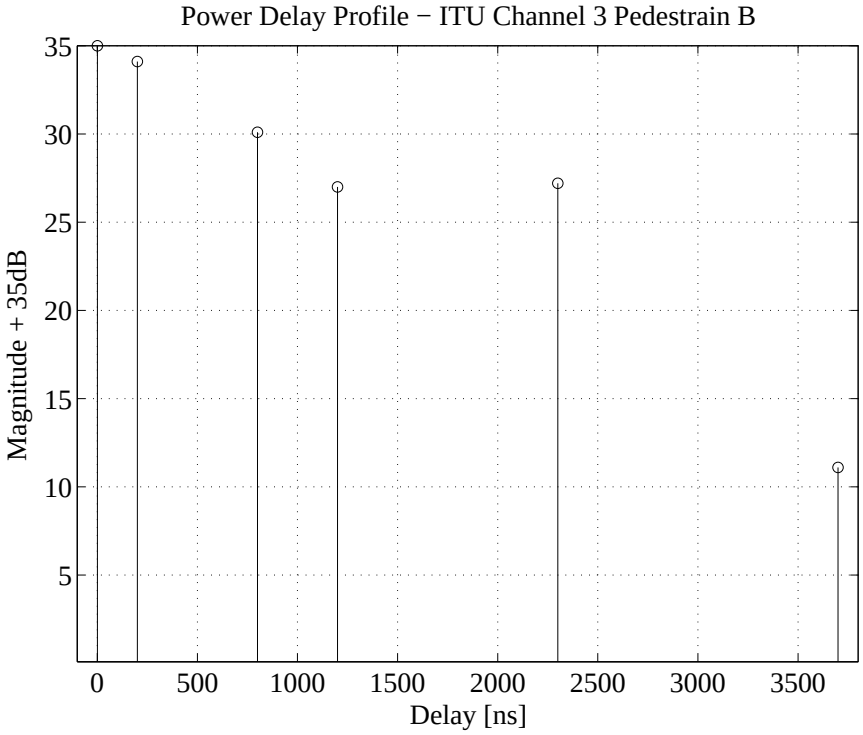

FIGURE A.7: Power delay profile for the ITU Channel 103 - Pedestrain B model.

APPENDIX B

NODE TABLE FOR CONVOLUTIONAL CODE

The most extensive convolutional code used today is the *NASA standard code* [5, 106], which has been used in many standards [8–10] and was standardized in mobile WiMAX [8] as a mandatory coding scheme. This code can be punctured and is pragmatic [107, 108] for TCM [20].

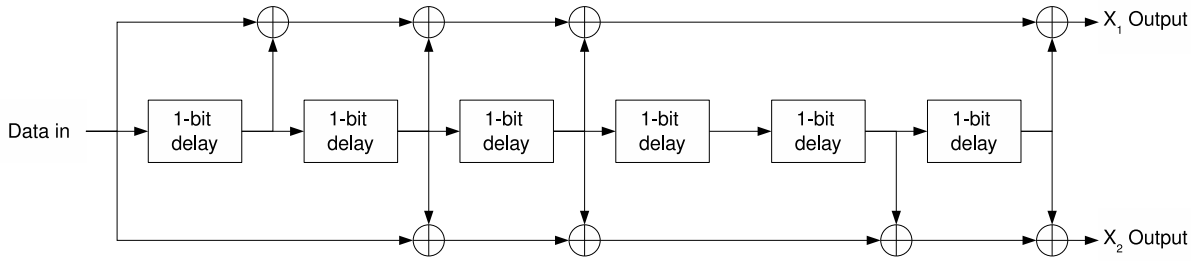

FIGURE B.1: CC encoder, $R_c = \frac{1}{2}$, $\mathcal{K} = 7$.

The convolutional encoder design has a free distance $d_{free} = 10$ and is illustrated in Figure B.1 with the generator taps of the encoder given in octal form as

$$g = (171; 133)_{oct}. \tag{B.1}$$

For the ease of implementation of a channel decoder, it is necessary to obtain the state diagram and all node information. These nodes can be easily hard-coded into most chipsets and for this reason is given in table B.1 as

TABLE B.1: State node information for mandatory CC in mobile WiMAX

Current node	Input	Output	Destination node	Input	Output	Destination node
000000_b	0_b	00_b	000000_b	1_b	11_b	100000_b
000001_b	0_b	11_b	000000_b	1_b	00_b	100000_b
000010_b	0_b	01_b	000001_b	1_b	10_b	100001_b
000011_b	0_b	10_b	000001_b	1_b	01_b	100001_b
000100_b	0_b	00_b	000010_b	1_b	11_b	100010_b
000101_b	0_b	11_b	000010_b	1_b	00_b	100010_b
000110_b	0_b	01_b	000011_b	1_b	10_b	100011_b
000111_b	0_b	10_b	000011_b	1_b	01_b	100011_b
001000_b	0_b	11_b	000100_b	1_b	00_b	100100_b
001001_b	0_b	00_b	000100_b	1_b	11_b	100100_b
001010_b	0_b	10_b	000101_b	1_b	01_b	100101_b
001011_b	0_b	01_b	000101_b	1_b	10_b	100101_b
001100_b	0_b	11_b	000110_b	1_b	00_b	100110_b
001101_b	0_b	00_b	000110_b	1_b	11_b	100110_b
001110_b	0_b	10_b	000111_b	1_b	01_b	100111_b
001111_b	0_b	01_b	000111_b	1_b	10_b	100111_b
010000_b	0_b	11_b	001000_b	1_b	00_b	101000_b
010001_b	0_b	00_b	001000_b	1_b	11_b	101000_b
010010_b	0_b	10_b	001001_b	1_b	01_b	101001_b
010011_b	0_b	01_b	001001_b	1_b	10_b	101001_b
010100_b	0_b	11_b	001010_b	1_b	00_b	101010_b
010101_b	0_b	00_b	001010_b	1_b	11_b	101010_b

Current node	Input	Output	Destination node	Input	Output	Destination node
010110_b	0_b	10_b	001011_b	1_b	01_b	101011_b
010111_b	0_b	01_b	001011_b	1_b	10_b	101011_b
011000_b	0_b	00_b	001100_b	1_b	11_b	101100_b
011001_b	0_b	11_b	001100_b	1_b	00_b	101100_b
011010_b	0_b	01_b	001101_b	1_b	10_b	101101_b
011011_b	0_b	10_b	001101_b	1_b	01_b	101101_b
011100_b	0_b	00_b	001110_b	1_b	11_b	101110_b
011101_b	0_b	11_b	001110_b	1_b	00_b	101110_b
011110_b	0_b	01_b	001111_b	1_b	10_b	101111_b
011111_b	0_b	10_b	001111_b	1_b	01_b	101111_b
100000_b	0_b	10_b	010000_b	1_b	01_b	110000_b
100001_b	0_b	01_b	010000_b	1_b	10_b	110000_b
100010_b	0_b	11_b	010001_b	1_b	00_b	110001_b
100011_b	0_b	00_b	010001_b	1_b	11_b	110001_b
100100_b	0_b	10_b	010010_b	1_b	01_b	110010_b
100101_b	0_b	01_b	010010_b	1_b	10_b	110010_b
100110_b	0_b	11_b	010011_b	1_b	00_b	110011_b
100111_b	0_b	00_b	010011_b	1_b	11_b	110011_b
101000_b	0_b	01_b	010100_b	1_b	10_b	110100_b
101001_b	0_b	10_b	010100_b	1_b	01_b	110100_b
101010_b	0_b	00_b	010101_b	1_b	11_b	110101_b
101011_b	0_b	11_b	010101_b	1_b	00_b	110101_b
101100_b	0_b	01_b	010110_b	1_b	10_b	110110_b

Current node	Input	Output	Destination node	Input	Output	Destination node
101101_b	0_b	10_b	010110_b	1_b	01_b	110110_b
101110_b	0_b	00_b	010111_b	1_b	11_b	110111_b
101111_b	0_b	11_b	010111_b	1_b	00_b	110111_b
110000_b	0_b	01_b	011000_b	1_b	10_b	111000_b
110001_b	0_b	10_b	011000_b	1_b	01_b	111000_b
110010_b	0_b	00_b	011001_b	1_b	11_b	111001_b
110011_b	0_b	11_b	011001_b	1_b	00_b	111001_b
110100_b	0_b	01_b	011010_b	1_b	10_b	111010_b
110101_b	0_b	10_b	011010_b	1_b	01_b	111010_b
110110_b	0_b	00_b	011011_b	1_b	11_b	111011_b
110111_b	0_b	11_b	011011_b	1_b	00_b	111011_b
111000_b	0_b	10_b	011100_b	1_b	01_b	111100_b
111001_b	0_b	01_b	011100_b	1_b	10_b	111100_b
111010_b	0_b	11_b	011101_b	1_b	00_b	111101_b
111011_b	0_b	00_b	011101_b	1_b	11_b	111101_b
111100_b	0_b	10_b	011110_b	1_b	01_b	111110_b
111101_b	0_b	01_b	011110_b	1_b	10_b	111110_b
111110_b	0_b	11_b	011111_b	1_b	00_b	111111_b
111111_b	0_b	00_b	011111_b	1_b	11_b	111111_b

APPENDIX C
NOTATIONS

C.1 NOTATION FOR INFORMATION THEORY

This section is focussed on presenting the notations used within this dissertation.

TABLE C.1: List of commutative semirings for iterative decoding

$\mathbb{K}$	"$(+, 0)$"	"$(\mathrm{x}, 1)$"	*Description*
$\mathbb{F}$	$(+, 0)$	$(\mathrm{x}, 1)$	
$\mathbb{F}[x, y, \ldots]$	$(+, 0)$	$(\mathrm{x}, 1)$	
$\mathbb{R}_{\geq 0}$	$(+, 0)$	$(\mathrm{x}, 1)$	sum-product
$\mathbb{R}_{\geq 0} \cup \{\infty\}$	$(\min, \infty)$	$(\mathrm{x}, 1)$	min-product
$\mathbb{R}_{\geq 0}$	$(\max, 0)$	$(\mathrm{x}, 1)$	max-product
$\mathbb{R} \cup \{\infty\}$	$(\min, \infty)$	$(+, 0)$	min-sum
$\mathbb{R} \cup \{-\infty\}$	$(\max, -\infty)$	$(+, 0)$	max-sum
$\{0, 1\}$	$(\mathsf{OR}, 0)$	$(\mathsf{AND}, 1)$	Boolean

Definition C.1.1 *If X is a discrete random variable with probability distribution $p_X(x)$, then the entropy is defined as [39]*

$$H(X) = -\sum^{x} p_X(x) \log p_X(x). \tag{C.1}$$

Definition C.1.2 *The joint entropy of a random variables X and Y is defined as [39]*

$$H(X,Y) = -\sum^{x,y} p_{X,Y}(x,y) \log p_{X,Y}(x,y), \tag{C.2}$$

and the chain rule [109] can be used to extend $Eq.$ (C.2) to [64]

$$H(X,Y) = H(X) + H(Y|X) = H(X) + \sum_{x} H(Y|X{=}x)p_X(x). \tag{C.3}$$

Where $H(Y|X{=}x)$ is the entropy of the random variable, given the probability distribution of $p_{Y|X}(y|x)$ and x is fixed.

Definition C.1.3 *The mutual information [39] between two random variables X and Y is defined as*

$$I(X;Y) = H(X) - H(X|Y) = H(Y) - H(Y|X), \tag{C.4}$$

and the maximum rate of reliable transmission [64] as

$$C = \max_{p_X(x)} I(X;Y). \tag{C.5}$$

Definition C.1.4 *The MAP decoding rule [64] is given by*

$$\overline{\tilde{b}}^{MAP}(\overline{\tilde{c}}) = \text{argmax}_{\overline{c}\in\mathcal{C}}\, p_{\overline{C}|\overline{C}}(\overline{c}|\overline{\tilde{c}}), \tag{C.6}$$

$$\overline{\tilde{b}}^{MAP}(\overline{\tilde{c}}) = \text{argmax}_{\overline{c}\in\mathcal{C}}\, p_{\overline{\tilde{C}}|\overline{C}}(\overline{\tilde{c}}|\overline{c}) \frac{p_{\overline{C}}(\overline{c})}{p_{\overline{\tilde{C}}}(\overline{\tilde{c}})}, \qquad \text{Bayes}' \text{ rule} \tag{C.7}$$

$$\overline{\tilde{b}}^{MAP}(\overline{\tilde{c}}) = \text{argmax}_{\overline{c}\in\mathcal{C}}\, p_{\overline{\tilde{C}}|\overline{C}}(\overline{\tilde{c}}|\overline{c}) p_{\overline{C}}(\overline{c}). \tag{C.8}$$

Definition C.1.5 *Processing of MAP and ML is equivalent if the codewords is uniformly distributed as*

$$p_{\overline{C}}(\overline{c^{[i]}}) = \frac{1}{2^{k_{\mathcal{C}}}}, \quad i = [0,1,\ldots,k_{\mathcal{C}}-1]. \tag{C.9}$$

This equates Eq. (C.8) to

$$\overline{\tilde{b}}^{MAP}(\overline{\tilde{c}}) = \text{argmax}_{\overline{c}\in\mathcal{C}}\, p_{\overline{\tilde{C}}|\overline{C}}(\overline{\tilde{c}}|\overline{c})p_{\overline{C}}(\overline{c}), \tag{C.10}$$

$$\overline{\tilde{b}}^{MAP}(\overline{\tilde{c}}) = \text{argmax}_{\overline{c}\in\mathcal{C}}\, p_{\overline{\tilde{C}}|\overline{C}}(\overline{\tilde{c}}|\overline{c}), \qquad \text{Constant factor} \tag{C.11}$$

$$\overline{\tilde{b}}^{MAP}(\overline{\tilde{c}}) = \overline{\tilde{b}}^{ML}(\overline{\tilde{c}}). \tag{C.12}$$

C.2 NOTATION FOR DISTRIBUTIONS

This section was focussed on presenting the different distributions that are used with the analysis of LDPC codes.

C.2.1 L-Distribution

Definition C.2.1 *The log-likelihood ratio for a received code bit is given as*

$$LLR(\tilde{c}_i) = \frac{P(\tilde{c}_i = 1)}{P(\tilde{c}_i = 0)}. \tag{C.13}$$

Definition C.2.2 *Let L denote the random variable of the log-likelihood ratio obtain from Eq. (C.13), $L \in (-\infty, \infty]$, in a space denoted by $\mathcal{A}_L$. The distribution of random variable L is presented by $A(l)$ and let $A(l)$ be a right-continuous non-decreasing function over $\mathbb{R}$ respectively that satisfies the following properties [27] of*

$$\lim_{l\to-\infty} A(l) = 0, \tag{C.14}$$

$$\lim_{l\to\infty} A(l) \leq 1, \tag{C.15}$$

$$A \in \mathcal{A}_L, \tag{C.16}$$

$$P(L \in (-\infty, l_u]) = A(l_u), \tag{C.17}$$

$$P(L = \infty) = 1 - \lim_{l_u\to\infty} A(l_u). \tag{C.18}$$

Definition C.2.3 *A probability mass exists at $l = \infty$ as shown in Eq. (C.15) for the Belief Propagation algorithm.*

Definition C.2.4 *A density $a(l)$ is defined as the derivative (Radon-Nikodyn) of the set of elements in space $\mathcal{A}_L$, with the densities existing over $(-\infty, \infty]$.*

Definition C.2.5 *The density $a(l)$ corresponds to the distribution $A(l)$ with*

$$\int_l g(x)dA(x) = \int_l g(x)a(x)dx, \tag{C.19}$$

when $g(x)$ is assumed to be a non-negative continuous function.

Definition C.2.6 *The Heavy distribution (step distribution) is defined as [64]*

$$H_z(x) = \begin{cases} 0 & x < z, \\ 1 & x \geq z. \end{cases} \tag{C.20}$$

Definition C.2.7 *The density of $H_z(x)$ is presented by $\Delta_z(x)$ and $\Delta_z(x)$ is the Dirac function [48] shifted by z.*

Definition C.2.8 *The convolution of two L-distributions $A, B \in \mathcal{A}_L$ is defined as [27, 64]*

$$(A * B)(l) = \int A(l-y)dB(y) = \int B(l-y)dA(y), \tag{C.21}$$

and the corresponding L-densities a and b is expressed as $(a * b)(l)$.

Definition C.2.9 *The distribution $A(l) \in \mathcal{A}_L$ is symmetric and thus the following property holds*

$$\int f(x)dA(x) = \int e^{-x} f(-x)dA(x), \tag{C.22}$$

for a bounded continuous function $f(x)$.

Definition C.2.10 *The Bhattacharyya constant associated with a symmetric l-density $a(l)$ is given as [64]*

$$\mathcal{B}(a(l)) = \int a(x) \exp\left(\frac{-x}{2}\right) dx, \tag{C.23}$$

and for the purpose of an AWGN channel we have [27]

$$\mathcal{B}(a_{\text{AWGN}}(l)) = \int \sqrt{\frac{\sigma^2_{\eta(t)}}{8\pi}} \exp\left(-\frac{(x - 2/\sigma^2_{\eta(t)})^2 \sigma^2_{\eta(t)}}{8}\right) \exp\left(\frac{-x^2}{2}\right) dx, \tag{C.24}$$

$$\mathcal{B}(a_{\text{AWGN}}(l)) = \exp\left(-\frac{1}{2\sigma^2_{\eta(t)}}\right). \tag{C.25}$$

C.2.2 G-Distribution

Definition C.2.11 *We define* $\mathfrak{h}(l)$ *as an unconventional probabilistic hard-decision function that takes the log-likelihood ratio* l=$LLR(\tilde{c}_i)$ *of the code bit as [64]*

$$\mathfrak{h}(l) = \begin{cases} 1 & \text{if } l > 0, \\ 1 & \text{if } l = 0 \text{ probability of } \frac{1}{2}, \\ -1 & \text{if } l = 0 \text{ probability of } \frac{1}{2}, \\ -1 & \text{if } l < 0. \end{cases} \tag{C.26}$$

Definition C.2.12 *The G-distribution is a convenient method of expressing operations done at the check node of the Tanner graph [27] and is given as*

$$g(l) = \left(\mathfrak{h}(l), \ln\left(\coth\left(\frac{|l|}{2}\right)\right)\right), \tag{C.27}$$

with l=$LLR(\tilde{c}_i)$*. Note that* $g(l)$ *takes on value in ranges of* $\{\pm 1\} \times [0, \infty]$*. It should be noted that in the horizontal step the Belief Propagation decoding can easily be computed with a* $1/tanh(l/2)$ *function, but for analysis of the G-distribution we rather use the* $coth(l/2)$ *function for providing positive values for the distribution.*

Definition C.2.13 *A sufficient representation for a G-density in* $Eq.$ *(C.28) and G-distribution in* $Eq.$ *(C.29) is presented by [27, 64] as*

$$\mathtt{a}(s, x) = \perp_{\{s=1\}} \mathtt{a}(1, x) + \perp_{\{s=-1\}} \mathtt{a}(-1, x), \tag{C.28}$$

$$\mathtt{A}(s, x) = \perp_{\{s=1\}} \mathtt{A}(1, x) + \perp_{\{s=-1\}} \mathtt{A}(-1, x), \tag{C.29}$$

with the notation of

$$\perp_{\{s=e\}} = \begin{cases} 1 & \text{if } s = e, \\ 0 & \text{otherwise.} \end{cases} \tag{C.30}$$

The distributions $\mathtt{A}(1, x)$ *and* $\mathtt{A}(-1, x)$ *are both non-decreasing right continuous functions with*

the following properties of

$$\lim_{x\to\infty} \mathtt{A}(1,x) \geq \lim_{x\to\infty} \mathtt{A}(-1,x), \tag{C.31}$$

$$\mathtt{A}(1,0) \geq 0, \tag{C.32}$$

$$\mathtt{A}(-1,0) = 0, \tag{C.33}$$

$$\mathtt{a}(1,0) = |\mathtt{A}(1,0)|, \tag{C.34}$$

$$\mathtt{a}(1,\infty) = \frac{1}{2}\left(1 - \lim_{x\to\infty} \mathtt{A}(1,x) - \lim_{x\to\infty} \mathtt{A}(-1,x)\right), \tag{C.35}$$

$$\mathtt{a}(-1,\infty) = \frac{1}{2}\left(1 - \lim_{x\to\infty} \mathtt{A}(1,x) - \lim_{x\to\infty} \mathtt{A}(-1,x)\right), \tag{C.36}$$

$$\mathtt{A}(s,x) \in \mathcal{A}_G. \tag{C.37}$$

This ensures that point mass probabilities exists at $x = 0$ and $x = \infty$.

C.2.3 Mapping of Distributions

It is convenient to switch between distributions in our analysis. Let Γ denote the map of a L-distribution to a G-distribution and let Γ^{-1} denote the inverse operator [27].

Definition C.2.14 *The Γ operator is given as*

$$\mathtt{A}(1, z \geq 0) = 1 - A^{-}(\ln(\coth(z/2))), \tag{C.38}$$

$$\mathtt{A}(-1, z \geq 0) = A(-\ln(\coth(z/2))), \tag{C.39}$$

$$\mathtt{a}(1, z \geq 0) = \frac{a(\ln(\coth(z/2)))}{\sinh(z)}, \tag{C.40}$$

$$\mathtt{a}(-1, z \geq 0) = \frac{a(-\ln(\coth(z/2)))}{\sinh(z)}. \tag{C.41}$$

Definition C.2.15 *The Γ^{-1} operator is given as*

$$A(z \geq 0) = 1 - \mathtt{A}^{-}(1, \ln(\coth(z/2))), \tag{C.42}$$

$$A(z < 0) = \mathtt{A}(-1, \ln(\coth(-z/2))), \tag{C.43}$$

$$a(z \geq 0) = \frac{\mathtt{a}(1, \ln(\coth(z/2)))}{\sinh(z)}, \tag{C.44}$$

$$a(z < 0) = \frac{\mathtt{a}(-1, \ln(\coth(-z/2)))}{\sinh(-z)}. \tag{C.45}$$

Definition C.2.16 *The convolution of two G-distributions* $\mathtt{A}, \mathtt{B} \in \mathcal{A}_G$ *is defined as [27, 64]*

$$\mathtt{A} \circledast \mathtt{B} = \perp_{\{s=1\}} \big(\mathtt{A}(1,\cdot) * \mathtt{B}(1,\cdot) + \mathtt{A}(-1,\cdot) * \mathtt{B}(-1,\cdot)\big) + \perp_{\{s=-1\}} \big(\mathtt{A}(-1,\cdot) * \mathtt{B}(1,\cdot) + \mathtt{A}(1,\cdot) * \mathtt{B}(-1,\cdot)\big) \tag{C.46}$$

with

$$\mathtt{A}(s,x) = \perp_{\{s=1\}} \mathtt{A}(1,x) + \perp_{\{s=-1\}} \mathtt{A}(-1,x), \tag{C.47}$$

$$\mathtt{B}(s,x) = \perp_{\{s=1\}} \mathtt{B}(1,x) + \perp_{\{s=-1\}} \mathtt{B}(-1,x). \tag{C.48}$$

Where $*$ *denotes a one-sided convolution of standard distribution [64].*